Study on fueling characteristics of supersonic gas puffing applied to large high-temperature plasmas

Akiyoshi Murakami

DOCTOR OF PHILOSOPHY

Department of Fusion Science

School of Physical Science

The Graduate University for Advanced Studies

2011

Acknowledgements

At first, I would like to express my sincere gratitude to my advisers Prof. Hiroshi Yamada and Dr. Junichi Miyazawa for their guidance, support, and encouragement over five years of my doctoral course.

I am deeply grateful to Mr. Koji Yasui and Mr. Takanori Murase for their kind helps and supports in the SSGP installation and the design of Laval nozzle.

Special thanks to Dr. Tomohiro Morisaki, Dr. Ryuichi Sakamoto, Dr. Naoki Tamura, Dr. Yoshiro Narushima, Dr. Tsuyoshi Akiyama, Dr. Naoko Ashikawa, Dr. Hayato Tsuchiya and others for their supports, many useful suggestions and comments.

My sincere gratitude to previous and present Director General of National Institute for Fusion Science (NIFS) Prof. Osamu Motojima and Prof. Akio Komori, respectively. I wish to express my appreciation to all members of the LHD experimental group, NIFS and the Graduate University for Advanced Studies (SOKENDAI) staffs for their supports.

Furthermore, I thank Dr.(to be) Kinya Saito, and the other Ph.D students in NIFS for mutual encouragement, and for sharing hopes and concerns about the future.

Finally, I am sincerely grateful to my family and friends for their support and understanding.

This work has been financially supported by the Ministry of Education, Sports, Culture, Science and Technology, Grants-in-Aid for Scientific Research (S) 20226018 and NIFS09ULFF006. This work is also supported by Grant-in-Aid for Japan Society for the Promotion of Science Fellowship (No. 23-1219).

March, 2012
Akiyoshi Murakami

Abstract

Fueling characteristics of supersonic gas puffing (SSGP) applied to large high-temperature plasmas have been investigated in the Large Helical Device (LHD). A fueling efficiency of ~20 % can be achieved in low-density plasmas and it decreases as the target plasma density increases. This is due to the fueling mechanism of SSGP, where the fuel particles are supplied to the plasma edge region and then transported to the core region by diffusion. The fueling efficiency improves depending on the recycling condition and/or the edge density condition of the target plasma. Various phenomena are induced by SSGP, such as the reheat of the plasma stored energy, the strong edge cooling and the nonlocal transport. The electron temperature fluctuations related to the MHD instability are induced after the nonlocal phenomenon. SSGP is also capable of inducing the fast density modulation externally by using fast pulse train. The convergence of gas flow plays an important role in these experiments. An effectiveness of a Laval nozzle in generating the convergent gas flow has been tested by visualizing the gas flow.

Establishment of fueling methods in future thermonuclear fusion reactors is one of the critical issues. In a fusion reactor, the role of fueling device is to supply fuel particles and, consequently, to control the plasma density profiles. Two major fueling methods have been used in the plasma experiments. One is the gas puffing that is a conventional method and has been used since the early period of the fusion plasma study. The conventional gas puffing has a drawback of low fueling efficiency. The other is the ice-pellet injection that can effectively increase the density in the plasma core region. However, the pellet injection device is complicated compared with the gas puffing device. SSGP has been developed as a new fueling method that can combine both advantages of the pellet injection and the conventional gas puffing, i.e., simpleness of the device, high fueling efficiency, and rapid response. In SSGP, high-pressure gas is ejected through a fast solenoid valve equipped with the Laval nozzle. SSGP supplies pulsed convergent gas flow to the plasma.

Before applying SSGP to LHD, the effectiveness of the Laval nozzle has been tested by visualizing the gas flow. Three methods have been

applied for visualization, i.e., the shadow graph imaging, the emission imaging using electron beam, and the laser scattering after forming the cluster beam. The cluster beam is formed by selecting the gas species, or by cooling the gas using a refrigerator.

As the first step, the cluster beam ejected through the fast solenoid valve without using the Laval nozzle has been investigated by selecting the gas species capable of forming the cluster at a room temperature in a test chamber. Time-resolved 2-D images of Rayleigh scattering from clusters have been measured by a fast charge coupled device camera. The expansion half angle of the gas flow without the Laval nozzle was 22.5º. The scattering signal was proportional to the averaged cluster size and the number density of clusters. The scattering signals from argon and nitrogen clusters showed approximately cubic dependence on the backing pressure as expected from a model. Meanwhile, stronger pressure dependence than this was found in the case of methane, where the scattering signal increased with the fifth power of the backing pressure at 3.2 MPa – 7 MPa, and it was further enhanced at > 7 MPa. This suggests that a new structure model would be necessary to determine the cluster size of methane, which shows stronger backing pressure dependence than argon and nitrogen.

Next, formation of the hydrogen cluster beam using the Laval nozzle has been investigated at a low-temperature regime ranging from 120 K to 300 K. The Rayleigh scattering signal from hydrogen clusters was detected when the temperature was lower than 178 K, as expected from a calculation result of the cluster formation condition. The scattering signal intensity was inversely proportional to the fifth power of the gas temperature and the cube of the backing pressure as expected from an available cluster model. The divergence of cluster beam has been decreased from 22.5 º to ~5 º after installation of the Laval nozzle.

Based on the test results of the Laval nozzle, fueling characteristics have been investigated in LHD. Since there is no disruption in LHD, the edge density can be significantly increased by supplying particles with a large flow rate. The plasma minor radius of ~0.6 m is much longer than the penetration depth of neutrals supplied by SSGP, of which the typical order is mm in LHD. The fueling efficiency of SSGP depends on the target plasma density and decreases as the density increases. This is due to the fueling mechanism of SSGP, where the fuel particles are supplied to the

plasma edge region and then transported to the core region by diffusion. SSGP locally supplies a large number of particles to the edge region within a short time on the order of ms. The fueling efficiency of ~20 % can be achieved by SSGP, which is more than twice higher than that of ordinary gas puffing.

Two kinds of improvement in the fueling efficiency of SSGP have been observed. The fueling efficiency improved suddenly when the target plasma was close to the density limit. In the case of hydrogen SSGP, abrupt increase in the density increase rate was observed with the plasma shrinkage. As a result of this, the fueling efficiency was improved for two times even though the difference in the number of supplied particles was less than 20 %. The fueling efficiency also improved when the edge-density was kept high and a strongly hollow density profile was maintained. The fueling efficiency of helium SSGP is indeed higher than that of hydrogen SSGP because of the high recycling property.

SSGP can be also used for physics experiments. For example, the nonlocal transport phenomenon and electron temperature fluctuations were triggered by SSGP. After a short-pulse SSGP, the core electron temperature increased while the edge electron temperature decreased. SSGP triggered a longer core temperature increase than that triggered by a small impurity pellet injection. The temperature profile, which was relatively flat inside the half minor radius before SSGP, becomes parabolic after non-local transport was triggered. Fluctuations were excited in the electron temperature signals around the half minor radius. The frequency of these fluctuations increased from ~400 Hz to ~1 kHz within ~0.1 s and the amplitude decreased correspondingly. The temperature fluctuations inside and outside of the half minor radius had opposite phases. Magnetic fluctuations resonating near the half minor radius were observed simultaneously with the electron temperature fluctuations.

Fast density modulation experiments using SSGP has been also carried out in the LHD. The fast density modulation of 50 ~ 200 Hz was excited by SSGP. High-frequency injection (500 Hz) was confirmed in preliminary experiments on the test stand. The achieved frequency of 200 Hz is still smaller than that demonstrated in the test stand of 500 Hz. The optimum flow rate for fast density modulation in LHD was 40 – 200 $Pa \cdot m^3/s$. In the case of 50 Hz injection, higher harmonics of up to 200 Hz

was also observed simultaneously.

SSGP has an additional effect of edge cooling that will be beneficial for divertor heat load reduction. The edge temperature during or just after SSGP becomes more than 50 % lower than that in the case of conventional gas puffing, compared at the similar edge density. This strong edge cooling effect will be beneficial for divertor heat load reduction, which is inevitable in future fusion reactors, since the low edge temperature enhances the radiation loss in the ergodic layer and reduces the conduction loss to the divertor plates.

In conclusion, the fueling efficiency of SSGP is more than twice higher than that of conventional gas puffing. The fueling efficiency improves when the target plasma is close to the density limit during SSGP and the edge-density is kept high and a strongly hollow density profile is maintained. In plasma physics experiments, SSGP caused various interesting phenomena by supplying the short convergent gas flow. SSGP is also available as the fueling method which triggers a variety of plasma responses by supplying a large numbers of particles in a short time. The scientific knowledge obtained in this study will be beneficial for future fusion reactors.

Contents

Chapter 1

Introduction

1.1 Fusion study and state of the world

A movement against the nuclear power plants has been invoked by a nuclear accident on Fukushima Daiichi Nuclear Power Station after the east Japan earthquake occurred on March 11, 2011. The nuclear power had accounted for 30% of the energy source in Japan before the accident. This is due to the policy that had been taken to reduce the risk of oil shortage after twice oil shocks in 1970s. In terms of energy balance, Japanese government should have kept a variety of energy sources. As a result, the nuclear energy was promoted in Japan. Japanese nuclear industries have been evolved to the leading industries in the world. However, Japanese energy policy after the east Japan earthquake is reaching a turning point.

It is expected that the world population will reach 9.3 billion at 2050s [1]. The countries of most increase in the Gross Domestic Product (GDP) at 2050s are China, India, Brazil and Russia which are called “BRICS”. These countries will economically develop significantly in a future. Energy is absolutely essential for economic activities. When large economic activities develop in these countries of large population, it will become necessary for human beings to use more energy than now.

There are various energy sources. The most popular energy source is the fossil fuels, such as coal, oil and natural gas. In the case of energy from fossil fuel, depletion is of special concern. In a future expected of the increase of population and economic activity, the energy from fossil fuels will not be sufficient for supplying all of the energy demands. The price of energy from fossil fuel also will increase more and more. In the case of renewable energy sources such as solar and wind power, the stable power cannot be supplied because of the weather. Unstable electric power is fatal for manufacturing factories. An energy source that can produce a lot of energy is the nuclear power. There are two methods to produce the nuclear power. One is fission in which the nucleus of an atom is split releasing a large amount of energy. The other is fusion in which the nuclei of atoms are combined to form a heavier nucleus, with energy being released. Nuclear power has an advantage of producing huge stable power. However, in the case of fission plants, there is a safety problem as mentioned. One of the most difficult problems is how to manage high-level radioactive wastes from fission power plants. We must control these high-level radioactive wastes for over tens of thousands of years.

Nuclear fusion is more safety than nuclear fission because there are no nuclear chain reactions in nuclear fusion. In fusion reactions, the runaway reactions will not cause in principle. The deuterium-tritium (D-T) reaction is selected for thermo-nuclear fusion because of its large cross section [2]. The reaction occurs as follows,

$$D + T \rightarrow He^4(3.5MeV) + n(14MeV) \quad (1.1)$$

Deuterium exists in sea and tritium will be bred in the process of the n-L reaction. If a fusion reactor realizes, the energy problem in the world might be solved. Fusion study started at 1950s. Many fusion experiments have been carried out in the world. International Thermonuclear Experimental Reactor (ITER) has been under construction at Cadarache, France in order to demonstrate the possibility of fusion reactor [3]. In ITER, D-T reaction will be occurred and it will be aimed that it takes out ten times larger energy compared with input power.

In conclusion, fusion study has to be promoted for future human beings by global

cooperation in order to take out energy from nuclear fusion.

1.2 Fueling system in fusion reactors

1.2.1 Introduction of fueling system

Establishment of fueling methods is one of the critical issues for the realization of a fusion reactor. There are four control factors of heat and particle transport in fusion plasmas. Those are a fueling system, a heating system, an exhaust system, and a heat removal system (See Fig. 1.1). Firstly, the fueling system supplies particles to fusion plasmas. As shown in Eq. (1.1), deuterium and tritium have to be continuously supplied to the plasma in fusion reactors. Secondly, the heating system heats the plasma to a temperature needed for nuclear fusion reactions. In current plasma experiment, neutral beam injection, ion cyclotron heating, and electron cyclotron heating are mainly used as the heating system. Thirdly, the exhaust system removes unnecessary particles. After nuclear fusion reactions, helium particles (alpha-particles) are generated, as also shown in Eq. (1.1). The alpha particles heat the plasma in the fusion reactor. After that, these particles become helium ash. Helium ash has to be removed otherwise the plasma temperature will decrease due to enhanced radiation loss. In the exhaust system called “divertor”, the magnetic field lines are connected to the divertor plate and those particles are exhausted. Finally, the heat removal system removes heat from the fusion plasma. The divertor system is also used as the heat removal system. Heat from neutron after nuclear fusion reactions is taken out as energy by the system called “blanket” located on first wall of a vacuum vessel. The blanket system will play another role in breeding of tritium from reactions between lithium and neutron.

Especially, since the alpha heating is dominant in the fusion plasma as previously described, the only active control factor is the fueling system. In addition, in order to obtain the fusion power continuously, the steady state plasma is required in fusion

reactors. In steady state plasma, the density control is fairly important. Recent results of particle control in the high temperature tokamak plasma were reported in JT- 60U, ASDEX-U and JET [4-6]. The role of fueling system is to supply fuel particles and, consequently, to control the plasma density profile.

In conclusion, the fueling system will be essential for the fusion plasma control and therefore development of effective fueling methods has been one of the key issues in the fusion study.

Conventionally, two fueling methods of a gas puffing system and a pellet injection have been studied for a long time. The conventional gas puffing (GP) and the pellet injection (PI) system are described in the following. A brief exposition of supersonic gas puffing (SSGP) is also given.

1.2.2 Conventional gas puffing (GP)

The conventional gas puffing (GP), in which fuel gas is ejected into the vacuum vessel and supplied to the edge plasma, has been used since early fusion plasma experiments. Piezo electric valves are often used in the conventional gas puffing. A piezo valve is available in a magnetic field. The maximum backing pressure is limited to less than ~0.6 MPa and the order of the minimum pulse length is ~1 ms. The conventional gas puffing has a drawback of low fueling efficiency. Especially in large plasmas, most of the particles supplied by gas puffing are ionized outside of the plasma confinement region. As a result, the fueling efficiency is as low as ~10 % [7, 8]. In tokamaks, shielding of fuel particle was observed in the case of conventional gas puffing [9].

1.2.3 Pellet injection (PI)

The ice-pellet injection (PI) is considered as a favorable method to refuel magnetically confined plasmas [10]. Hydrogen gas is cooled by a refrigerator to ~10 K

to form small ice pellets. The pellet is injected to plasma at a velocity of ~1000 m/s. PI is characterized by the high fueling efficiency reaching 100 % and can effectively increase the density in the plasma core region. From the point of view of the time response, the density increases within the duration of the pellet ablation of less than 1 ms in the case of PI, while the typical time constant of density control by GP is similar to the particle confinement time. Using the pellet injection, improved particle and energy confinement properties have been demonstrated in LHD [11]. In LHD, a super dense core plasma develops when a series of pellets are injected [12]. High-density steady state operation has also been demonstrated in LHD [13]. However, the pellet injection device itself is complicated compared with a gas puff device and still has demanding technological issues for a fusion reactor.

1.2.4 Supersonic gas puffing (SSGP)

Supersonic gas puffing (SSGP) has been developed as a new fueling method that can combine both advantages of the pellet injection and the conventional gas puffing, i.e., simpleness of the device, high fueling efficiency, and rapid response [14,15]. In SSGP, high-pressure gas is ejected through a fast solenoid valve equipped with a Laval nozzle. SSGP supplies pulsed convergent gas flow to the plasma. In this study, fueling characteristics of SSGP applied to large high-temperature plasmas and the plasma physics experiments using SSGP are described. Detailed explanations of the SSGP device are described in Chapter 2.

1.3 Large Helical Device

In this study, SSGP has been applied to the large high-temperature plasma on Large Helical Device (LHD) in National Institute for Fusion Science (NIFS). Figure 1.2 shows the bird's-eye view of LHD.

In a magnetic confinement fusion study, there are two major methods to maintain plasmas. One is a device called “tokamak”, which is devised by Russian researchers in the 1960s. In tokamak devices, the electric current is driven in the plasma to form magnetic fields for plasma confinement. Tokamak has been the top runner in the fusion research. Highest ion temperature of 520 million degrees centigrade was achieved in JT-60U tokamak. ITER is also a tokamak device. However, plasma collapse phenomenon called “disruption” is observed in tokamak [16]. Disruptions occur suddenly and damage the vacuum vessel. This phenomenon is weakpoint of the tokamak as a fusion reactor. On the other hand, the other method of stellarator device is devised by Dr. Spizer in 1950s. One of the merits of a stellarator device is not to require the plasma current. The helical device is an improved version of the stellarator device. The confinement magnetic fields are produced by external coils alone. There is no disruption in the helical device. Therefore, as a nuclear fusion reactor, helical device has an advantage in steady state operation.

LHD is the world’s-largest superconducting helical device where nested magnetic surfaces are generated by a pair of continuously wound helical coil and three pairs of planar poloidal coils [17,18]. The major radius, R, can be adjusted from 3.5 m to 3.9 m. The minor radius, a, is ~0.6 m. The volume of the vacuum vessel is ~200 m^3. The typical plasma volume, V_p is ~30 m^3 in the standard configuration of R = 3.6 m. The magnetic field strength on the plasma axis, B_t, is up to 3 T. A steady state operation has been demonstrated in LHD [19].

Three heating systems of electron cyclotron heating (ECH) [20], ion cyclotron heating (ICH) [21,22] and neutral beam injection (NBI) [23] have been employed in LHD. There are three negative-ion-based tangential neutral beam injectors and two positive-ion-based vertical neutral beam injectors. In this study, the plasma was mainly heated by three negative-ion-based tangential neutral beam injectors. The total heating power of neutral beam injectors was up to 14 MW.

Many plasma measurement systems have been installed on LHD. The plasma

characteristics after SSGP are analyzed by electron density profiles measured by a Thomson scattering system [24,25]. The Thomson scattering system is installed on a horizontally elongated section in LHD. The line-averaged density is measured by a FIR laser interferometer [26].

The conventional gas puffing systems has been installed on 3.5-L, 5.5-L 9.5-L and 6-I port in LHD [27]. The gas flow rate of the conventional gas puffing is selectable from 1 to 100 Pa·m^3/s. Ordinary gas species of gas puffing is hydrogen. Other gas species of helium, nitrogen, neon and argon are used in some experiment conditions. Although the fueling efficiency is low, gas puffing is mainly used in the experiment as the most reliable fueling method. The pellet injection system is installed on 4-O port in LHD. The position of SSGP is 3.5-L port. The gas flow is upward and the distance from valves to plasma is ~4 m.

1.4 Position of SSGP in the world

There are many methods similar to SSGP in the world plasma devices as described below.

- **SMBI in HL-2A**

  Supersonic molecular beam injection (SMBI) has been installed on HL-2A tokamak (Plasma volume, V_p ~ 5.2 m^3). Prof. Yao started to develop supersonic molecular beam injection (SMBI) on HL-1M for the first time [28-31]. Two type SMBIs (high- and low- filed side injections) have been installed on HL-2A. The valve for LFS SMBI is an electro-magnetic valve, which is the same type used for SSGP in LHD. On the other hand, the valve for HFS SMBI is a pneumatic valve, which is the same type used in Tore Supra [30]. The distance from plasma to LFS nozzle is ~1.28 m. The fueling efficiency of both SMBIs, which is defined as the ratio

of the increment of the plasma content divided by the number of injected particles, was 30 ~ 60 %. The fuelling efficiency of HFS SMBI is higher than that of LFS SMBI. It was also reported that H-mode was triggered by SMBI instead of pellet injection in HL-2A [32]. Recently, a conic nozzle with a diameter of 0.5 mm and half angle of 8^{o} is installed on the valve of LFS SMBI [33].

- **SPGI in Tore Supra**

Supersonic pulsed gas injection (SPGI) has been installed on Tore Supra tokamak (V_p ~ 25 m^3) [34,35]. The fueling efficiency of SPGI, which was derived from interferometer measurements, was 30 ~ 50 % in the limiter discharges. The fueling efficiency from the LFS tends to be better than that from the HFS. The fueling efficiency in the divertor discharges is lower than that in the limiter discharges. The edge cooling effect of SPGI has been observed in Tore Supra. It was revealed that SPGI reduced wall inventory compared to a similar conventional gas puffing in one long pulse discharge.

- **SMBI in JT-60U**

SMBI was installed on JT-60U tokamak (V_p ~ 80 m^3) [36,37]. The SMBI system in JT-60U is the same as that used in Tore supra. It was revealed that a fueling efficiency of SMBI exhibited a week dependence on the backing pressure and injection direction (high- and low-side injections). The backing pressure is 0.2 ~ 0.6 MPa. The injection frequency is less than 10 Hz and the pulse length of one pulse is ~2 ms. It was also reported that the fueling efficiency defined as a ratio of increase in the total electron number to the injected electron number was estimated to be ~20% when it was assumed that the density increases uniformly in the whole plasma and ~50 % when it was assumed that the density increases only in the peripheral region (r/a = 0.96 – 1.0). The fueling efficiency of SMBI was higher than that of GP. The plasma response for SMBI was also faster than that for GP.

- **SMBI in Heliotron J**

  SMBI has been installed on Heliotron J (V_p ~ 0.7 m^3) [38,39]. Heliotron J is a helical type device. It was reported that the fueling efficiency is estimated to be about 50 – 60 % for NBI and 20 – 30 % for ECH + NBI discharges at $\overline{n_e} \sim 1 \times 10^{19}$ m^{-3}. The stored energy reached ~4.5 kJ for ECH + NBI with SMBI fueling, which is about 50 % higher than the maximum one achieved so far under the similar heating condition with conventional gas puffing fueling [39].

- **SPGI in ASDEX-U**

  SPGI has been installed in ASDEX-U tokamak (V_p ~ 13 m^3) [40,41]. The SPGI is the same type of SPGI installed in Tore Supra. The fueling efficiency is ~30% for L-mode and low density H-mode plasmas. In contrast, the fueling efficiency is reduced to less than 15% in high density H-mode discharge [40]. The possibility of type-I edge localized modes (ELMs) pacing in H-mode plasmas by 2 Hz gas injection was investigated in ASDEX-U [41].

- **SGI-U in NSTX**

  Supersonic gas injector upgrade (SGI-U) has been installed in NSTX tokamak (V_p ~ 12.5 m^3) [42, 43]. The SGI-U device consists of a small converging diverging graphite Laval nozzle and a piezoelectric gas valve. The backing pressure is up to 5000 Torr (~0.7 MPa). High fueling efficiency (10 ~ 40%), which was estimated by the ratio of the total electron inventory N_e differentiated with time to the particles supply by SGI-U, was obtained [43].

The plasma volumes of JT-60U and Tore supra are similar to that of LHD. These devices are tokamaks. There is no disruption in helical plasma and therefore the edge density can be significantly increased by supplying particles with a large flow rate. The

maximum amount of particles supplied by SSGP in LHD is ~ 13.6 Pam^3/pulse (#108184) while that of SMBI in JT-60U is 1.5 Pam^3/pulse [6]. Since the plasma volume of LHD is larger than that of Heliotron J, the fueling characteristics of SSGP applied to large helical plasma are able to be investigated in this study.

1.5 Objective of this study

Establishment of fueling methods is one of the critical issues for the realization of a fusion reactor. Two fueling methods of gas puffing and pellet injection have been studied for a long time. The objective of this study is to investigate fueling characteristics of SSGP applied to large high-temperature helical plasmas in LHD.

Since detailed radial profiles can be measured in LHD, the fueling characteristics can be studied based on the analysis of electron density profile data.

In addition, various phenomena are induced by SSGP, such as the reheat of the plasma stored energy, the strong edge cooling and the nonlocal transport. The electron temperature fluctuations related to the MHD instability are induced after the nonlocal phenomenon. SSGP is also capable of inducing the fast density modulation externally by using fast pulse train. These plasma physics experiments using SSGP are also discussed in this study.

The convergence of gas flow plays an important role in these experiments. An effectiveness of a Laval nozzle in generating the convergent gas flow has been tested by visualizing the gas flow. Three methods have been applied for visualization, i.e., the shadow graph imaging, the emission imaging using electron beam, and the laser scattering after forming the cluster beam. The convergences of gas flow with and without the Laval nozzle have been investigated using these methods. As a result, the effectiveness of the Laval nozzle has been revealed in this study.

1.6 Outline of this thesis

After introducing the first chapter (this chapter), Chapter 2 describes the basic physics of supersonic gas puffing, and the experiments results on convergence of supersonic gas flow or cluster beam. The fueling characteristics of SSGP applied to large high-temperature plasma in LHD are discussed in Chapter 3. In Chapter 4, the results of plasma physics experiments using SSGP are presented. Finally, the summary and conclusions are given in Chapter 5.

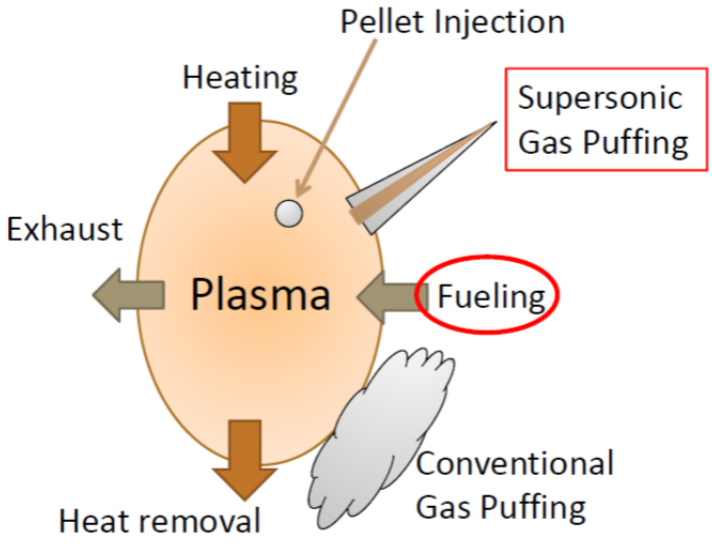

Fig. 1.1 Schematic view of heat and particles controls in fusion DEMO reactor. Images of three fueling methods are also shown.

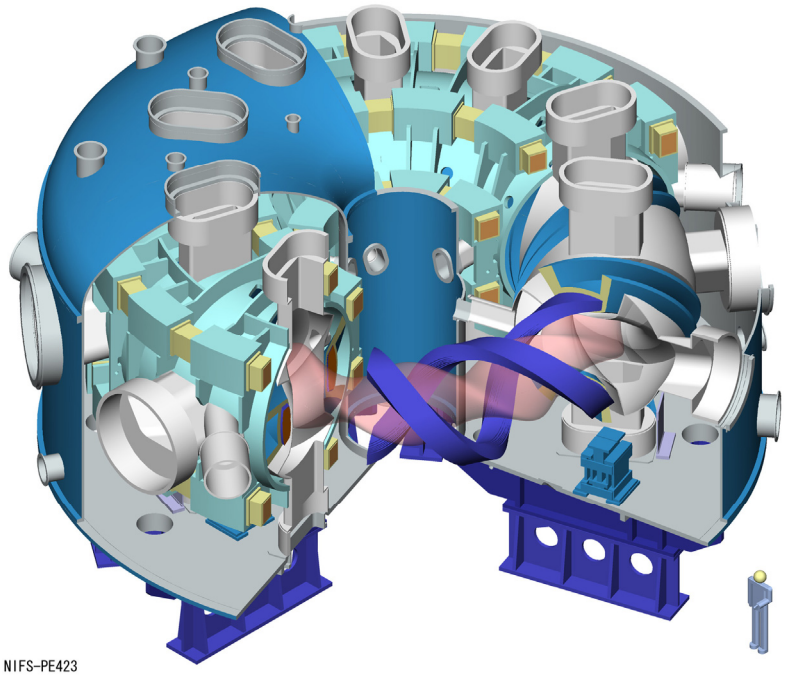

Fig. 1.2 Bird's-eye view of LHD [44]. LHD is the world's-largest superconducting heliotron device.

Bibliography of Chapter 1

[1] UN, World Population Prospects: The 2010 Revision, http://esa.un.org/unpd/wpp/Excel-Data/population.htm.

[2] R. D. Hazelitine and J. D. Meiss, "Plasma Confinement" Chapter 1.3 p.3 Addison-weslet publishing company. (1992).

[3] ITER project http://www.iter.org/.

[4] H. Takenaga et al., J. Nucl. Mater. **390-391**, 869 (2009).

[5] C. Angioni et al., Phys. Rev. Lett. **90**, 205003 (2003).

[6] H. Weisen et al., Plasma Phys. Control. Fusion **48**, A457 (2006).

[7] J. Miyazawa et al., Nucl. Fusion **44**, 154 (2004).

[8] J. Miyazawa et al., J. Nucl. Mater. **313-316**, 534 (2003).

[9] B. J. D. Tubbingb et al., Nucl. Fusion **32**, 967 (1992).

[10] C. A. Foster et al., Nucl. Fusion **17**, 1067 (1977).

[11] R. Sakamoto et al., Nucl. Fusion **41**, 381 (2001).

[12] N. Ohyabu et al., Phys. Rev. Lett. **97**, 055002 (2006).

[13] R. Sakamoto et al., Nucl. Fusion **46**, 884 (2006).

[14] A. Murakami et al., Plasma Fusion Res. **5**, S1032 (2010).

[15] A. Murakami et al., J. Plasma Fusion Res. SERIES **9**, 979 (2010).

[16] John Wesson, "Tokamaks", Chapter 7.7, p. 374, Clarendon Press – Oxford, (2004).

[17] A. Iiyoshi et al., Nucl. Fusion **39**, 1245 (1999).

[18] O. Motojima et al., Phys. Plasmas **6**, 1843 (1999).

[19] Y. Yoshimura et al., J. Phys. Conf. Ser. **25**, 189 (2005).

[20] T. Shimozuma et al., Fusion Eng. Des. **53**, 525 (2001).

[21] T. Mutoh et al., Phys. Rev. Lett. **85**, 4530 (2000).

[22] T. Watari et al., Nucl. Fusion **41**, 325 (2001).

[23] Y. Takeiri et al., Rev. Sci. Instrum. **70**, 4260 (1999).

[24] K. Narihara et al., Rev. Sci. Instrum. **72**, 1122 (2001).

[25] I. Yamada et al., Fusion Sci. Tech **58**, 345 (2010).

[26] K. Kawahata et al., Rev. Sci. Instrum. **70**, 707 (1999).

[27] J. Miyazawa et al., Fusion Eng. Des. **83**, 265 (2008).

[28] L. Yao et al., Nucl. Fusion **38**, 631 (1998).

[29] L. Yao et al., Nucl. Fusion **41**, 817 (2001).

[30] L. Yao et al., Nucl. Fusion **44**, 420 (2004).

[31] L. Yao et al., Nucl. Fusion **47**, 1399 (2007).

[32] X. R. Duan et al., Nucl. Fusion **50**, 095011 (2010).

[33] C. Y. Chen et al., J. Plasma Fusion Res. SERIES **9**, 37 (2010).

[34] B. Pegourie et al., J. Nucl. Mater. **313-316**, 539 (2003).

[35] J. Bucalossi et al., 19th IAEA conf. Lyon, WX/P4-04, (2002).

[36] H. Takenaga et al., Nucl. Fusion **49**, 075012 (2009).

[37] H. Takenaga et al., Nucl. Fusion **50**, 115003 (2010).

[38] T. Mizuuchi et al., Contrib. Plasma Phys. **50**, NO.6-7, 639 (2010).

[39] T. Mizuuchi et al., J. Nucl. Materials **415**, S443 (2011).

[40] J. Bucalossi et al., Proc. 31st EPS Conference on Plasma phys. London, ECA 28G P-4. 115 (2004).

[41] P. T. Lang et al., Plasma Phys. Control. Fusion **47**, 1495 (2005).

[42] V. A. Soukhanovskii et al., Rev. Sci. Instrum. **75**, 4320 (2004).

[43] V. A. Soukhanovskii et al., Proc. 35th EPS Conference on plasma phys. Greece, P2. 109 (2008).

[44] NIFS HP, http://www.lhd.nifs.ac.jp/lhd/limit/cad/LHD_cut/PE423.JPG.

Chapter 2

Development of supersonic gas puffing

2.1 Theoretical backgrounds

2.1.1 Theory of supersonic gas flow

Supersonic gas flow is generated from a “Laval nozzle”. In this section, the theory of supersonic gas flow is described.

The stream-tube, where the cross section area A to vary with distance x, is assumed, as illustrated in Fig. 2.1. The steady flow, where the cross section area, A, the pressure, p, the density, n_f, and the velocity, v are functions of x only, is defined as quasi-one-dimensional flow. One the other hand, in the case of one-dimensional flow that is treated as strictly constant-area flow, three physical mechanisms, such as a normal shock, heat addition and/or friction, cause the flow properties to change with x even though the area constant [1]. Although the actual physical flow through the variable-area duct is three-dimensional, in the case of quasi-one-dimensional flow, the flow properties described as a function of x. This is due to assuming that the flow properties are uniform across any given cross section of area A. The quasi-one-dimensional flow is an approximation to the actual physics of the flow.

The continuity equation for steady quasi-one-dimensional flow is derived from the integrated calculation over the control volume, as follows,

$$-\iint_S n_f \mathbf{V} \cdot d\mathbf{S} = \frac{\partial}{\partial t} \iiint_V n_f dV \,, \tag{2.1}$$

when integrated over the control volume in Fig. 2.1 leads, for steady flow, directly to

$$n_{f\,i} v_i A_i = n_{f\,ii} v_{ii} A_{ii} \,. \tag{2.2}$$

Note that in Eq. (2.2) the term $n_{f\,i} v_i A_i$ is the surface integral over the cross section at location 1 and $n_{f\,ii} v_{ii} A_{ii}$ is the surface integral over the cross section at location 2. The surface integral taken over the side of the control surface between location 1 and 2 is zero, because the control surface is a stream tube; Hence $\mathbf{V}$ is assumed oriented along the surface, and hence $\mathbf{V} \cdot d\mathbf{S} = 0$ along the side.

From Eq. (2.2),

$$n_f v A = \text{const} \,. \tag{2.3}$$

Hence,

$$d(n_f v A) = 0 \,. \tag{2.4}$$

The momentum equation for steady quasi-one-dimensional flow is estimated from the integral form of the momentum equation, assuming steady flow and no body forces, as follows,

$$\iint_S (n_f \mathbf{V} \cdot d\mathbf{S})\mathbf{V} + \iiint_V \frac{\partial (n_f \mathbf{V})}{\partial t} dV = \iiint_V n_f \mathbf{f} dV - \iint_S p d\mathbf{S} \,, \tag{2.5}$$

$$p_i A_i + n_{f\,i} v_i^{\,2} A_i + \int_{A_i}^{A_{ii}} p dA = p_{ii} A_{ii} + n_{f\,ii} v_{ii}^{\,2} A_{ii} \,. \tag{2.6}$$

To obtain a differential form of the momentum equation, apply Eq. (2.6) to the infinitesimal control volume sketched in Fig. 2.2, where the length in the *x* direction is *dx*:

$$pA + n_f v^2 A + n_f dA = (p + dp)(A + dA) + (n_f + dn_f)(v + dv)^2 (A + dA) \,. \tag{2.7}$$

Dropping all second-order terms involving products of differentials, this becomes

$$A dp + A v^2 dn_f + n_f v^2 dA + 2 n_f v A dv = 0 \,. \tag{2.8}$$

Expanding Eq. (2.4), and multiplying by v,

$$n_{\mathrm{f}} v^2 dA + n_{\mathrm{f}} v A dv + A v^2 dn_{\mathrm{f}} = 0 \,. \tag{2.9}$$

Subtracting this equation from Eq. (2.8), we obtain

$$dp = -n_{\mathrm{f}} v dv \,. \tag{2.10}$$

From Eq. (2.4),

$$\frac{dn_{\mathrm{f}}}{n_{\mathrm{f}}} + \frac{dv}{v} + \frac{dA}{A} = 0 \tag{2.11}$$

.

To eliminate $dn_{\mathrm{f}} / n_{\mathrm{f}}$ from Eq. (2.11), consider Eq. (2.10)

$$\frac{dn_{\mathrm{f}}}{n_{\mathrm{f}}} = \frac{dp}{dn_{\mathrm{f}}} \frac{dn_{\mathrm{f}}}{n_{\mathrm{f}}} = -v dv \tag{2.12}$$

.

There are no dissipative mechanisms such as friction, thermal conduction, or diffusion acting on the flow. Thus, the flow is isentropic. Hence, any change in pressure, dp, in the flow is accompanied by a corresponding isentropic change in density, dn_{f}. Therefore, we can write,

$$\frac{dp}{dn_{\mathrm{f}}} = \left(\frac{\partial p}{\partial n_{\mathrm{f}}} \right)_s = {v_{\mathrm{s}}}^2 \tag{2.13}$$

,

where v_{s} is the sound speed. Eq. (2.13) is a fundamental expression for the speed of sound. Combining Eqs. (2.12) and (2.13),

$${v_{\mathrm{s}}}^2 \frac{dn_{\mathrm{f}}}{n_{\mathrm{f}}} = -v dv$$

,

$$\frac{dn_{\mathrm{f}}}{n_{\mathrm{f}}} = -\frac{v dv}{{v_{\mathrm{s}}}^2} = -\frac{v^2 dv}{{v_{\mathrm{s}}}^2 v} = -M^2 \frac{dv}{v} \tag{2.14}$$

,

where M is Mach number which is defined by $M = v / v_s$. Substituting Eq. (2.14) into Eq. (2.11),

$$\frac{dA}{A} = \left(M^2 - 1 \right) \frac{dv}{v} \tag{2.15}$$

.

This equation is called the area-velocity relation and significant equation. It tells us this information:

1. $M \to 0$ (Incompressible flow)

$$\frac{dA}{A} = -\frac{dv}{v} .$$
$$Av = const .$$

This is the familiar continuity equation for incompressible flow.

2. $0 \le M \le 1$ (Subsonic flow)

$$\frac{dA}{A} = -C\frac{dv}{v} \quad (C > 0) .$$
$$dA > 0 \;\Rightarrow\; dv < 0$$
$$dA < 0 \;\Rightarrow\; dv > 0 .$$

The velocity increases in a converging duct and decreases in a diverging duct.

3. $M > 1$ (Supersonic flow)

$$\frac{dA}{A} = C\frac{dv}{v} \quad (C > 0) .$$
$$dA > 0 \;\Rightarrow\; dv > 0$$
$$dA < 0 \;\Rightarrow\; dv < 0 .$$

The velocity increases in a diverging duct and decreases in a converging duct.

4. $M = 1$ (Sonic flow)

$$\frac{dA}{A} = 0 .$$

From the above results, the flow with the speed of the subsonic becomes supersonic speed flow when the flow passes through a minimum radius of the area which is called throat. In contrast, the supersonic flow becomes the subsonic flow when the flow passes through the throat (See Fig. 2.3). That is, in order to obtain the supersonic speed, it is necessary to pass through the throat. “Laval nozzle” is the nozzle to achieve supersonic flow using this property.

Next, a relation equation of the area and Mach number in nozzle is shown as follows. Consider the duct shown in Fig. 2.4. At the throat, the flow is sonic. Hence,

denoting conditions at sonic speed by an asterisk, we have $M^* = 1$ and $v^* = v_s^*$ at the throat. The area of the throat is A^*. At any other section of the duct, the local area, Mach number, and velocity are A, M, and v, respectively. Apply Eq. (2.2) between these two locations:

$$n_f^* v^* A^* = n_f v A \tag{2.16}$$

Since $v^* = v_s^*$, Eq. (2.16) becomes

$$\frac{A}{A^*} = \frac{n_f^*}{n_f}\frac{v_s^*}{v} = \frac{n_f^*}{n_{f0}}\frac{n_{f0}}{n_f}\frac{v_s^*}{v}, \tag{2.17}$$

where n_{f0} is the stagnation density, $n_{f0} = p_s / R_G T_s$, and is constant throughout the isentropic flow. The ratio of total to static density at a point in the flow as a function of Mach number M at that point is given as follows [2],

$$\frac{n_{f0}}{n_f} = \left(1 + \frac{\gamma - 1}{2} M^2\right)^{1/(\gamma-1)}, \tag{2.18}$$

and apply this to sonic conditions, we have

$$\frac{n_{f0}}{n_f^*} = \left(\frac{\gamma + 1}{2}\right)^{1/(\gamma-1)}. \tag{2.19}$$

Also, by definition, and from a direct relation between the actual Mach number M and the characteristics Mach number M^*,

$$\left(\frac{v}{v_s^*}\right)^2 = M^{*2} = \frac{\frac{\gamma+1}{2}M^2}{1 + \frac{\gamma-1}{2}M^2}. \tag{2.20}$$

Squaring Eq. (2.17), and substituting Eqs. (2.18), (2.19), and (2.20), we have

$$\left(\frac{A}{A^*}\right)^2 = \left(\frac{n_f^*}{n_{f0}}\right)^2 \left(\frac{n_{f0}}{n_f}\right)^2 \left(\frac{v_s^*}{v}\right)^2,$$

$$\left(\frac{A}{A^*}\right)^2 = \left(\frac{2}{\gamma+1}\right)^{2/(\gamma-1)} \left(1 + \frac{\gamma-1}{2}M^2\right)^{2/(\gamma-1)} \left(\frac{1 + \frac{\gamma-1}{2}M^2}{\frac{\gamma+1}{2}M^2}\right),$$

$$\frac{A}{A^*} = \frac{1}{M}\left[\frac{2}{\gamma+1}\left(1+\frac{\gamma-1}{2}M^2\right)\right]^{(\gamma+1)/2(\gamma-1)} \tag{2.21}$$

Equation (2.21) is called the area-Mach number relation. The Mach number at any location in the duct is a function of the ratio of the local duct area to the sonic throat area.

2.1.2 Design of Laval nozzle

Our Laval nozzles were designed referring NACA technical note [3]. Especially, a part of method of Foelsch was used in this design. Design of Laval nozzle is divided into three sections. First section is upstream of the throat. This section is arbitrary curved line. Other two sections are important for the Laval nozzle. Second section is called expansion section where expansion wave is generated and propagate across the flow downstream reflecting from the opposite wall. Third section is called straightening section where all the expansion waves generated by the expansion section are canceled. The point of junction of the expansion section and straightening section is called a "inflection point". The angle of the duct wall at inflection point is largest in the all section of the Laval nozzle. (See Fig. 2.5)

Before design, the diameter of throat, d, the Mach number of the design value, M_t and the angle of the inflection point, θ_1 were determined. Typical design parameters of Laval nozzle for SSGP are d = 0.3 mm, M_t = 8 and θ_1 = 12°, respectively.

Firstly, the design of the expansion section is described. Although the curve line of the expansion section is also arbitrary, the coordinate at inflection point, (x_1, y_1), have to be determined. The cross section area at the throat, A^* is πy^{*2}, where y^* denotes the radius of throat. The streamline through (x_1, y_1) is radial surface. The cross section area of the radial surface, A_1, is as follows,

$$A_1 = 2\pi r_1^2\left(1-\cos\theta_1\right) \tag{2.22}$$

From Fig. 2.6,

$$r_1 \sin\theta_1 = y_1 \quad , \tag{2.23}$$

$$\frac{A_1}{A^*} = \frac{2r_1^2}{y^{*2}}\left(1-\cos\theta_1\right) \quad . \tag{2.24}$$

Hence,

$$y_1 = y^* \sqrt{\frac{A_1}{A^*}\frac{\sin^2\theta_1}{2\left(1-\cos\theta_1\right)}} \tag{2.25}$$

This is the *y*-coordinate of the inflection point. However, A_1/A^* is unknown now. When the nozzle is axial symmetry, the velocity at the inflection point, v_1 is related to θ_1 as follows,

$$v_1 = v_t - 2\theta_1, \tag{2.26}$$

where v_t is Prandtl-Meyer function,

$$v_t = \sqrt{\frac{\gamma+1}{\gamma-1}}\tan^{-1}\sqrt{\frac{\gamma-1}{\gamma+1}\left(M^2-1\right)} - \tan^{-1}\sqrt{M^2-1}\,. \tag{2.27}$$

The Mach number at the inflection point, M_1, is also estimated from Eq. (2.26) and (2.27).

$$\begin{aligned}&\sqrt{\frac{\gamma+1}{\gamma-1}}\tan^{-1}\sqrt{\frac{\gamma-1}{\gamma+1}\left(M^2-1\right)} - \tan^{-1}\sqrt{M^2-1} - 2\theta_1 \\ &= \sqrt{\frac{\gamma+1}{\gamma-1}}\tan^{-1}\sqrt{\frac{\gamma-1}{\gamma+1}\left(M_1^{\,2}-1\right)} - \tan^{-1}\sqrt{M_1^{\,2}-1}\end{aligned} \quad . \tag{2.28}$$

A_1/A^* is calculated by Eq. (2.21), substituting M_1.

$$\frac{A_1}{A^*} = \frac{1}{M_1}\left[\frac{2}{\gamma+1}\left(1+\frac{\gamma-1}{2}M_1^{\,2}\right)\right]^{(\gamma+1)/2(\gamma-1)} \tag{2.29}$$

The curve line of the expansion section is given by the Foelsh method in Ref. [3], as a third-order function,

$$y = y^* + \frac{\tan\theta_1}{x_1} x^2 \left(1 - \frac{x}{3x_1} \right). \tag{2.28}$$

Substituting $(x, y) = (x_1, y_1)$ to Eq. (2.28) and solving the equation for x_1,

$$x_1 = \frac{3}{2} \frac{\left(y_1 - y^* \right)}{\tan\theta_1}. \tag{2.29}$$

This is the x-coordinate of the inflection point.

Next, the design of straightening section is shown as follows. The assumptions of this method, or rather its boundary conditions, may be variously stated:

(1) Along the Mach line emanating from the inflection point, the velocity vectors are co-original,

(2) the Mach number is constant along the arc of the circle which passes through the inflection point of the wall perpendicularly (and obviously its center is the origin of the velocity vectors),

(3) in the region between this arc and the Mach line from the inflection point, the Mach number is a function solely of the radius from the vector origin.

The radius of vector at the throat, r^* is as follows,

$$r^* = \sqrt{\frac{A^*}{A_1}} r_1. \tag{2.23}$$

The minim step of the Mach number is determined as the step number of 500,

$$\Delta M = \frac{M_t - M_1}{500}, \tag{2.24}$$

where M_t is the Mach number of the design value. The angle at the point of P is estimated from next equation, substituting the Mach number,

$$\theta = \frac{\nu_t - \nu(M)}{2}. \tag{2.25}$$

The relation is given by continuity equation from Fig. 2.7, as follows

$$2\pi r^2 \left(\cos\theta - \cos\theta_1 \right) = \pi \left[l \sin\left(\theta + \alpha_0 \right) + r \sin\theta + \left(r + l\cos\alpha_0 \right) \sin\theta \right] l \sin\alpha_0, \tag{2.26}$$

where α_0 is the Mach angle at the point P. The left-hand side of this equation means the

area formed by the arc between the points of P and P'. In contrast, the right-hand side of this equation means the area of side of the circular truncated cone, where the side surface is formed by the points of Q and Q'. This equation can be solved for the length between the points of P and Q, l, as follows,

$$l = \frac{2r\sin\alpha_0\sin\theta - \sqrt{4r^2\sin^2\alpha_0\sin^2\theta - 4\left(2r^2\cos\theta - 2r^2\cos\theta_1\right)\left(-\cos\alpha_0\sin\alpha_0\sin\theta - \sin\alpha_0\sin(\alpha_0+\theta)\right)}}{2\left(-\cos\alpha_0\sin\alpha_0\sin\theta - \sin\alpha_0\sin(\alpha_0+\theta)\right)} \tag{2.27}$$

The coordinate, (x, y), in straightening section are determined by l,

$$x = r\cos\theta + l\cos(\theta+\alpha_0) + (x_1 - r_1\cos\theta_1) \tag{2.28}$$

$$y = l\sin(\theta+\alpha_0) + r\sin\theta \tag{2.29}$$

This is the points of the straightening section. We have to calculate until the end of exit hole of Laval nozzle. At the inflection point, the length of l needs to be the minimum value.

Figure 2.8 shows cross sections of the three Laval nozzles of 0.1, 0.3 and 0.6 mm throat diameter designed for the SSGP device. These nozzles are similarly designed to generate a gas flow of $M_t = 8$ and the inflection angle of 12^o. Figure 2.9 shows an image of Laval nozzle of 0.3 mm throat diameter. An improved Laval nozzle is described in the section 2.5 and 3.4.

2.1.3 Visualizing of supersonic gas flow and cluster theory

Before applying SSGP to LHD, the effectiveness of the Laval nozzle has been tested by visualizing the gas flow. Three methods have been applied for visualization, i.e., the shadow graph imaging, the emission imaging using electron beam, and the laser scattering after forming the cluster beam.

The cluster beam is formed by selecting the gas species, or by cooling the gas using a refrigerator. Physics of cluster formation by gas jet has been studied since 1956

[4]. A cluster beam for fusion research was studied firstly as the source of plasma heating in the 1970s [5]. Cluster jet injection (CJI) comes to the front again in recent study of fueling [6]. The CJI, where liquid nitrogen of 77 K is used for gas cooling, has been developed for HL-2A. Supersonic gas injector (SGI) has been developed for NSTX, where a Laval nozzle is used to generate supersonic gas jet [7].

There is no established theory to predict the cluster size in a free jet expansion. Nevertheless, it has been shown that the condition to produce clusters can be described by an empirical scaling parameter Γ* that is proportional to a so-called "Hagena parameter", k [8, 9]

$$\Gamma^* = k\frac{(d/\tan\alpha)^{0.85}}{T_0^{2.29}}P_0 \tag{2.30}$$

where d is the nozzle diameter in μm, α is the expansion half angle (α = 45° for the sonic case, α < 45° for the supersonic case), P_0 is the backing plenum pressure in 10^{-4} MPa, and T_0 is the pre-expansion temperature in Kelvin. Massive condensation, where the cluster size exceeds 100 atoms/cluster, is generally observed for Γ* > 1000 [8, 9].

The parameter Γ* as a function of the gas temperature is shown in Fig. 2.10, where d = 500 μm, α = 45°, and P_0 = 4 MPa are assumed, respectively. The nozzle diameter of d = 500 μm is equal to that of the solenoid valve used in next section study. In this calculation, species-dependent k of 184, 3.85, 2360, 528, 185, and 1650 are used for H_2, He, CH_4, N_2, Ne, and Ar, respectively [8]. The result implies that the gasses except He are expected to form clusters at a room temperature.

Characteristics of cluster beam ejected from the solenoid valve without the Laval nozzle is described in Section 2.2. In section 2.3, results of the H_2 cluster jet using the Laval nozzle of 0.3 mm throat diameter for SSGP are described. The convergence of gas flow from the Laval nozzle is discussed using results of the shadow graph imaging and the emission imaging using electron beam in section 2.4. Installation of SSGP device in LHD is shown in section 2.5. Finally, these are summarized in section 2.6.

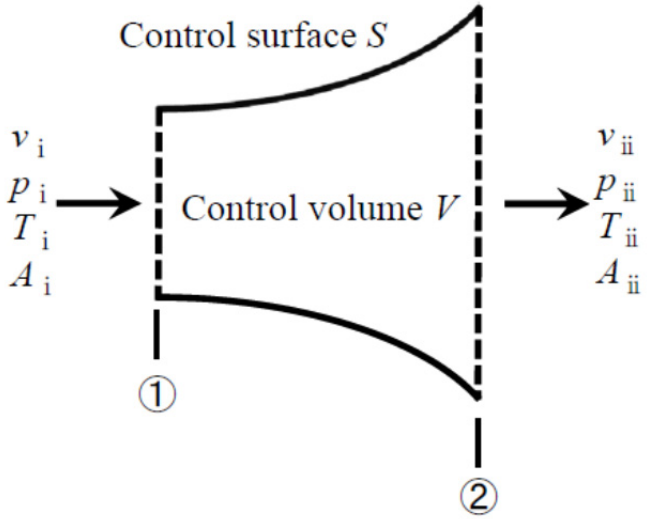

Fig. 2.1 The model of quasi-one-dimensional flow.

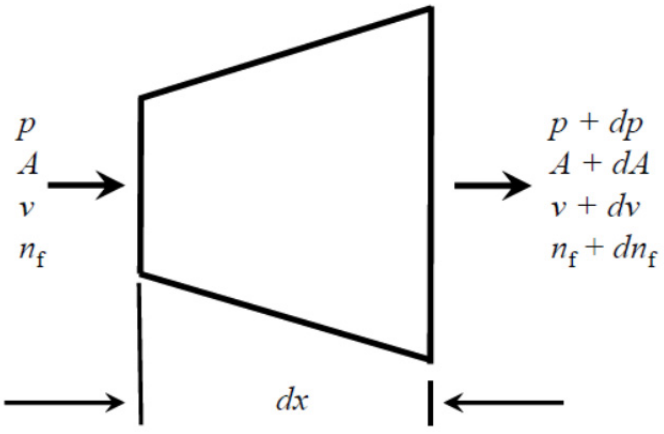

Fig. 2.2 Incremental volume.

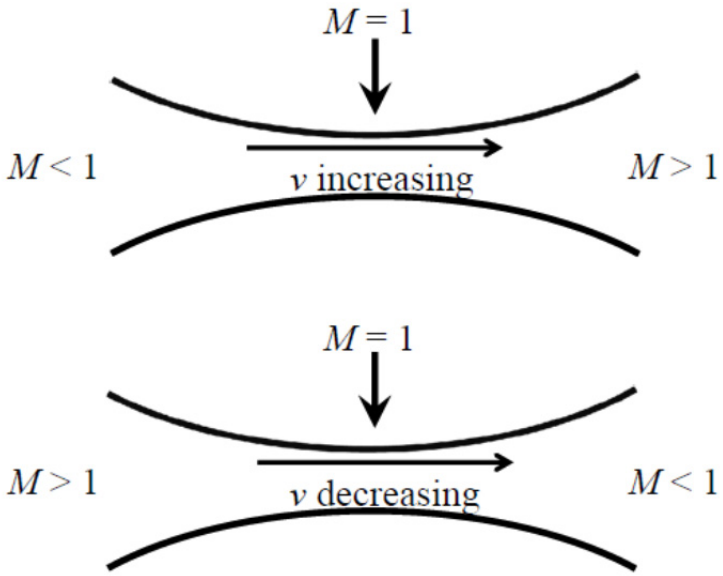

Fig. 2.3 Flow in a convergent-divergent duct.

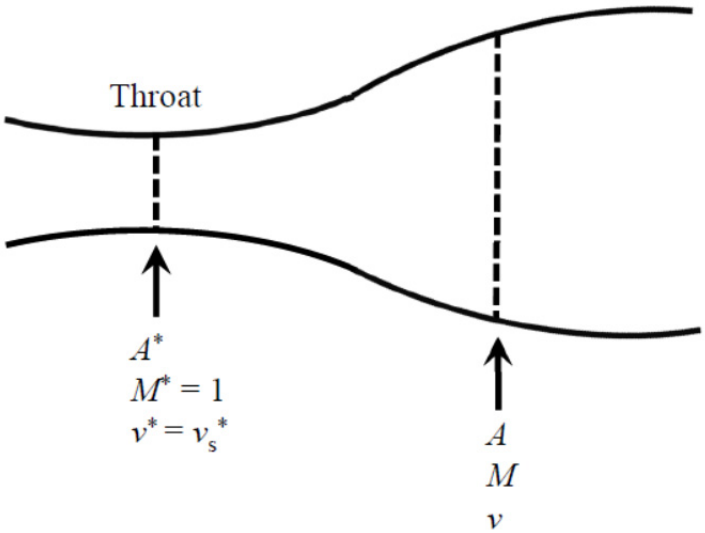

Fig. 2.4 Geometry for derivation of the area Mach number relation.

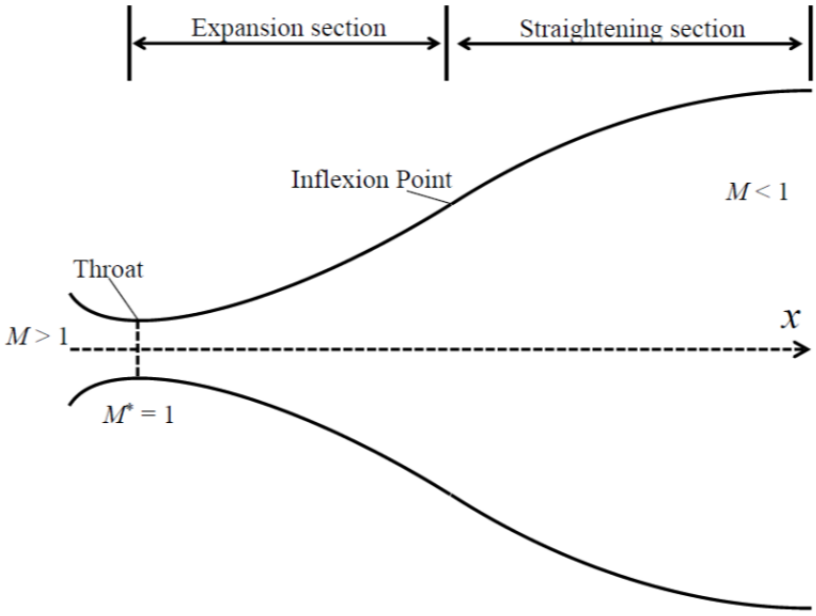

Fig. 2.5 Sketch of Laval nozzle.

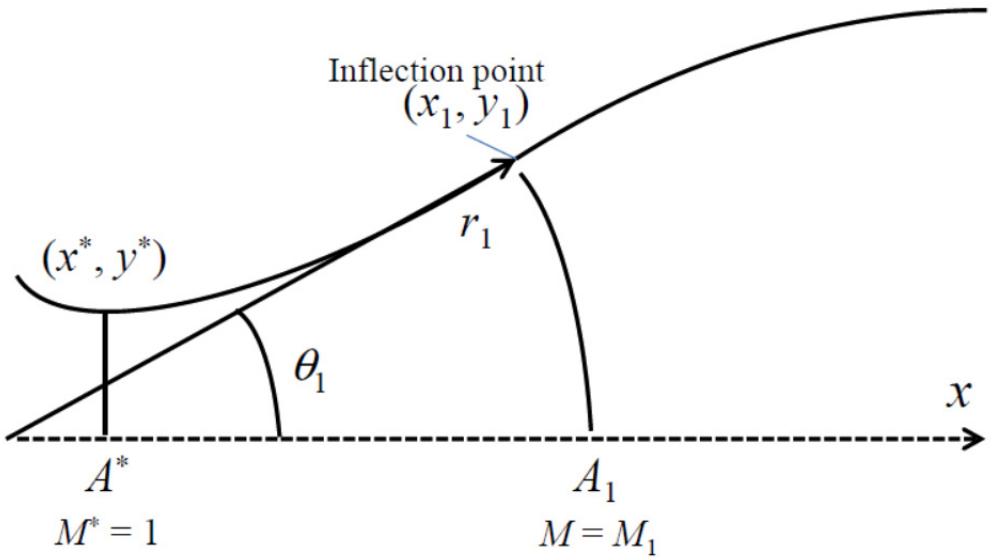

Fig. 2.6 Design of expansion section.

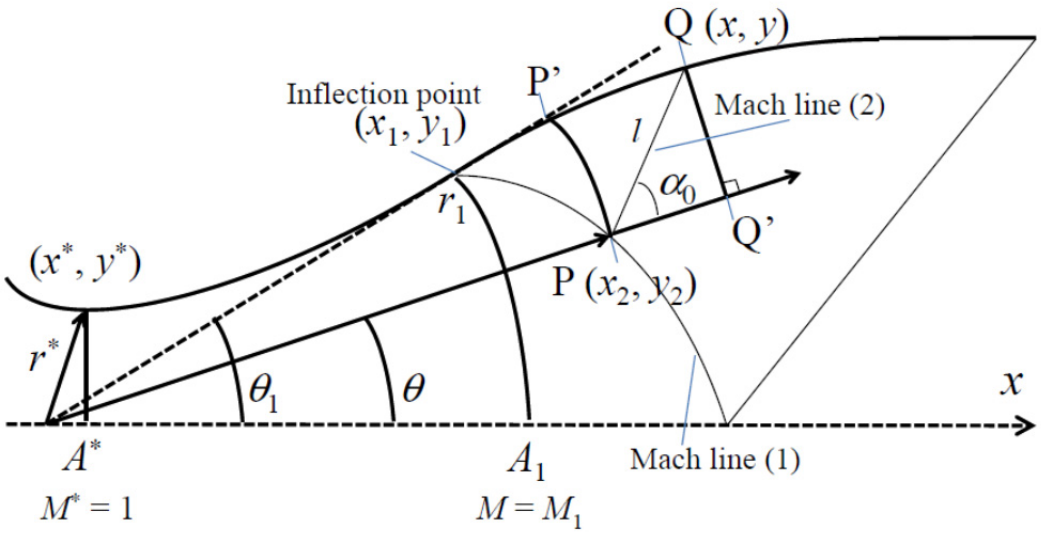

Fig. 2.7 Design of straightening section.

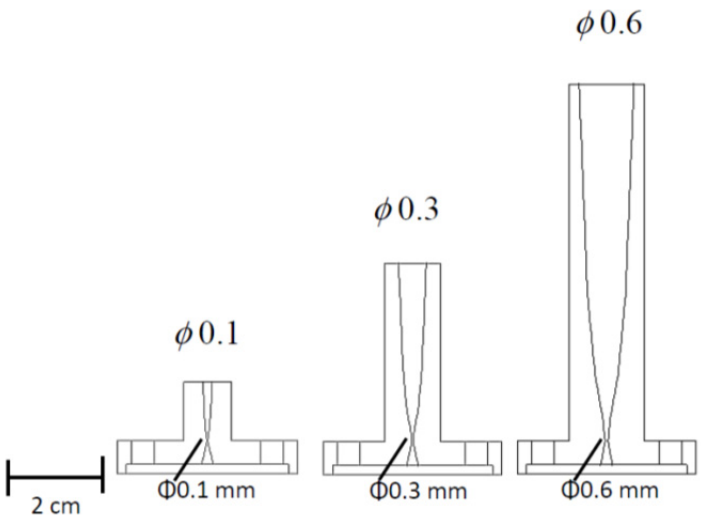

Fig. 2.8 Cross sections of the three Laval nozzles installed in the SSGP device. These nozzles are similarly designed to generate a gas flow of $M_t = 8$.

Fig. 2.9 Image of Laval nozzle with 0.3 mm throat diameter.

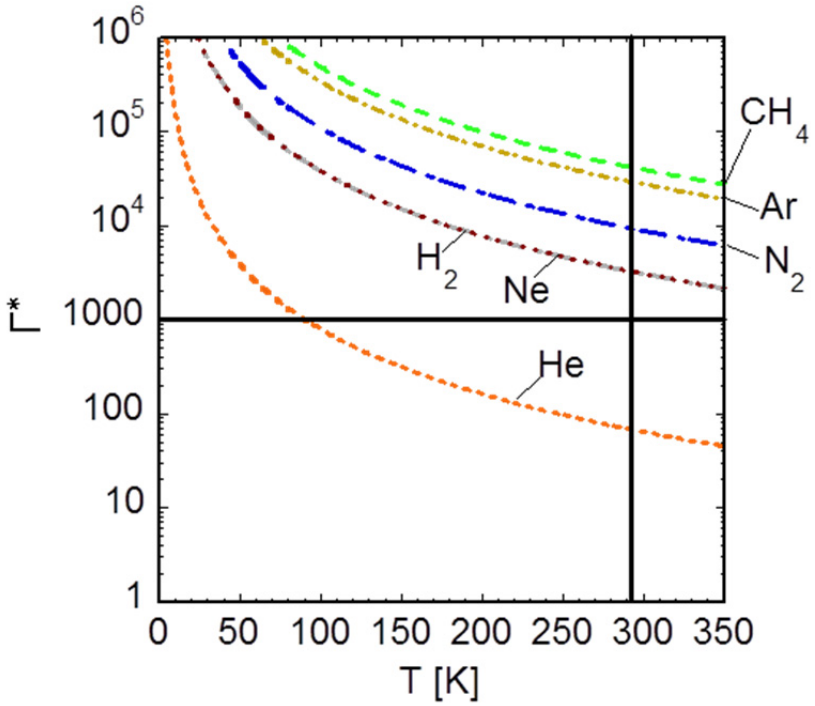

Fig. 2.10 Calculated results of the scaling parameter Γ^*, where d = 500 μm, α = 45°, P_0 = 4 MPa. The gasses except helium satisfy the condition for massive condensation of $\Gamma^* > 1000$ at room temperature (293 K).

2.2 Characteristics of solenoid valve

2.2.1 Mechanism of solenoid valve

A solenoid valve of Parker-Hannifin Pulse Valve 99 Series has been chosen for SSGP. Figure 2.11 shows the image of the solenoid valve. A similar valve is installed in HL-2A tokamak for SMBI [6]. The maximum pressure of the solenoid valve is up to 8 MPa. The minimum pulse length is ~0.1 ms. On the other hand, piezo-electrical valves are used in the conventional gas puffing (GP). In a typical case of piezo-electric valves, the maximum backing pressure is ~0.6 MPa and the minimum pulse length is ~1 ms [10]. While the piezo-electric valve is driven by the motion of a piezo-electric element, the solenoid valve is driven by the electrical magnetic force to open a poppet. The voltage of 250 V is applied for the first 30 μs and the voltage of 30 V is applied until the end of the pulse length. The material of poppet is TEFLON. The cross section of solenoid valve is shown in Fig. 2.12. Comparison between the conventional gas puffing and SSGP is shown in Table 2.1. A solenoid valve for SSGP has been tested at a room temperature in a test vacuum chamber. In this section, the convergence of gas flow ejected from the solenoid valve without the Laval nozzle has been revealed. Various gasses shown in Fig. 2.10 were used in the experiment to investigate the clustering condition.

2.2.1 Experimental setup

The experimental setup is shown in Fig. 2.13. A solenoid valve of Parker-Hannifin Pulse Valve Series 99B07 with a 500 μm diameter orifice is used. This valve is equipped with a tapered nozzle and without a Laval nozzle. The available backing pressure is up to 8 MPa. This valve is set inside the vacuum chamber. The pressure in the vacuum chamber is measured by a pressure gauge of MKS Baratron capacitance manometer (MODEL#617A) set at the opposite side of the valve. When the

valve is open, the gas flows from left to right in Fig. 2.13. Various gasses of H_2, He, CH_4, N_2, Ne, and Ar are used in the experiment. A semiconductor laser of NEOARK LDP2-6535A with 650 nm standard wavelength and 35 mW power is set inside the chamber to perpendicularly intersect the gas flow. A beam dump is set at the opposite side of the laser and the valve is rolled by black tape in such a way that the stray light is lowered. The distance between the valve exit and the laser chord is variable from 3.5 mm to 4.0 mm. A fast charge coupled device (CCD) camera of 1280 × 1024 pixels is arranged in the direction perpendicular to both the gas flow and the laser beam. An example CCD image is shown in Fig. 2.14.

The total Rayleigh scattering signal S_{RS} is proportional to the product of the scattering cross section σ and the number density of clusters n_c. The cross section σ is proportional to the square of the averaged cluster size N_c defined by the averaged number of atoms per a cluster. n_c is approximately given by the monomer density before becoming cluster, n_0, divided by N_c, i.e., $n_c \approx n_0/N_c$. The scattering signal S_{RS} is proportional to P_0N_c since the monomer density is proportional to the backing plenum pressure P_0. Farges *et al*. showed that $N_c \propto P_0^{1.8\text{-}2.1}$, assuming a multilayer icosahedral model [11, 12]. This means that the scattered light signal S_{RS} should vary as below,

$$S_{RS} \propto P_0^{2.8-3.1}. \tag{2.31}$$

2.2.2 Results

Figure 2.15 shows the temporal behavior of the scattering signal intensity in the case of Ar. The valve is opened from 0 – 120 ms. The camera exposure time is fixed to 1 ms. The scattered light signal intensity is approximately constant during the valve open. This means that the cluster is formed as long as the valve is open. Hereinafter, the valve opening time of 40 ms and the CCD camera trigger timing of 35 ms are fixed.

Typical scattering signal profiles in the case of CH_4 are shown in Fig. 2.16. The direction y in Fig. 2.16 is parallel to the laser light (see Fig. 2.14). The backing plenum pressure P_0 is varied from 6.0 MPa to 8.0 MPa. While the exposure time of the CCD

camera is fixed to 10 ms. These profiles are axisymmetric and the full-width of half-maximum (FWHM) does not depend on the backing pressure. Similar characteristics are also observed for N_2 and Ar.

Figure 2.17 shows that scattering signal profiles of Ar measured at different position, where the distance from the valve to laser light is varied from 0.23 cm to 1.0 cm. A contour plot of these profiles is shown in Fig. 2.18. The FWHM increases with the distance from the valve. The expansion half angle of 22.5° suggests that this gas flow is supersonic.

The maximum of the scattering signal as a function of the backing pressure is plotted in Fig. 2.19. The scattering signal increases with $\sim P_0^{2.8}$ for Ar (Fig. 2.19 (a)) and $\sim P_0^{3.2}$ for N_2 (Fig. 2.19 (b)). These results are similar to the expectation of Eq. (2.31) and the results in Ref. [8]. However, in the case of CH_4 (Fig. 2.19 (c)), it is found that the backing pressure dependence is stronger than expected, i.e., $S_{RS} \propto P_0^{4.8}$ at $P_0 < 7$ MPa and $S_{RS} \propto P_0^{8.6}$ at $P_0 > 7$ MPa. This result is different from $S_{RS} \propto P_0^{2.8\text{-}3.1}$ (Eq. (2.31)). Farges et al. estimated this relation assuming a multilayer icosahedral model for an Ar cluster. This model seems to be reasonable also for N_2, which shows similar pressure dependence as Ar. However, a new structure model would be necessary to determine the cluster size of CH_4, which shows stronger backing pressure dependence than Ar or N_2.

The scattering signal is detected when the backing plenum pressure is above 3.2 MPa, 3.0 MPa, and 4.0 MPa for CH_4, Ar, and N_2, respectively. In the case of H_2, He, and Ne, no scattering signal has been detected up to 8.0 MPa. Especially, even though the massive condensation condition of $\Gamma^* > 1000$ is satisfied for H_2 and Ne, no cluster has been detected. Even for CH_4, Ar, and N_2 the scattering signals appear at high Γ^* of 31000, 22000, and 9000, respectively. These are much higher than 1000. Possible causes of this might be; the noise level was larger than the scattering signal, or the laser power was too low. In order to detect scattering signals of hydrogen and neon clusters, it would be necessary to improve the experimental setup.

The expansion half angle of 22.5° was confirmed in the case of the solenoid valve without the Laval nozzle in this section.

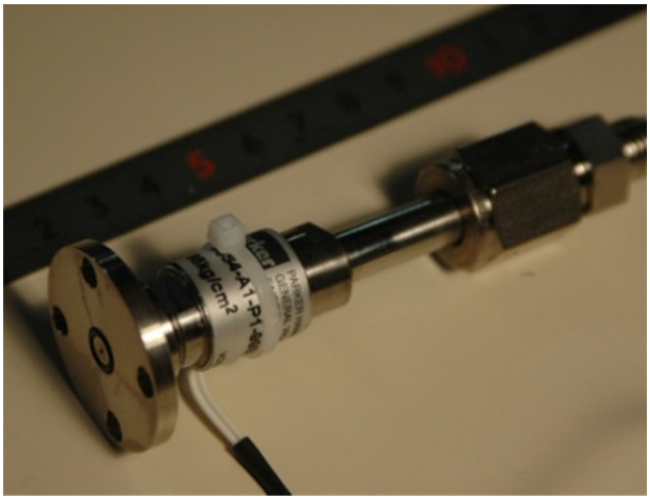

Fig. 2.11 Image of the solenoid valve from Parker-Hannifin Pulse Valve Series for SSGP.

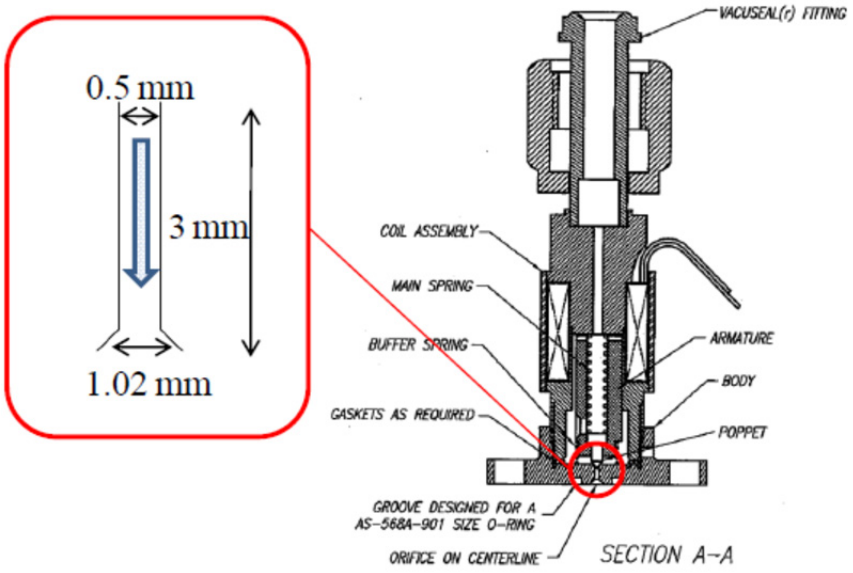

Fig. 2.12 Cross section of the solenoid valve and the enlarge image of the exit of the valve.

	SSGP	**Conventional gas puffing**
Valve	Solenoid valve	Piezo valve
Maximum pressure	8 MPa	~0.6 MPa
Convergence	~5°	~22.5°
Responsive property	Valve open time ~100 μs	Valve open time ~1 ms

Table. 2.1 Table of comparison between SSGP and conventional GP.

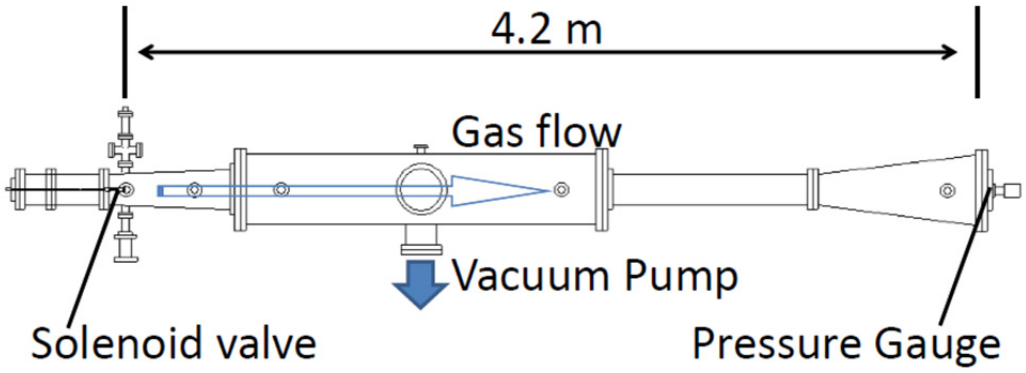

Fig. 2.13 Schematic of the experimental setup. The distance from the solenoid valve to the baratron pressure gauge is 4.2 m. Inside the chamber is pumped to less than 10^{-4} Pa. The laser is set inside the chamber.

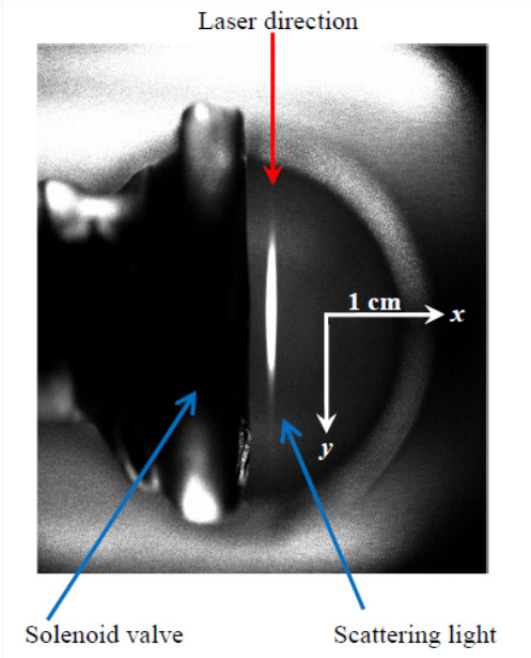

Fig. 2.14 The scattering light image detected by the CCD camera in the case of CH_4. The backing pressure is 8.0 MPa, and the exposure time is 10 ms. The laser beam direction (y) is perpendicular to the gas flow (x).

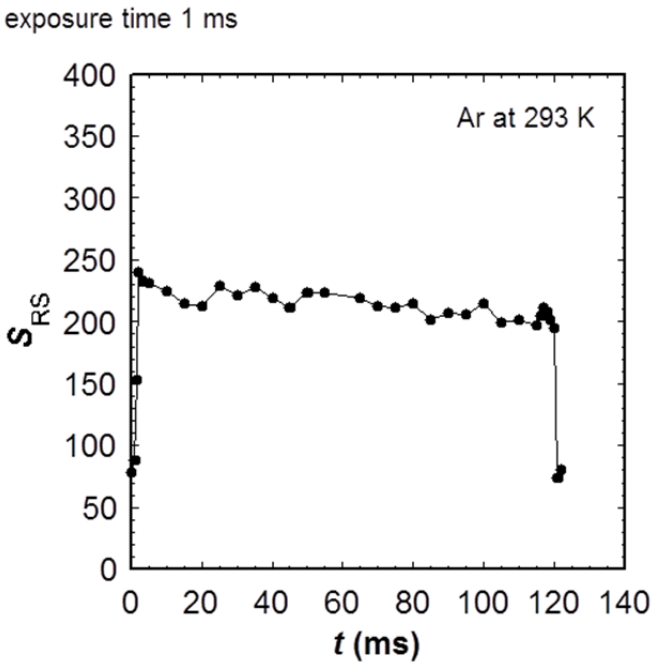

Fig. 2.15 Typical temporal behavior of the scattering signal intensity. The working gas is Ar and the backing pressure is 7.1 MPa.

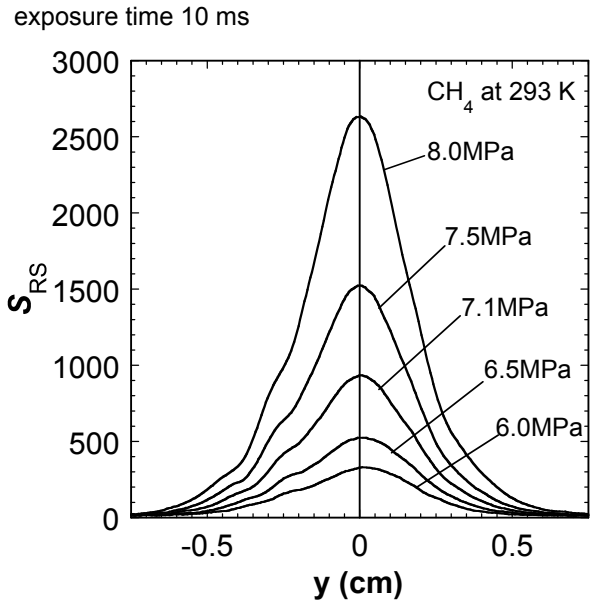

Fig. 2.16 Typical scatter signal profiles in the case of CH_4. The direction y is parallel to the laser light. The backing pressure P_0 is scanned from 6.0 MPa to 8.0MPa, while the gas puff pulse length of 40 ms, the CCD camera trigger timing of 35 ms, and the exposure time of 10 ms are fixed.

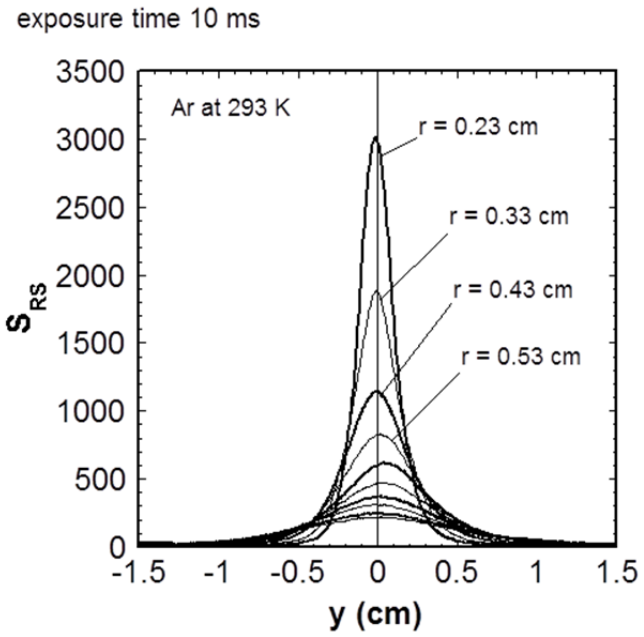

Fig. 2.17 Scatter signal profiles in the case of Ar, where the distance from valves to laser light is varied from 0.23 cm to 1.0 cm. The direction y is parallel to the laser beam.

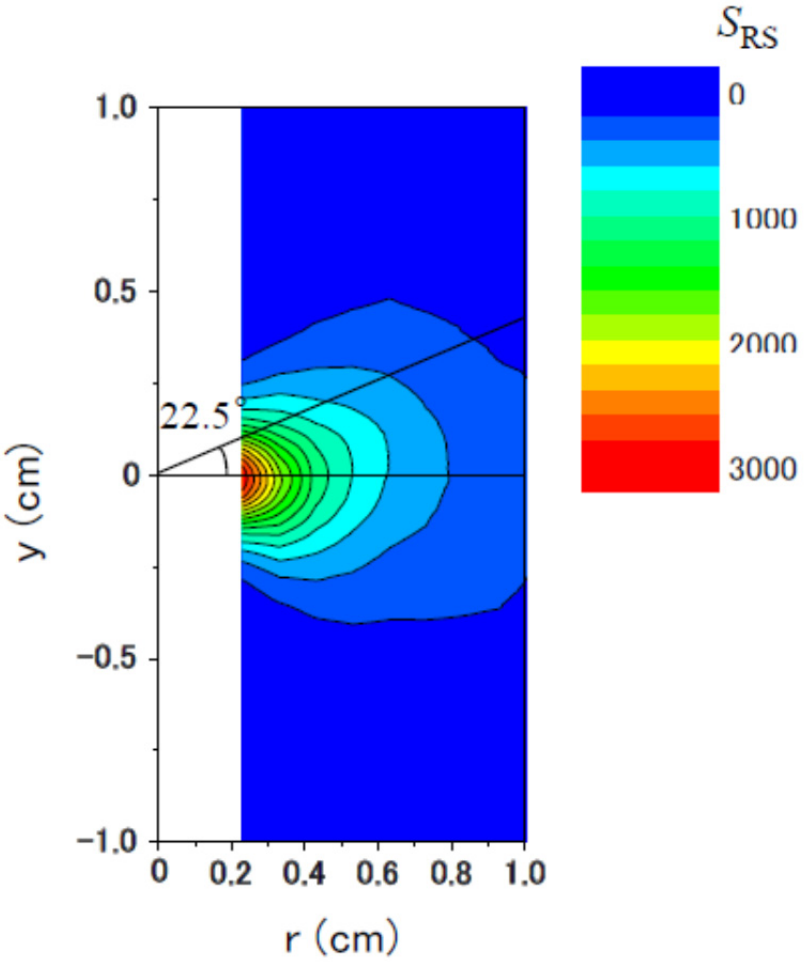

Fig. 2.18 Contour plot of scatter signal profiles shown in Fig. 2.17.

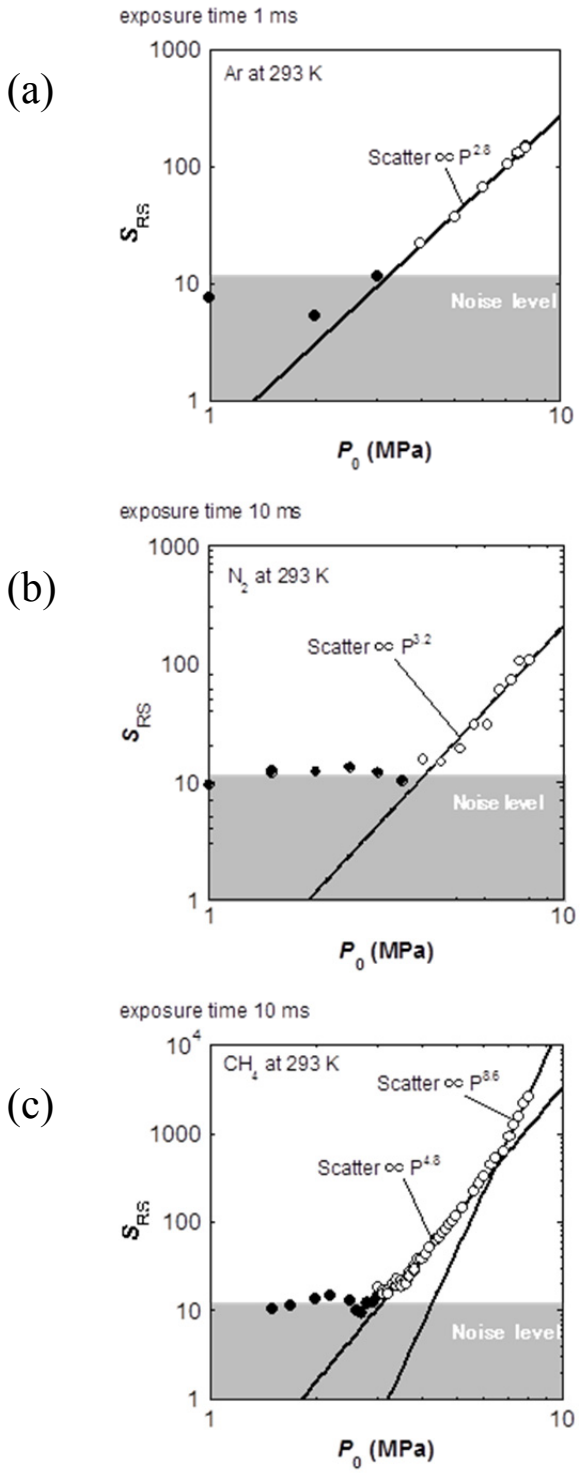

Fig. 2.19 Peak scattered signal as a function of the backing pressure in the cases of (a) Ar, (b) N_2 and (c) CH_4. Closed circles denote the signals under the noise level. Regression analysis has been done using the data points denoted by open circles.

2.3 Characteristics of cluster beam ejected from Laval nozzle

2.3.1 Calculation of hydrogen cluster conditions

In this section, formation of the H_2 cluster jet using a Laval nozzle for SSGP has been investigated in the temperature range from 120 K to 300 K. Time-resolved 2-D images of Rayleigh scattering due to clusters have been measured by a fast charge coupled device (CCD) camera. Characteristics of cluster jet ejected from the Laval nozzle are discussed with regard to dependence on pressure and temperature.

The condition to produce clusters can be described by Eq. (2.30). Massive condensation, where the cluster size exceeds 100 atoms/cluster, is generally observed for $\Gamma^* > 1000$ [8, 9]. Figure 2.20 shows the parameter Γ^* as a function of the gas temperature, where d = 300 μm, α = 12°, P_0 = 4 MPa are assumed, respectively. The nozzle diameter of d = 300 μm and α = 12° are equal to those of the Laval nozzle used in this experimental study. The curve line in the Laval nozzle hole has one inflection point. The angle of α = 12° corresponds to the slope angle of the tangent at the inflection point. It means that the angle of α = 12° is the maximum expansion half angle on the Laval curve line. In this calculation, species-dependent k of 184, 3.85, 2360, 528, 185, and 1650 are used for H_2, He, CH_4, N_2, Ne, and Ar, respectively. Previous study showed that clear scattering signals are observed at high valve backing pressure of more than 3 – 4 MPa at the room temperature in the case of CH_4, N_2, and Ar. Meanwhile, in the case of H_2, He, and Ne, no scattering signal has been detected up to 8.0 MPa at the room temperature [13]. This calculation result shows the parameter Γ^* of H_2 at the temperature region of ~180 K corresponds to that of N_2 at the room temperature. In other words, it implies that H_2 will form clusters when the gas temperature is ~180 K from the room temperature.

2.3.2 Experimental Setup

The experimental setup is shown in Fig. 2.21. The solenoid valve is equipped with the Laval nozzle of 300 μm throat diameter. The valve is installed in the vacuum chamber and cooled by a GM refrigerator via connection with copper plate and shafts. The temperature of copper valve jacket is measured by a thermocouple. A semiconductor laser of NEOARK LDP2-6535A with 650 nm standard wavelength and 35 mW power is guided in the chamber to perpendicularly intersect the gas flow. A beam dump is set at the opposite side of the laser inlet and the Laval nozzle is rolled by black tape in such a way that the stray light is lowered. The distance between the nozzle exit and the laser chord is 17 mm. A fast CCD camera of 1280 × 1024 pixels is arranged in the direction perpendicular to both the gas flow (*x*-direction) and the laser beam (*y*-direction). A typical CCD image of 8.0 MPa H_2 cluster jet at 125 K and the cross section of the Laval nozzle are shown in Fig. 2.22. A straight emission line that is scattered by clusters is observed along the laser beam.

2.3.3 Temperature dependence of scattering signal

The scattering signals are detected when the temperature is below ~180 K as expected from the calculation. The image of scattering signal emission line of H_2 at 178 K is shown in Fig. 2.23. The empirical scaling parameter Γ*of H_2 at ~180 K nearly corresponds to that of N_2 at the room temperature. Figure 2.24 shows scattering signal profiles along the laser light direction (*y*), where the temperature is varied from 119 K to 143 K. The exposure time of the CCD camera is fixed to 10 ms and the backing pressure is fixed to 5 MPa for this scan. The width of 5.8 mm in Fig. 2.24 denotes the exit hole diameter of the Laval nozzle. These profiles are axisymmetric. The full-width of half-maximum (FWHM) is 6.2 ± 0.2 mm. The FWHM does not depend on temperature. Two peaks observed in the profiles indicate that the center of cluster flow has hole. Similar hollow profile was observed in the study on plasma produced by laser pulses irradiating a cluster target generated by a Laval nozzle [14]. The points on three

y-coordinate (*y* = 2.9 for □, 0.7 for ○, 0 mm for Δ) of the scattering profile are plotted in Fig. 2.25. The signal points of *y* = 2.9 mm is the radial of nozzle exit hole diameter (5.8 mm). The signal points of *y* = 0.7 mm indicate the peak signals in the profiles. The signal points of *y* = 0 mm show the center of hollow profiles. The points on three *y*-coordinate of scattering signal increase with $\sim T_0^{-5}$. This result is similar to the results in Ref. [8].

2.3.4 Pressure dependence of scattering signal

Figure 2.26 shows scattering signal profiles along the laser light direction (*y*), where the backing pressure is increased from 3.0 to 8.0 MPa at ~125 K. The FWHM of these profiles is 5.83 ± 0.3 mm and roughly corresponds to the exit hole diameter of the Laval nozzle. The points on three *y*-coordinate (*y* = 2.9 for □, 0.7 for ○, 0 mm for Δ) scattering profiles in Fig. 2.26 as a function of the backing pressure are plotted in Fig. 2.27. The peak scattering signal (*y* = 0.7 mm) increases with $\sim P_0^3$. The result is similar to the expectation of Eq. (2.31) and the results in Ref. [8, 13]. Farges *et al*. estimated this relation assuming a multilayer model for Ar cluster. This suggests that the structure of hydrogen cluster also has the multilayer model for Ar cluster. The other signal points of *y* = 2.9 and 0 mm are smaller than the cubic dependence on the backing pressure.

Figure 2.28 shows the images of cluster scattering signals in the case of H_2 at ~130 K without the Laval nozzle (a) and with the Laval nozzle (b). The divergence of cluster jet has been decreased after installation of the Laval nozzle.

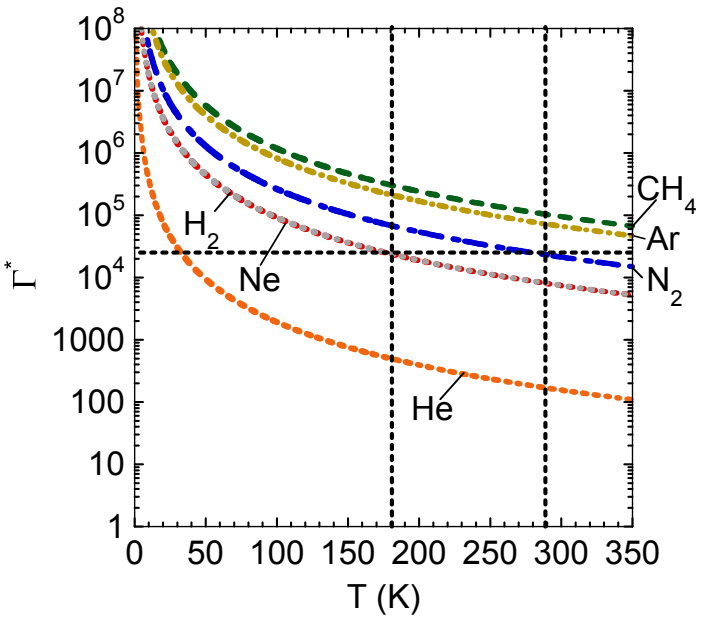

Fig. 2.20 Calculated results of the scaling parameter Γ*, where d = 300 μm, α = 12°, P_0 = 4 MPa. The parameter of hydrogen at the temperature region of ~180K corresponds to that of nitrogen at the room temperature.

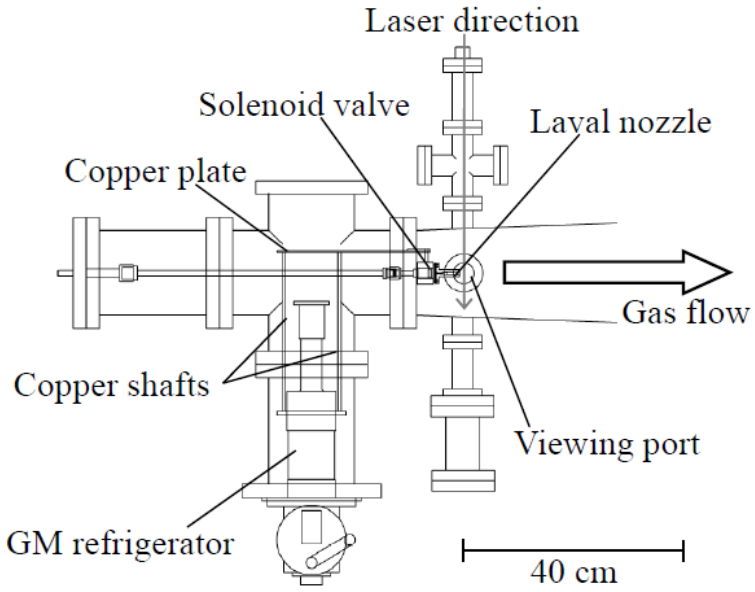

Fig. 2.21 Schematic of the experimental setup. A solenoid valve installed in the vacuum chamber is cooled by the GM refrigerator through copper plates.

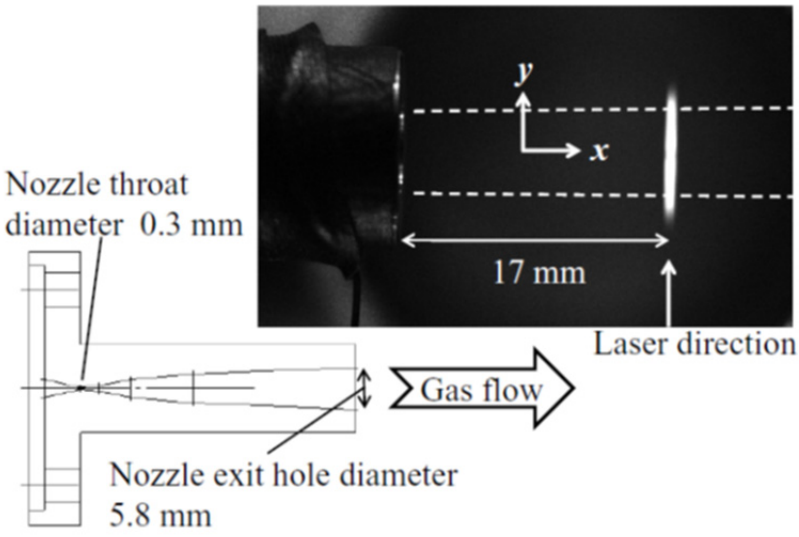

Fig. 2.22 Typical CCD image in the case of H_2 at 125 K and the cross section of the Laval nozzle. The backing pressure is 8.0 MPa, and the exposure time is 10 ms. The laser beam direction (y) is perpendicular to the gas flow (x). The broken lines denote extension of the exit hole with a diameter of Laval nozzle (5.8 mm).

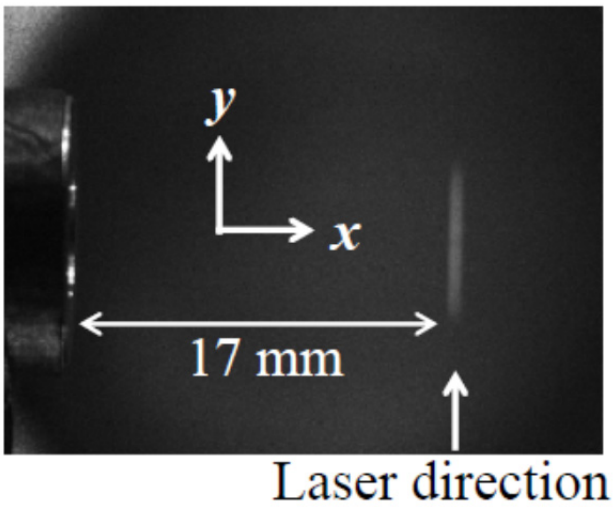

Fig. 2.23 The image of scattering signal emission line in the case of H_2 at 178K. The backing pressure is 5.0 MPa, and the exposure time is 10 ms.

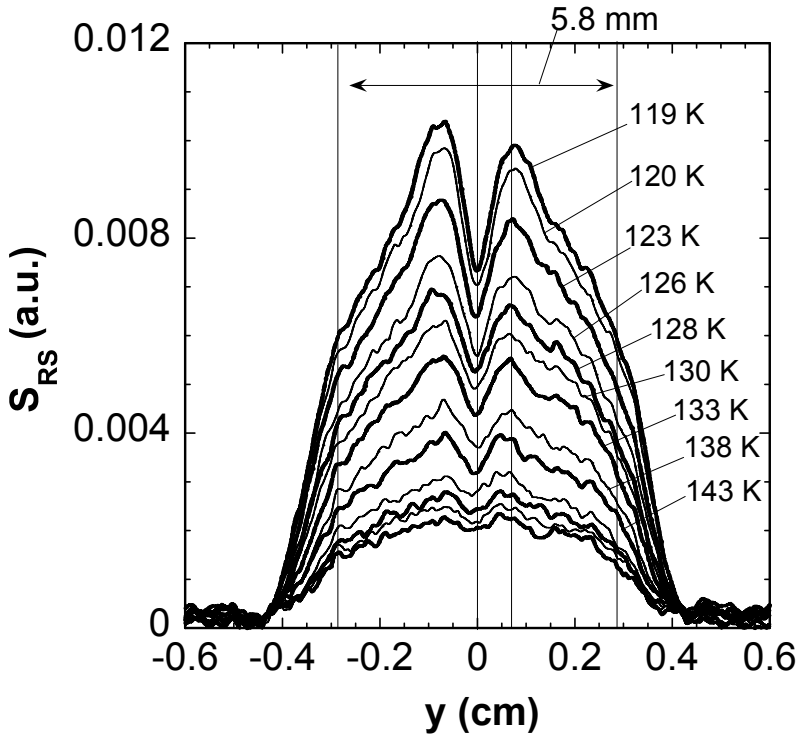

Fig. 2.24 Scatter signal profiles normalized by the exposure time (μs), where the temperature is varied from 119K to 143K.

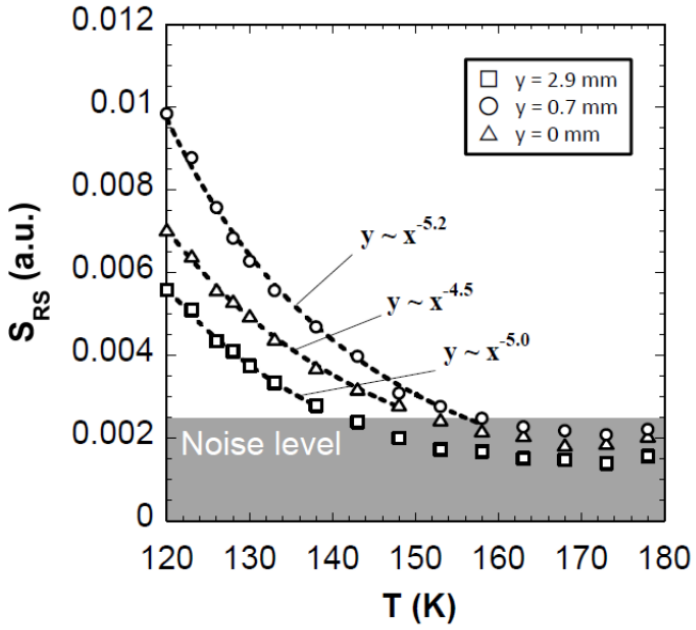

Fig. 2.25 The points on three y-coordinate (y = 2.9 for □, 0.7 for ○, 0 mm for △) of the scattering profiles in Fig.2.24 are plotted.

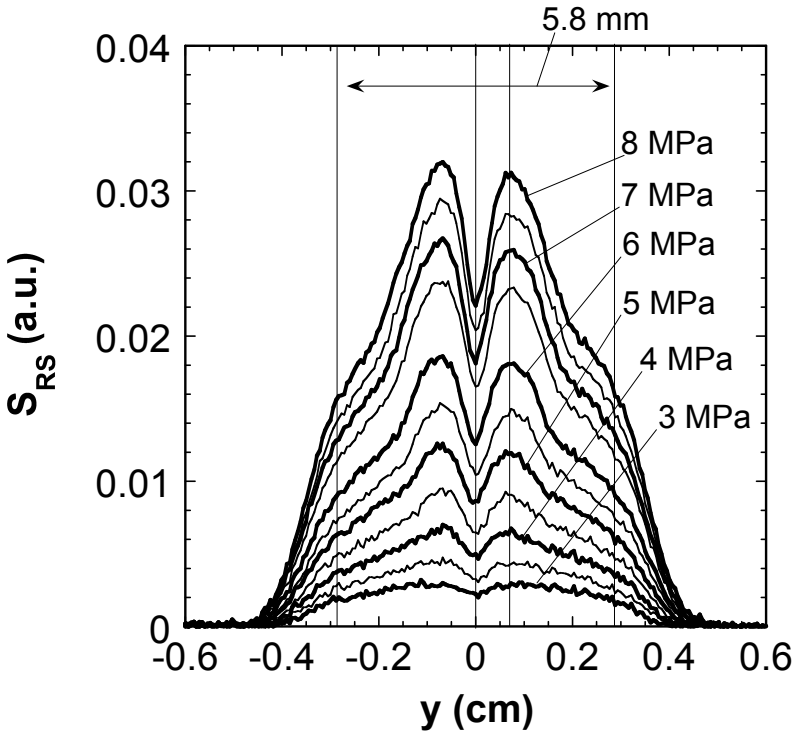

Fig. 2.26 Scatter signal profiles normalized by the exposure time (μs), where the backing pressure is varied from 3.0 MPa to 8.0 MPa.

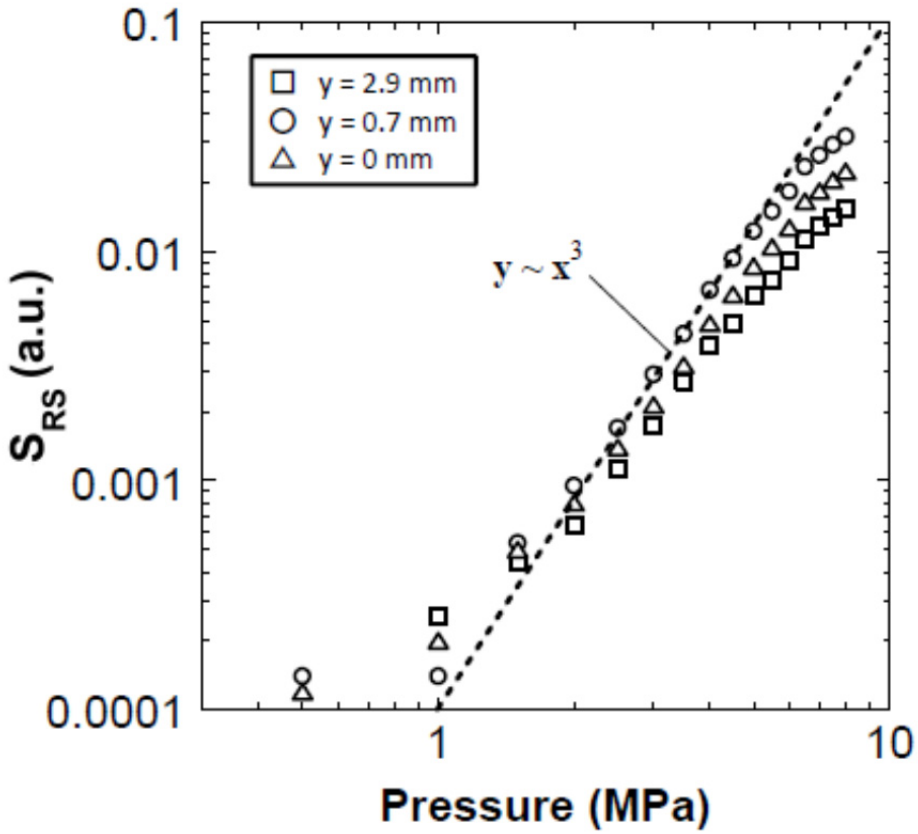

Fig. 2.27 The points on three y-coordinate (y = 2.9 for □, 0.7 for ○, 0 mm for △) of the scattering profiles in Fig.2.26 are plotted.

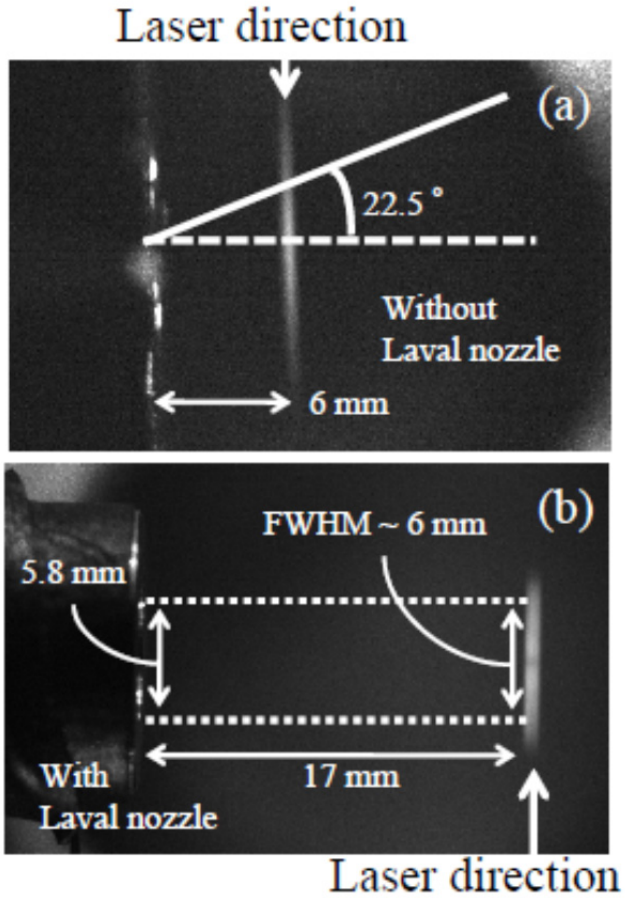

Fig. 2.28 The images of cluster scattering signals in the case of H_2 at ~130 K without the Laval nozzle (a) and with Laval nozzle (b). The backing pressure is 5.0 MPa, and the exposure time is 10 ms.

2.4 Shadow graph imaging and emission imaging using electron beam

2.4.1 Shadow graph imaging

A shadow graph imaging is also available for investigation of effect of the Laval nozzle. In the case of nitrogen at ~115 K, rapid increase of the signal intensity was observed at the backing pressure, P_0 > 4 MPa (Fig. 2.29). In the case of methane at the backing pressure of 4MPa, the scattering signal increased rapidly under the temperature of ~170 K (Fig. 2.30). Similar phenomena have also been observed in the cases of argon and similar results are also shown in Ref. [8]. This might presumably be due to the phase transition to the liquid state. In this regime, the particle flow is visible by eye and it is possible to take the image of shadow graph by the CCD camera. Figure 2.31(a) shows a shadow graph imaging of the particle flow in the case of CH_4 at 138 K with the Laval nozzle. The scattering signals of this region are much stronger than that of clusters. The imaging of strong scattering signal is shown in Fig.2.31 (b) at the same conditions in Fig. 2.31(a). Figure 2.32 shows the images of cluster scattering signals in the case of H_2 at ~130 K with the Laval nozzle (a) and a shadow graph image of the particle flow in the case of CH_4 at 180 K with the Laval nozzle (b). Figs. 2.32 (a) and (b) imply that the width of clusters during 17 mm is similar to the exit hole diameter and the width of the liquid particle flow is slightly broader than that of clusters. The expansion angle of ~5º is estimated from this shadow imaging.

2.4.2 Emission imaging using electron beam

Emission imaging using electron beam is also available for visualization of gas flow. Figure 2.33 shows the schematic of emission imaging using electron beam. A Pierce type electron gun is guided in the chamber to perpendicularly intersect the gas flow.

The emission from nuclear excitation and/or de-excitation process is detected by CCD camera. Figure 2.34 shows a typical emission imaging in the case of helium gas flow with the Laval nozzle and the backing pressure of 4.0 MPa. The expansion angle of this gas flow is estimated to be 5^{o} by this imeaging.

In conclusion, the divergence of cluster jet has been decreased from 22.5^{o} to ~ 5^{o} after installation of the Laval nozzle. The effectiveness of the Laval nozzle is revealed in this section.

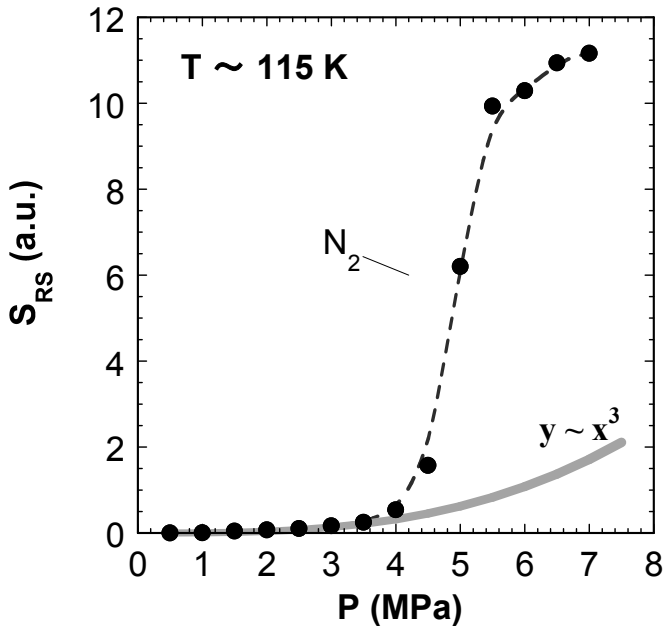

Fig. 2.29 Rayleigh scattering signal as a function of the backing pressure in the case of N_2. A rapid increase of the signal intensity was observed at > 4 MPa.

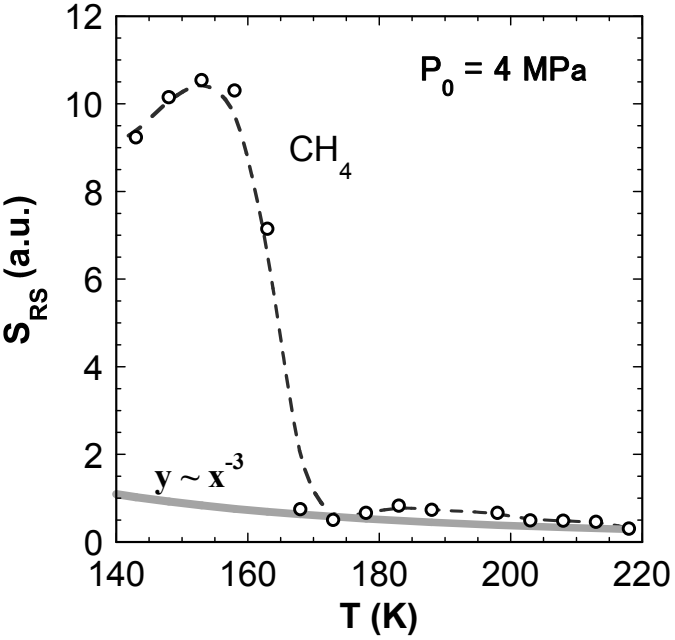

Fig. 2.30 Rayleigh scattering signal as a function of the backing pressure in the case of CH_4. The scattering signal increased rapidly under the temperature of ~170 K.

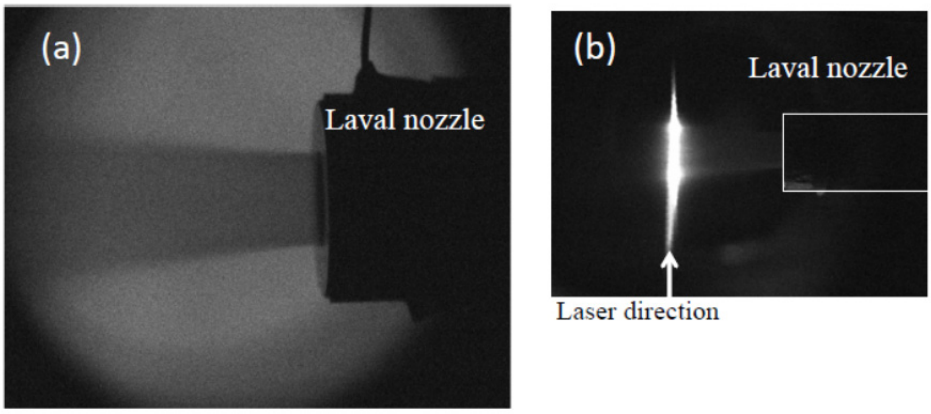

Fig. 2.31 Shadow graph imaging of the particle flow in the case of CH_4 at 138 K with the Laval nozzle (a) and the imaging of too strong scattering signal in the case of (a). The backing pressure is 4.0 MPa, and the exposure time is 1 ms.

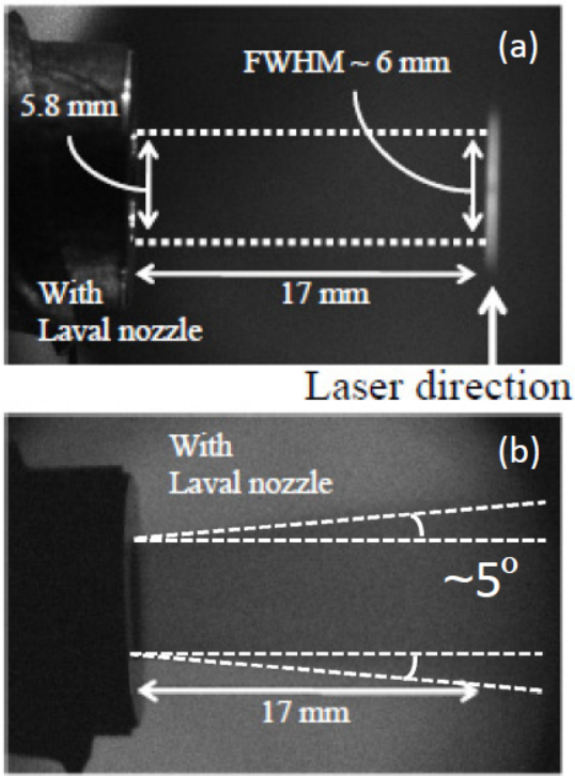

Fig. 2.32 The images of cluster scattering signals in the case of H_2 at ~130 K with Laval nozzle (a). The backing pressure is 5.0 MPa, and the exposure time is 10 ms. A shadow graph image of the particle flow in the case of CH_4 at 180 K with the Laval nozzle (b). The backing pressure is 7.0 MPa, and the exposure time is 1 ms.

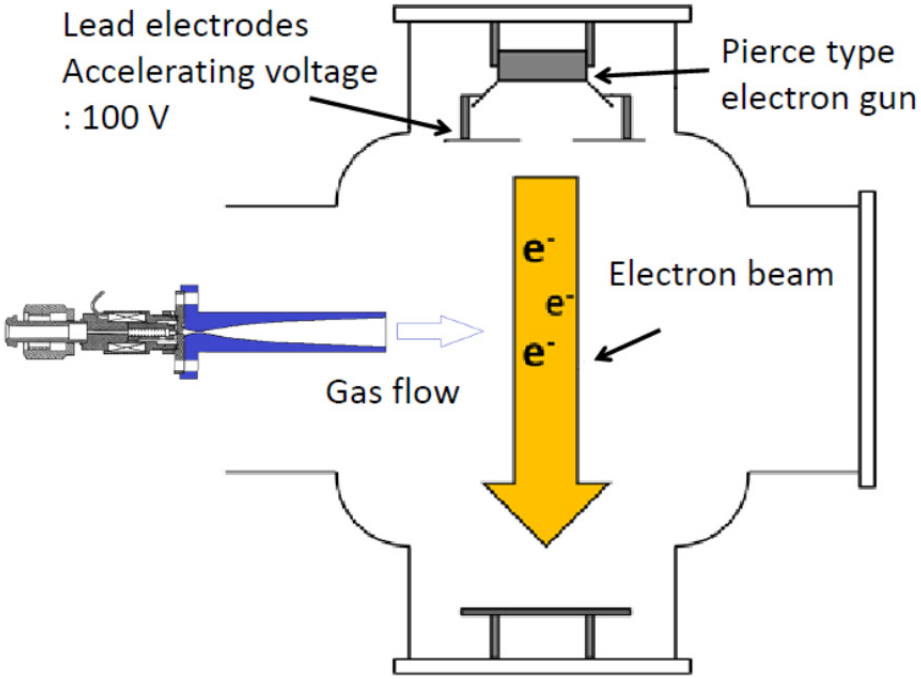

Fig. 2.33 Schematic of emission imaging using electron beam.

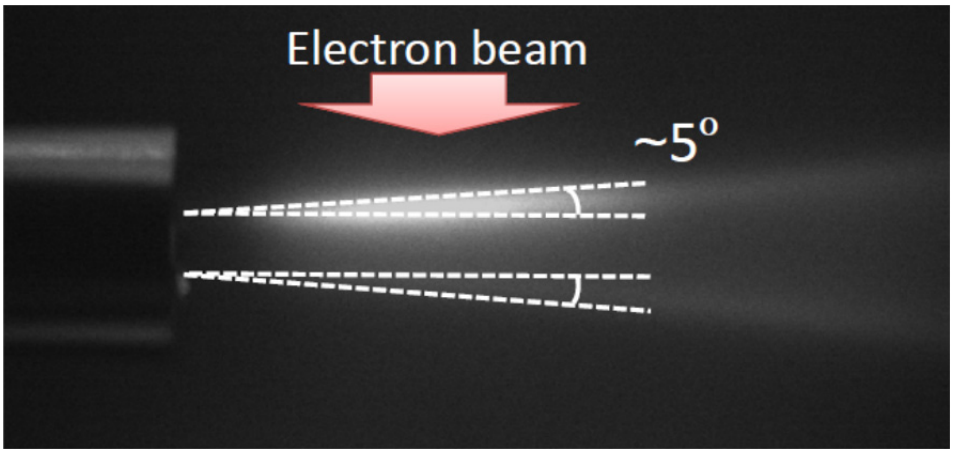

Fig. 2.34 Emission imaging using electron beam. The gas species is helium and the baking pressure is 4.0 MPa.

2.5 Installation of SSGP device in LHD

The prototype of SSGP device was installed in the LHD at 2008 experimental campaign. It has been improved year by year. The SSGP device is installed on a lower port in LHD (See Fig.2.35). The direction of the gas flow is upward. The distance from the valves to the plasma is ~4 m. In the experimental campaign 2008, the SSGP device is equipped with one solenoid valve without Laval nozzle. In the experimental campaign 2009, a Laval nozzle was firstly examined. The parameters of the Laval nozzle were the throat diameter of 0.3 mm, the design Mach number of 8, and the angle of the inflection point of 12º. In the experimental campaign 2010, three solenoid valves with three different Laval nozzles were installed. Three solenoid valves were equipped with three different Laval nozzles of 0.1, 0.3 and 0.6 mm throat diameter, which we refer to ϕ0.1, ϕ0.3, and ϕ0.6, respectively. These Laval nozzles were similarly designed to generate a gas flow of M_1 = 8. In the experimental campaign 2011, the ϕ0.1 Laval nozzle was replaced by a new type Laval nozzle called ϕ0.6L. The ϕ0.3 and ϕ0.6 Laval nozzles are similarly designed to generate the gas flow of Mach number M_1 = 8 with the angle of inflection point θ_1 of 12º. Since the flow rate of the ϕ0.1 Laval nozzle was small compared with the LHD plasma volume and the fueling characteristic was similar to that of conventional GP, it has been replaced with an improved ϕ0.6L Laval nozzle. The ϕ0.6L Laval nozzle is designed to generate the gas flow of M = 11.5 with θ_1 = 4º. The length of ϕ0.6L Laval nozzle is 40 cm and 4 times longer than that of the ordinary ϕ0.6 Laval nozzle. It is expected that the gas flow through the ϕ0.6L Laval nozzle will become more convergent and faster than those of the ordinary ϕ0.6 Laval nozzle. Figure 2.36 shows the image of four Laval nozzles and summary of transition of SSGP device. Figure 2.37 shows the diagram of SSGP control system. There are two control signal lines in SSGP system. One is normal SSGP control system that the waveform is input by control PC in control room, the other is the system for high frequency SSGP, that the waveform is input by a pulse generator in the LHD room.

It is favorable for high frequency signals to be input in short line. The SSGP system diagram is shown in Fig. 2.38. There are three gas bombs for SSGP. The species of these bombs are hydrogen, helium and others, respectively. In general, argon bomb is located in the position of others bomb. Pneumatic valves are equipped on gas line tube and commanded remotely. Since the solenoid valve is driven by the electrical magnetic force to open a poppet, it is necessary that the solenoid valves are shielded magnetically in order to prevent a mechanical error. Detailed of the magnetic shield is described in Appendix.

Although SSGP device was developed as supersonic cluster beam (SSCB) injection, it was selected SSGP not SSCB by the following reasons.

Differences between SSGP and SSCB are shown as follows,

1. The convergence of gas flow is similar to the convergence of cluster beam.
2. The density of the cluster beam is higher than that of gas flow
3. The controllability of cluster beam is more difficult than that of SSGP.

Especially, it is necessary to cool the solenoid valves to less than 180 K for SSCB injection. Since a seat leak rate of cooled valves is large, SSCB needs to be controlled with great caution. Therefore, SSGP was selected in this fueling study.

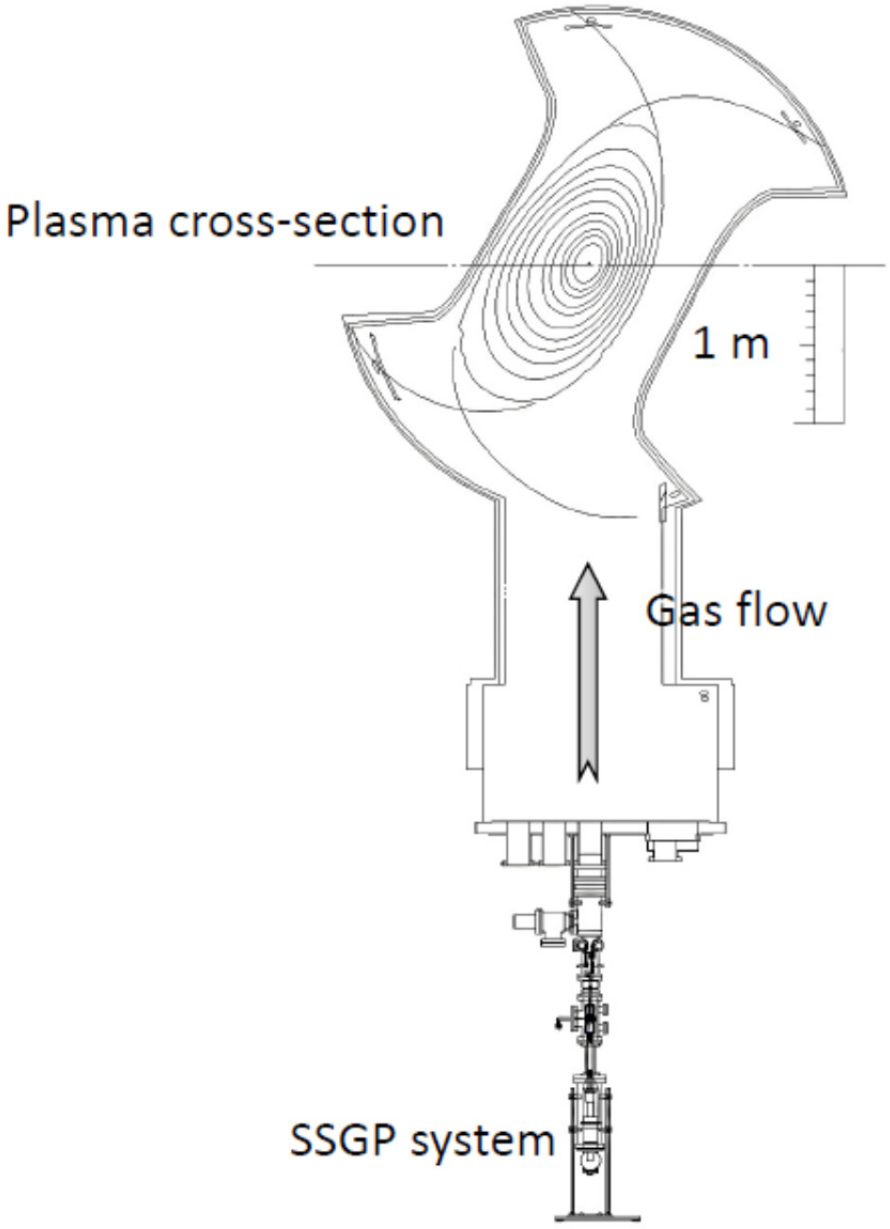

Fig. 2.35 Schematic view of the SSGP device in LHD. The distance from the valves to the plasma is ~4 m. Three types of Laval nozzles are attached to the solenoid valves.

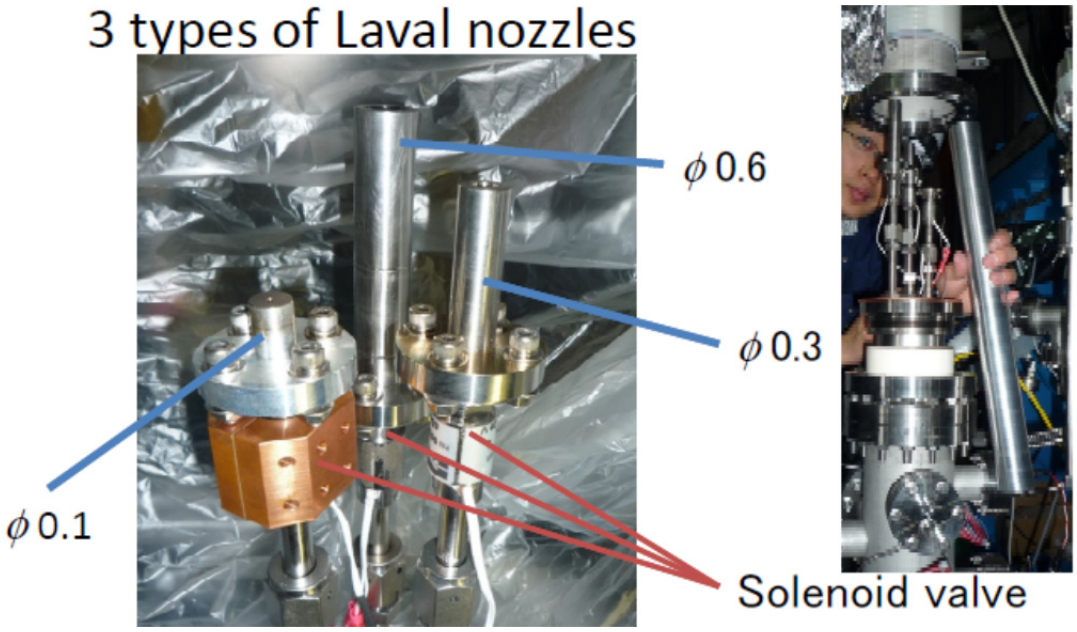

Figure 2.36 Transition of SSGP device
2008: 1 solenoid valve w/o Laval nozzle
2009: 1 solenoid valve w/ Laval nozzle
2010: 3 solenoid valves w/ 3 Laval nozzles
(ϕ0.1, ϕ0.3, ϕ0.6)
2011: 3 solenoid valves w/ 3 Laval nozzles
(ϕ0.3, ϕ0.6, ϕ0.6L)

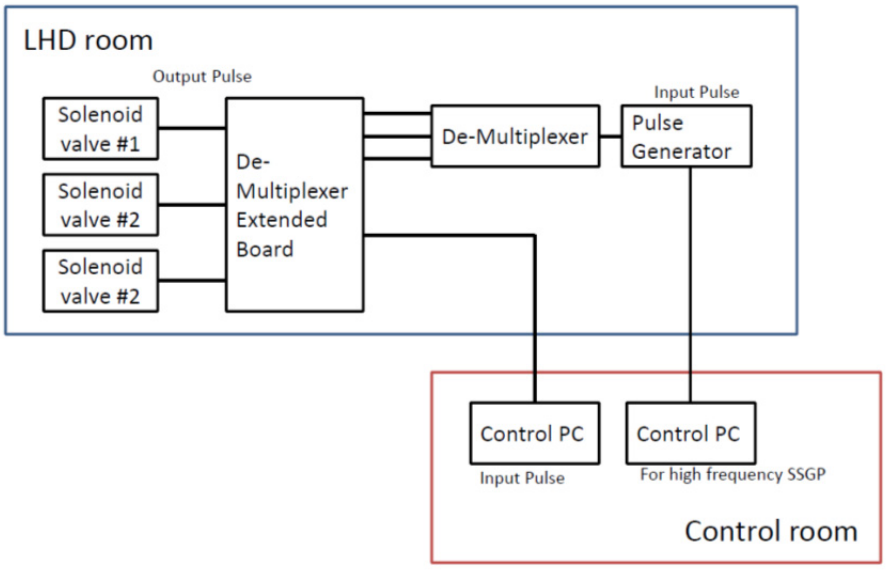

Figure 2.37 SSGP control system.

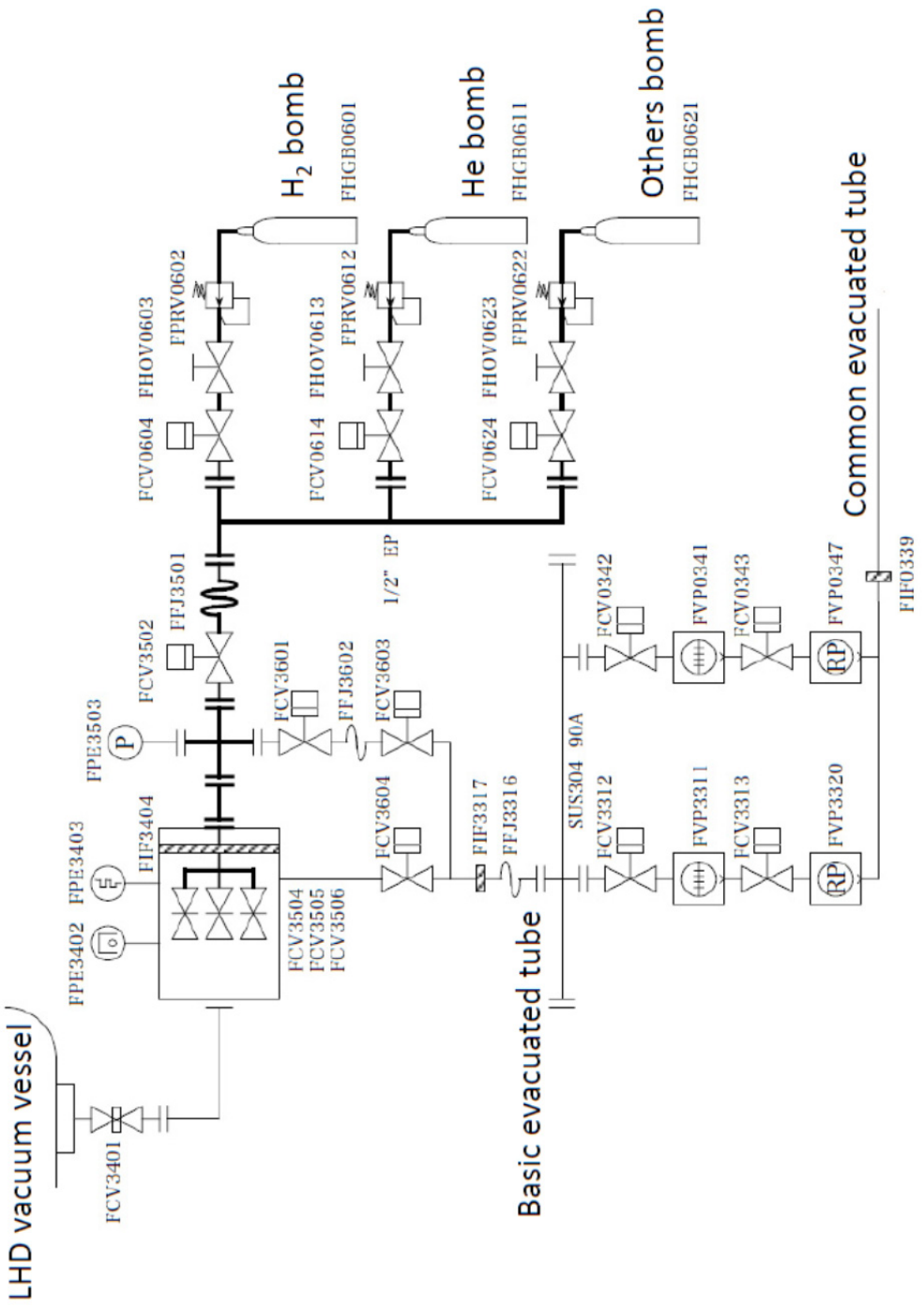

Figure 2.38 SSGP system diagram.

2.6 Summary

Before applying SSGP to LHD, the effectiveness of the Laval nozzle has been tested by visualizing the gas flow. Three methods have been applied for visualization, i.e., the shadow graph imaging, the emission imaging using electron beam, and the laser scattering after forming the cluster beam. The cluster beam is formed by selecting the gas species, or by cooling the gas using a refrigerator.

As the first step, the cluster beam ejected through the fast solenoid valve without using the Laval nozzle has been investigated by selecting the gas species capable of forming the cluster at a room temperature in a test chamber. Time-resolved 2-D images of Rayleigh scattering from clusters have been measured by the fast CCD camera. The expansion half angle of the gas flow without the Laval nozzle was 22.5º. The scattering signal was proportional to the averaged cluster size and the number density of clusters. The scattering signals from argon and nitrogen clusters showed approximately cubic dependence on the backing pressure as expected from a model. Meanwhile, a stronger pressure dependence than this was found in the case of methane, where the scattering signal increased with the fifth power of the backing pressure at 3.2 MPa – 7 MPa, and it was further enhanced at > 7 MPa. This suggests that a new structure model would be necessary to determine the cluster size of methane, which shows stronger backing pressure dependence than argon and nitrogen.

Next, formation of the hydrogen cluster beam using the Laval nozzle has been investigated at a low-temperature regime ranging from 120 K to 300 K. The Rayleigh scattering signal from hydrogen clusters was detected when the temperature was lower than 178 K, as expected from a calculation result of the cluster formation condition. The scattering signal intensity was inversely proportional to the fifth power of the gas temperature and the cube of the backing pressure as expected from an available cluster model. The divergence of cluster beam has been decreased from 22.5 º to ~5 º after installation of the Laval nozzle.

Bibliography of Chapter 2

[1] J. D. Anderson "Modern Compressible Flow with historical perspective" Chapter 5, p.195, The McGraw-Hill Companies, (2004).

[2] J. D. Anderson "Modern Compressible Flow with historical perspective" Chapter 3, p.80, The McGraw-Hill Companies, (2004).

[3] NACA Technical Note No.1651 (1948).

[4] E.W. Becker, K. Bier, and W. Henkes, Zeitschrift für Physik, Bd. 146, S333 (1956).

[5] B. J. C. Burrows *et al*., Paper **51**, Fifth Symposium on Fusion Technology (1968).

[6] L. Yao et al., Nucl. Fusion **47**, 1399 (2007).

[7] V.A.Soukhanovskii *et al*. Rev Sci Instrum.**75**, 4320 (2004).

[8] R. A. Smith *et al* Rev. Sci. Instrum. **69**, 3798 (1988).

[9] O. F. Hagena Z. Phys. D **4**, 291 (1987).

[10] J. Miyazawa et al., Nucl. Fusion **46**, 532 (2006).

[11] O. F. Hagena and W. Obert, J. Chem. Phys. **56**,1793 (1972).

[12] J. Farges, M. F. de Feraudy, B. Raoult, and G. Torchet, J. Chem. Phys. **84**, 3491 (1986).

[13] A. Murakami *et al*., Plasma Fusion Res. **5**, S1032 (2010).

[14] I. Yu. Skobelev *et al*., JETP **94**, 966 (2002).

Chapter 3

Fueling Characteristics of Supersonic Gas Puffing

3.1 Introduction

Supersonic gas puffing (SSGP), where high-pressure hydrogen gas is ejected through a fast solenoid valve equipped with a Laval nozzle, has been applied to large high-temperature plasmas and its fueling characteristics have been investigated in the Large Helical Device (LHD) [1,2]. The heliotron configuration is characterized by an ergodic layer surrounding the last-closed-flux-surface (LCFS). The role of the ergodic layer on fueling has, however, not been understood sufficiently yet. The plasma density can be increased to the density limit by GP in LHD [3], without suffering severe shielding of fuel particles as observed in tokamaks [4]. Since there is no disruption in LHD, the edge density can be significantly increased by supplying particles with a large flow rate. The plasma minor radius of ~0.6 m is much longer than the penetration depth of neutrals supplied by SSGP, of which the typical order is mm in LHD.

The solenoid valves used in the SSGP device are characterized by the response

time of less than 1 ms and the higher working pressure of < 8 MPa than those of piezo-electric valves used in the ordinary GP device in LHD [5,6]. Three solenoid valves are equipped with three different Laval nozzles of 0.1, 0.3 and 0.6 mm throat diameter, which we refer to ϕ0.1, ϕ0.3, and ϕ0.6, respectively. These Laval nozzles are similarly designed to generate a gas flow of $M_t = 8$, where M_t is the Mach number of the design value. According to the experimental results obtained in a test stand [1,2], the divergence of supersonic gas flow has been controlled to ~10º by these Laval nozzles, even though the measured hydrogen gas flow speed was ~1 km/s, which roughly corresponds to the hydrogen sound speed at room temperature. By selecting nozzles and backing pressure, one can adjust the flow rate of SSGP from ~1 to ~800 Pa·m^3/s. The measured hydrogen flow rates of the three Laval nozzles are summarized in Table 3.1. When the backing pressure is 5.0 MPa, at which the SSGP device was operated in the series of experiments discussed in the next section, the particle flux, Γ_{SSGP}, of the Laval nozzles of ϕ0.1, ϕ0.3, and ϕ0.6, are ~1.4, ~9.3 and ~22.3 × 10^{22} particles/s, respectively.

In this chapter, the fueling characteristics of SSGP applied to large high-temperature helical plasmas heated by neutral beam (NB) injection are discussed based on the analysis of electron density profile data. Typical responses of the plasma to SSGP are given in Section 3.2. The fueling efficiency is discussed in Sections 3.3. Improved Laval nozzle is introduced in section 3.4. The results of improved Laval nozzle is reported in section 3.5. Finally, these are summarized in Section 3.6.

Table. 3.1 The hydrogem flow rate of SSGP

	Laval nozzle diameter		
Backing pressure	ϕ0.1 mm	ϕ0.3 mm	ϕ0.6 mm
1.0 MPa	~6 Pa·m^3/s	~41 Pa·m^3/s	~98 Pa·m^3/s
5.0 MPa	~28 Pa·m^3/s	~190 Pa·m^3/s	~454 Pa·m^3/s

3.2 Typical responses of the plasma to SSGP

In order to investigate the fueling characteristics of SSGP, density ramp-up experiments have been carried out in LHD. Figure 3.1 shows typical time evolutions of the line-averaged electron density, $\overline{n_e}$, and radial density profiles before and after the fueling by SSGP. In the series of experiments, the magnetic field strength on the magnetic axis, B_t, was fixed to 1.5 T. The major radius, R, and the minor radius, a, of the plasma torus were also fixed to 3.6 m and 0.6 m, respectively. The plasmas were heated by NB injection with various heating powers of P_{NB} = 9 – 13 MW. After SSGP using the Laval nozzles of ϕ0.1, ϕ0.3, and ϕ0.6, at t = 3.765 s, with the pulse length of 200 ms, 50 ms, and 20 ms, respectively, $\overline{n_e}$ was increased by 1×10^{19} m^{-3} (Fig. 3.1(a)), 2.5×10^{19} m^{-3} (Fig. 3.1(c)), and 3.5×10^{19} m^{-3} (Fig. 3.1(e)). Hatched regions in Figs. 3.3(a), 3.3(c), and 3.3(e) denote the SSGP pulse length. It should be noted that the line-averaged density kept increasing even after the turn off of the SSGP. Figures 3.1(b), 3.1(c), and 3.1(f) are the radial profiles of electron density before (t = 3.766 s) and during/after (t = 3.800 s) SSGP, measured by a YAG Thomson scattering system [7, 8]. Figures 3.1(d) and 3.1(f) show that a large increase in the electron density profile is observed at $r_{eff} \sim 0.65$ m, where r_{eff} is the averaged minor radius. In figures 3.1(b), 3.1(d), and 3.1(f), the position of $a_{99} \sim 0.64$ m is denoted by a vertical line, where a_{99} is the effective minor radius in which 99% of the plasma kinetic energy is confined. In these discharges, a_{99} roughly corresponds to the position of LCFS ($r_{eff} \sim 0.63$ m in vacuum). Especially in the case of the ϕ0.6 Laval nozzle, a strongly hollow density profile with steep inward gradient was formed after SSGP, as shown in Fig. 3.1(f). A rapid increase in $\overline{n_e}$ observed in the cases of ϕ0.3 and ϕ0.6 Laval nozzles after SSGP was due to this edge density increase. After the SSGP pulse, the hollow density profile gradually becomes flat by diffusion. This is why $\overline{n_e}$ continues increasing after SSGP. This point is important for discussing the fueling efficiency of SSGP and will be

discussed again in the next section. According to these observations, SSGP deposits the particles in the plasma edge region of $r_{\mathrm{eff}} > 0.64$ m, which corresponds to the ergodic layer outside the LCFS, independent of the type of Laval nozzle.

3.3 Fueling efficiency of SSGP

3.3.1 Differentiated fueling efficiency

As the first step, the fueling efficiency of SSGP has been estimated by comparing the time derivative of the total electron inventory, N_{e}, and the particle flux, Γ_{SSGP}. In this study, N_{e} is estimated from the volume-integration of the electron density profile as shown below;

$$N_{\mathrm{e}} = \int_0^{a_{99}} n_{\mathrm{e}}(r_{\mathrm{eff}}) \frac{\mathrm{d}V_{\mathrm{p}}}{\mathrm{d}r_{\mathrm{eff}}} \mathrm{d}r_{\mathrm{eff}} \quad , \tag{3.1}$$

where V_{p} is the plasma volume. Here, the differential fueling efficiency, η_{diff}, is defined by

$$\eta_{\mathrm{diff}} \equiv \frac{\mathrm{d}N_{\mathrm{e}}/\mathrm{d}t}{\Gamma_{\mathrm{SSGP}}} \times 100 , \tag{3.2}$$

in units of %. Figure 3.2 (a) shows η_{diff} as a function of $\overline{n_e}$ before SSGP, in the case of the ϕ0.3 Laval nozzle operated with various pulse lengths ranging from 40 to 200 ms and backing pressures of 2 MPa and 5 MPa. These data are extracted from a series of experiments carried out at R = 3.6 m, a = 0.6 m, B_0 = 1.5 T, and P_{NB} = 9 – 13 MW. The fueling efficiency decreases as the target plasma density increases. This density dependence of fueling efficiency is similar to the results in Tore supra [9]. Figure 3.4 shows two radial electron density profiles in the cases of high and low fueling efficiency, where SSGP was injected at t = 3.765 s and t = 3.965 s, respectively, with the same pulse length of 50 ms. In the case of high fueling efficiency (Fig. 3.3(a)), electron density before SSGP (t = 3.766 s) is low and the electron density was increased in a wide region of $r_{\mathrm{eff}} > 0.3$ m during SSGP (t = 3.800 s). In contrast, the edge electron

density before SSGP was already high in the case of low fueling efficiency (Fig. 3.3(b)). The electron density increase was limited to the edge region of $r_{eff} > 0.55$ m. If we assume that the electron density rises at $r_{eff} > 0.64$ m were the same for the two cases of high and low efficiency, the inward gradient of the density profile just after SSGP should depend on the edge density at $r_{eff} \sim 0.64$ m, n_{e_edge}, before SSGP. In other words, the inward density gradient in the edge region in the case of low n_{e_edge} becomes steeper than that in the case of high n_{e_edge}. The inward density gradient transports fuel particles from the edge region to the core region through the diffusion process, i.e., the particle flux is proportional to the inward density gradient. Therefore, as long as the particle diffusion coefficient is constant, the steep inward gradient observed in the low n_{e_edge} case (Fig. 3.3(a)) is beneficial for achieving a high fueling efficiency. Figure 3.2(b) shows the fueling efficiency as a function of n_{e_edge} before SSGP. A strong η_{diff} dependence on n_{e_edge} before SSGP is recognized in Fig. 3.2(b), which can be fitted to

$$\eta_{diff} = 18 \times n_{e\_edge}^{-0.9}, \tag{3.3}$$

for the case of the ϕ0.3 Laval nozzle. According to the discussions above, a steep inward density gradient is required to achieve high fueling efficiency. This can be realized when n_{e_edge} before SSGP is low enough, or the amount of density increase by SSGP is much higher than n_{e_edge} before SSGP. In the case of the ϕ0.1 Laval nozzle, for instance, η_{diff} is as small as 5 – 10 %, even at low density, because the edge density increase after SSGP using this nozzle is small (Fig. 3.1(b)).

3.3.2 Total fueling efficiency

Figures 3.1(c) and 3.1(e) show that $\overline{n_e}$ kept increasing after SSGP. In the density increasing phase after SSGP, the core density inside a_{99} (~0.64 m) is increased by the particles diffusing from the ergodic region outside a_{99}. Figure 3.4(a) shows the temporal evolutions of the electron density at different r_{eff} in the same discharge as shown in Figs. 3.3(e) and 3.3(f). The slow increase in the core density at $r_{eff} = 0.13$ m together with the slow decrease in the ergodic density at $r_{eff} = 0.65$ m indicates the diffusion process of

electrons from the ergodic region to the core region. The electron density increase due to this diffusion process after SSGP should be taken into account in evaluating the fueling efficiency of SSGP. Note that the estimate of fueling efficiency using Eq. (3.2) is limited to during SSGP and does not include this diffusion process after SSGP. Here, we define the total fueling efficiency, η_{tot}, by

$$\eta_{tot} = \frac{\Delta N_e}{\Gamma_{SSGP}\Delta t} \times 100, \tag{3.4}$$

where ΔN_e is the increase in the total electron number due to SSGP and Δt is the pulse length of SSGP. This definition is similar to those used in Refs. [9,10]. In Fig. 3.4(b), η_{tot} as a function of n_{e_edge} before SSGP is compared with η_{diff}. As seen in the figure, η_{tot} is ~1.5 times larger than η_{diff}, even though the negative density dependence is unchanged.

3.4 Improved Laval Nozzle

The SSGP device is installed on a lower port in LHD. Three solenoid valves with different Laval nozzles ϕ0.3 and two 0.6 mm throat diameter, which we refer to ϕ0.3, ϕ0.6, and ϕ0.6L, respectively, are employed in the SSGP device. The ϕ0.3 and ϕ0.6 Laval nozzles are similarly designed to generate the gas flow of Mach number M_t = 8 with the angle of inflection point θ_1 of 12º. Figure 3.5 shows the cross sections of ϕ0.6L Laval nozzle and the ordinary ϕ0.6 Laval nozzle. The ϕ0.6L Laval nozzle is designed to generate the gas flow of M_t = 11.5 with θ_1 = 4º. The length of ϕ0.6L Laval nozzle is 40 cm and 4 times longer than that of the ordinary ϕ0.6 Laval nozzle. It is expected that the gas flow through the ϕ0.6L Laval nozzle will become more convergent and faster than those of the ordinary ϕ0.6 Laval nozzle.

Figure 3.6 shows radial profiles of the electron density measured by a YAG Thomson scattering system before and 3 ms after SSGP with (a) ordinary ϕ0.6 Laval nozzle and (b) ϕ0.6L Laval nozzle [7, 8]. Solid curves in Figs. 3.6(a) and 3.6(b) denote the difference of the density profiles before and 3 ms after SSGP, dn_e. In the case of

ϕ0.6L Laval nozzle, the peak of dn_e is ~ 1.5 times larger than that in the case of ordinary ϕ0.6 Laval nozzle.

3.5 Improvement in the Fueling Efficiency

The fueling efficiency improves suddenly when the target plasma is close to the density limit during SSGP.

Figures 3.7(a) and 3.7(b) show the time evolutions of the line-averaged density and the plasma stored energy in the discharges with improved efficiency and ordinary efficiency. In these discharges, R, a, B_t, and P_{NB} were fixed to 3.6 m, 0.6 m, 1.5 T, and 13 MW, respectively. SSGP was injected through ϕ0.6L Laval nozzle at t = 3.730 s with the pulse length of 130 ms and 150 ms. The backing pressure was ~2 MPa and the flow rate was 170 Pa·m^3/s. The line-averaged density in the case of Δt = 150 ms abruptly increased at t ~ 3.9 s while the plasma stored energy decreased. The plasma stored energy increased again at t ~ 4.0 s and became higher than that of Δt = 130 ms at t ~ 4.1 s. As a result of this, the fueling efficiency was improved for two times even though the difference in the number of supplied particles was less than 20 %.

Figure 3.7(c) shows the time evolutions of the position of a_{99} in both cases. In these discharges, the position of the last-closed-flux-surface (LCFS) in vacuum was 0.63 m. The position of a_{99} is close to LCFS when the density increased while the plasma stored energy decreased at t = 3.9 s. Figure 3.8 shows radial profiles of the electron density in the discharges shown in Fig. 3.7. At t = 3.866 s, the density at r_{eff} ~ 0.65 m in both cases is larger than the Sudo density limit [11] of ~9.2×10^{19} m^{-3} in these discharges. On the other hand, the density at t = 3.900 s in the region of r_{eff} > 0.6 m in the case of Δt = 150 ms exceeds the Sudo density limit, while the density decreased to smaller than the Sudo limit in the case of Δt = 130 ms. It has been revealed that the plasma tends to shrink when the edge plasma density increases to the Sudo limit [12]. In the discharge with Δt = 150 ms, the plasma shrink and SSGP deposited the particles inside LCFS. This is why the density increased rapidly. Similar phenomena are

frequently observed when the edge density of the target plasma is close to the density limit. Since SSGP was turned off before the plasma collapse, the position of a_{99} was restored to the ordinary position after $t \sim 4.1$ s. It is important to turn off SSGP when the plasma shrinks to achieve a high fueling efficiency without collapse.

3.5.1 Reheat after SSGP

Improvement of plasma performance after turning off conventional gas puffing ("reheat mode") had been observed in not only small-scale helical devices such as CHS but also LHD [13, 14]. "Reheat" of the plasma stored energy after a short pulse SSGP was also observed using the ϕ0.6L Laval nozzle. Figures 3.9(a) and 3.9(b) show the time evolutions of the line-averaged density and the plasma stored energy in a "super reheat" discharge. In this discharge, R, a, B_t, and P_{NB} were 3.6 m, 0.6 m, 1.0 T, and 14 MW, respectively. SSGP was injected through the ϕ0.6L Laval nozzle at $t = 4.0$ s with a short pulse length of 25 ms and a high backing pressure of ~6 MPa. With this pulse length, the amount of supplied particle is ~ 13.6 Pa·m^3. The plasma shrunk and the density increased largely after the short pulse SSGP as in the discharge discussed in the previous section. The plasma stored energy was once decreased after SSGP and recovered at $t \sim 4.4$ s. This phenomenon is what we call "reheat".

The fueling efficiency in this discharge was ~37%. In the case of ordinary ϕ0.6 Laval nozzle, plasma was not shrunk even though the same amount of particles were supplied. It presumably indicates that the converged gas flow ejected through the ϕ0.6L Laval nozzle is effective for plasma shrinking.

3.5.2 Helium SSGP

In the case of helium SSGP, where the high recycling from the plasma facing materials is expected, inward density gradient was maintained for a longer time than in the case of hydrogen SSGP. Figure 3.10 shows the time evolutions of the electron density at different r_{eff}/a_{99} in the cases of (a) helium and (b) hydrogen SSGP. In these

discharges, R, a, B_t, and P_{NB} were 3.6 m, 0.6 m, 2.75 T, and ~12 MW, respectively. Helium SSGP was injected at 4.05 s with the pulse length of 80 ms, while hydrogen SSGP was injected at 4.06 s with the pulse length of 70 ms. In both cases, ϕ0.6L Laval nozzle was used. The flow rates of helium and hydrogen SSGP was 80 Pa·m^3/s and 300 Pa·m^3/s, respectively. In the case of helium SSGP, the density at r_{eff}/a_{99} ~ 1.04, which is the region outside LCFS, was kept for ~100 ms presumably due to the high recycling after SSGP. On the other hand, the density at r_{eff}/a_{99} ~ 1.04 in the case of hydrogen SSGP decreased immediately after the injection. Since the strongly hollow density profile was maintained, the core density at r_{eff}/a_{99} ~ 0.2 kept increasing for ~400 ms in the case of helium SSGP. As the result, the fueling efficiency of helium SSGP is as high as 50 – 80 %. Similar high fueling efficiency was also observed in ordinary GP using helium gas [5].

3.6 Summary

Fueling characteristics of SSGP have been investigated in LHD. The total fueling efficiency of SSGP is 15 – 25 % when the target plasma edge density is ~1 × 10^{19} m^{-3}, and it decreases to ~10 % as the edge density increases to ~3 × 10^{19} m^{-3}. SSGP deposits the fuel particles in the plasma edge region and forms a hollow density profile. The inward density gradient that drives inward diffusion of fuel particles is larger in the case of a low target plasma density. This is the reason why the fueling efficiency becomes high at low density. SSGP can supply a large number of particles to the edge region within a short time on the order of ms, which results in the better fueling efficiency compared with ordinary gas puffing. Furthermore, this property adds the effect of edge cooling to SSGP that will be beneficial for divertor heat load reduction, *i.e.*, the edge temperature of the plasma fuelled by SSGP is lower than that fuelled by ordinary gas puffing. Two kinds of improvement in the fueling efficiency of SSGP have been observed in LHD. The fueling efficiency improves suddenly when the target plasma is close to the density limit. In the case of hydrogen SSGP, abrupt increase in the density

increase rate was observed when the pulse-length of SSGP was extended. As a result of this, the fueling efficiency was improved two times even though the difference in the number of supplied particles was less than 20%. “Reheat” of the plasma stored energy after short pulse SSGP was observed using ϕ0.6L Laval nozzle. The fueling efficiency in “reheat” discharge is twice higher than that of ordinary results. The fueling efficiency of helium SSGP is also higher than that of hydrogen SSGP since the edge-density is kept high and a strongly hollow density profile is maintained because of the high recycling.

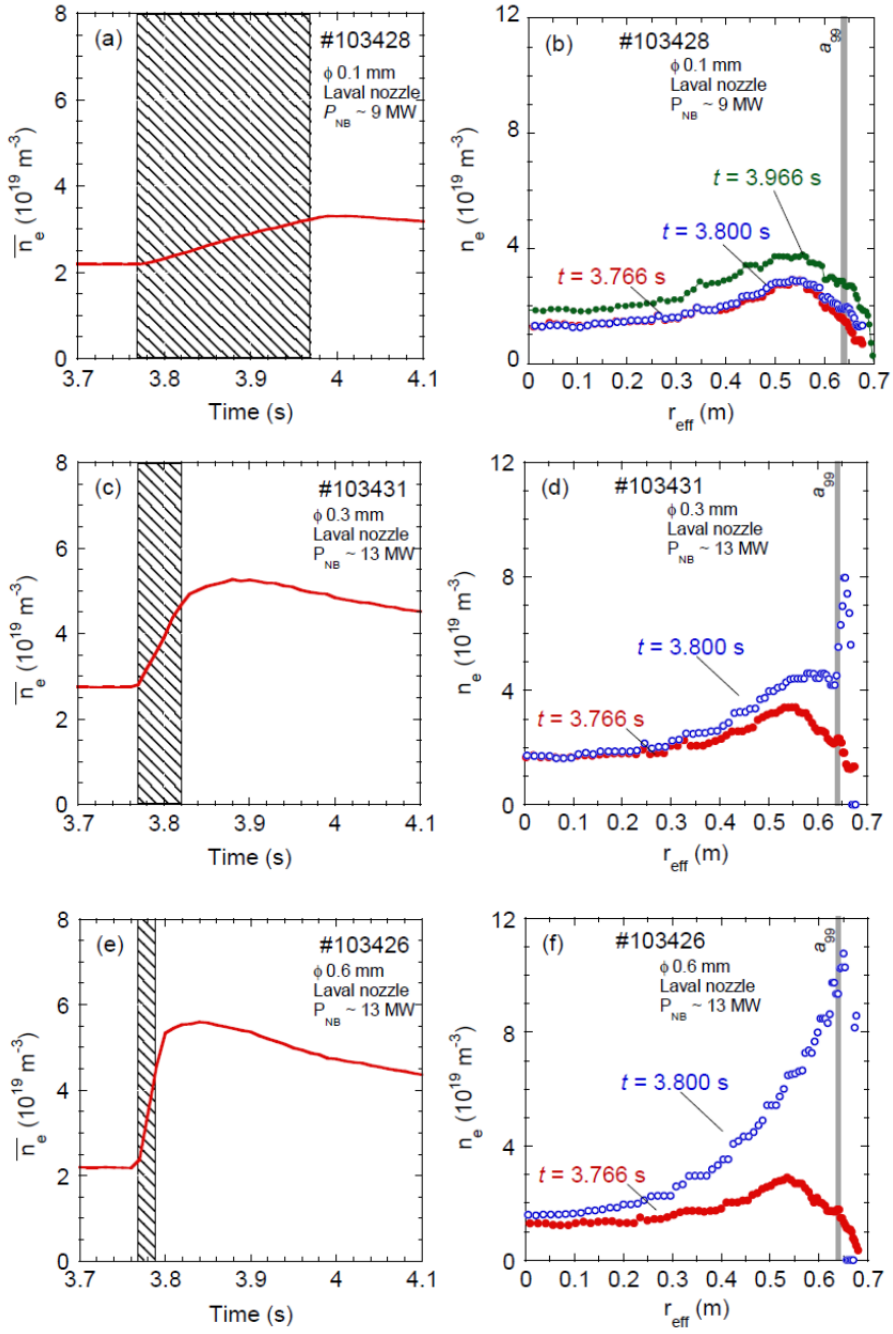

Fig. 3.1 Typical temporal evolutions of the line-averaged electron density, $\overline{n_e}$, and the radial profiles of electron density in the discharges fuelled by SSGP with (a-b) ϕ0.1, (c-d) ϕ0.3, and (e-f) ϕ0.6 Laval nozzles. The hatched region in (a), (c), and (e) denote the SSGP pulse length. Closed and open symbols in (b), (d), and (f) correspond to the density profiles before and after SSGP, respectively.

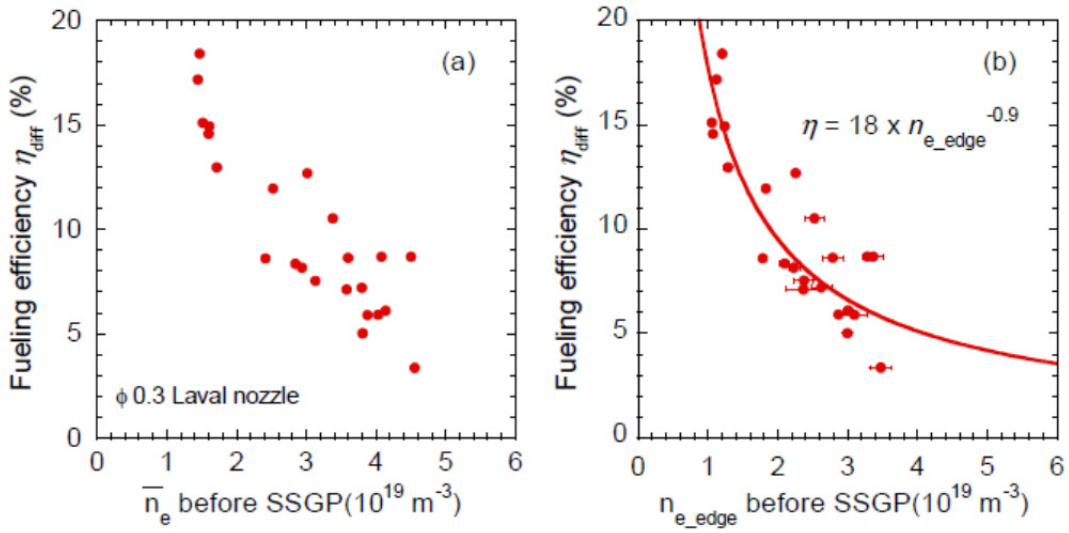

Fig. 3.2 Fueling efficiency in the case of ϕ 0.3 Laval nozzle as a function of (a) the line-averaged electron density before SSGP, and (b) the edge electron density at r_{eff} ~ 0.64 m before SSGP. The fueling efficiency exponentially decreases with the edge electron density before SSGP increases.

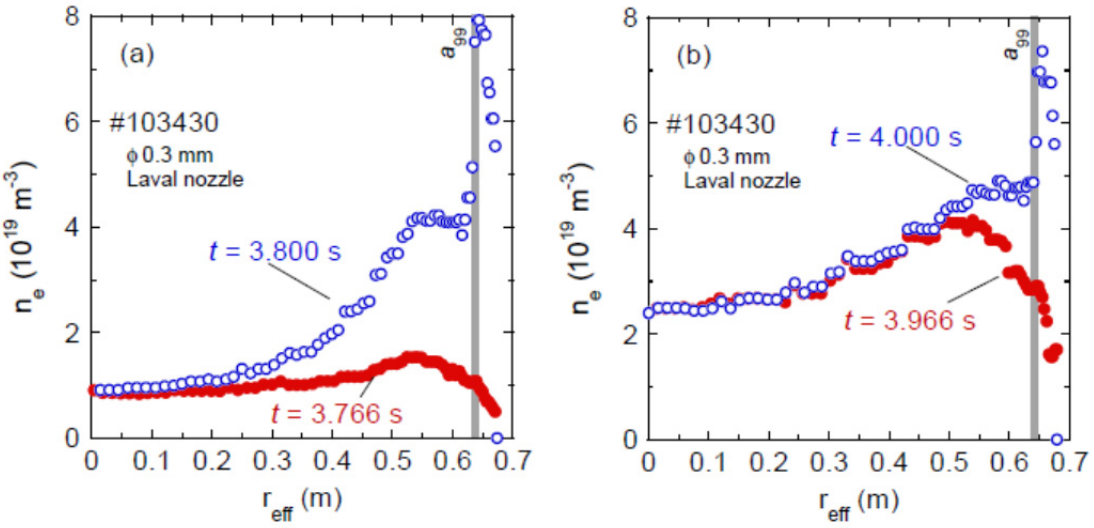

Fig. 3.3 Radial electron density profiles in the cases of (a) high and (b) low fueling efficiency. Closed and open symbols denote before and after SSGP, respectively.

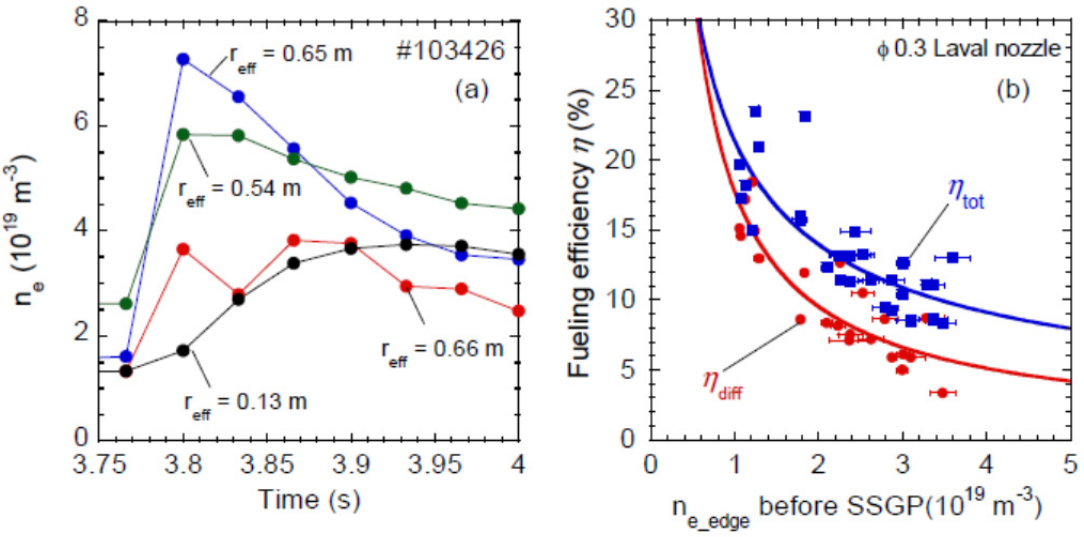

Fig. 3.4 Temporal evolutions of (a) the electron density at different averaged minor radii and (b) the total fueling efficiency as a function of the edge electron density at r_{eff} ~ 0.64 m before SSGP.

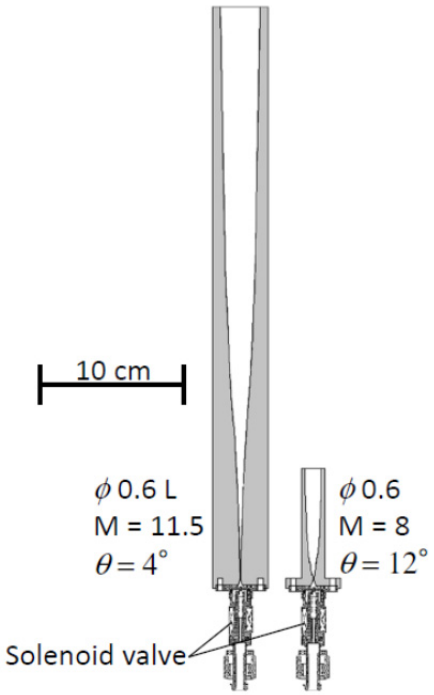

Fig. 3.5 Cross sections of ϕ0.6L and ϕ0.6 Laval nozzle. ϕ0.6L is designed to achieve M_{t} = 11.5 with a steep angle of inflection point of θ_{i}= 4º.

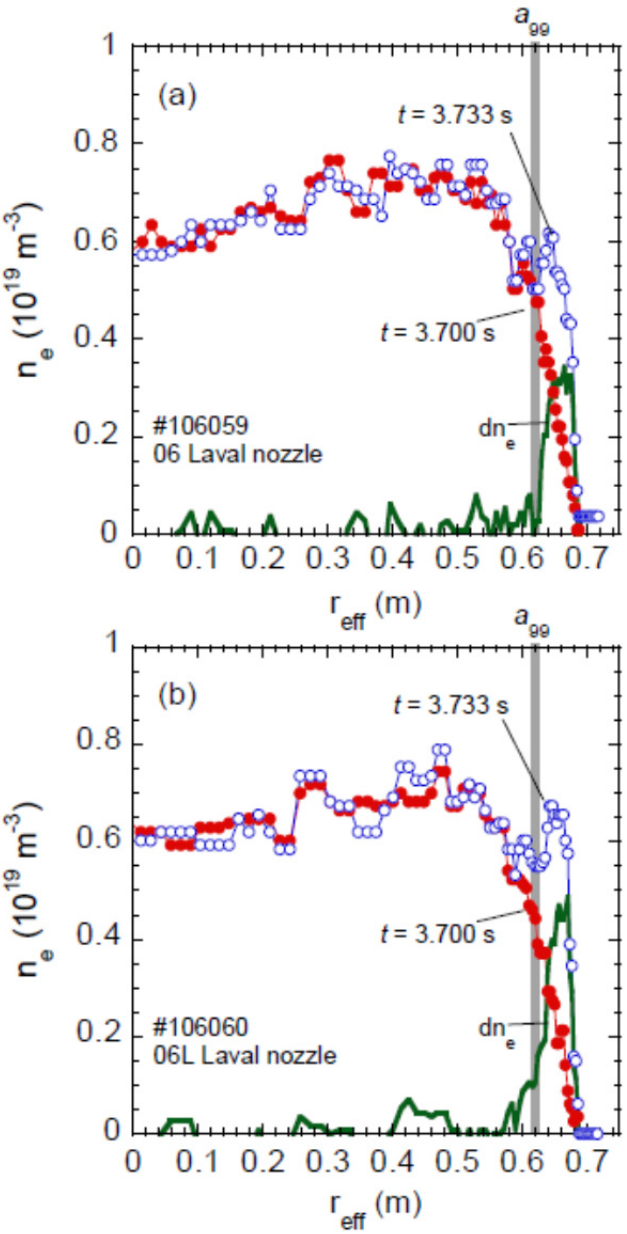

Fig. 3.6 Radial profiles of the electron density before and 3 ms after SSGP with (a) ϕ0.6 Laval nozzle and (b) ϕ0.6L Laval nozzle as a function of the effective minor radius, r_{eff}. Solid curves denote the difference between between before and 3 ms after SSGP and vertical straight lines denote the positions of a_{99}.

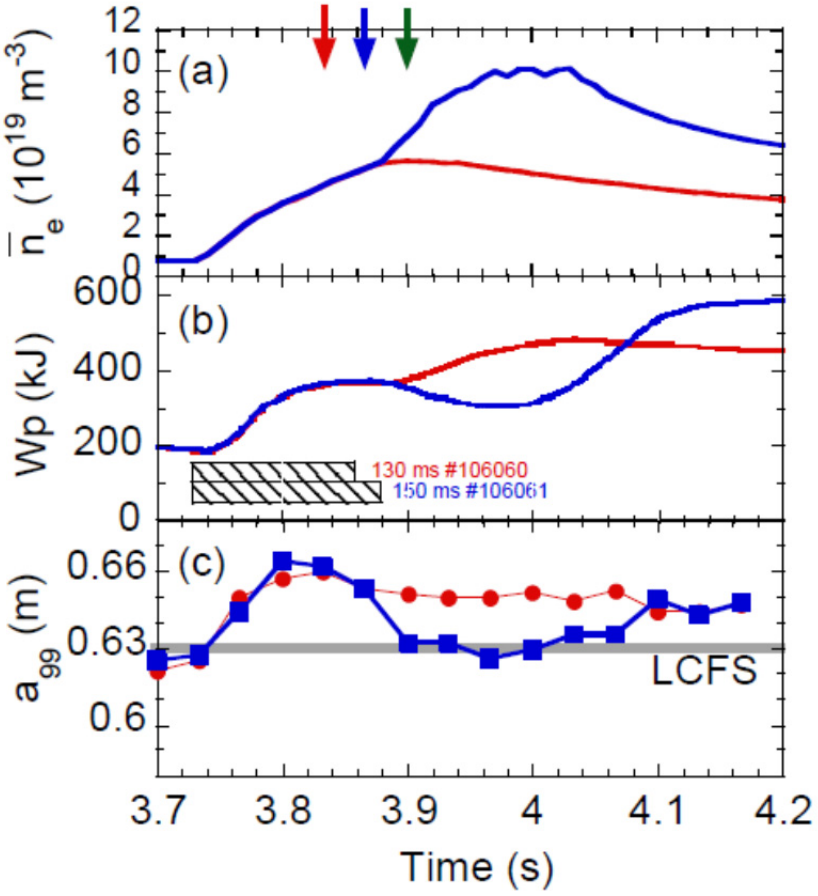

Fig. 3.7 Temporal evolutions of (a) the line-averaged density, (b) the plasma stored energy and (c) a_{99} in the case of the pulse length of 130 ms (red) and 150 ms (blue). a_{99} is close to LCFS at t = 3.9 s in the case of the improved fueling efficiency. Three arrows denote the time slices in Figs. 3.10 (a) and (b).

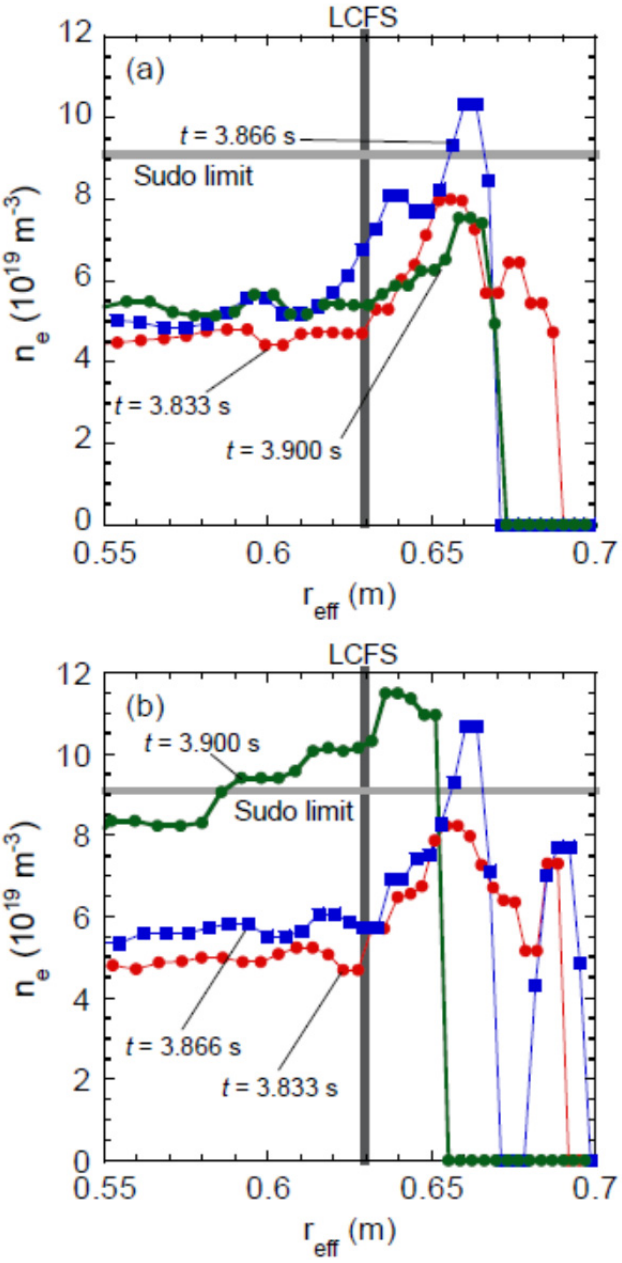

Fig. 3.8 Radial profiles of the electron density in the case of the pulse length of (a) 130 ms and (b) 150 ms.

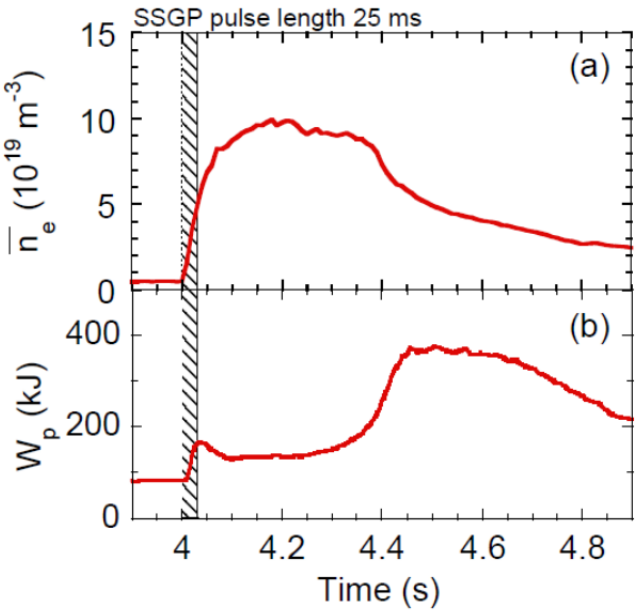

Fig. 3.9 Temporal evolutions of (a) the line-averaged density and (b) the plasma stored energy, in the case of "reheat" after the short pulse SSGP with a pulse length of 25 ms and a backing pressure of ~6 MPa.

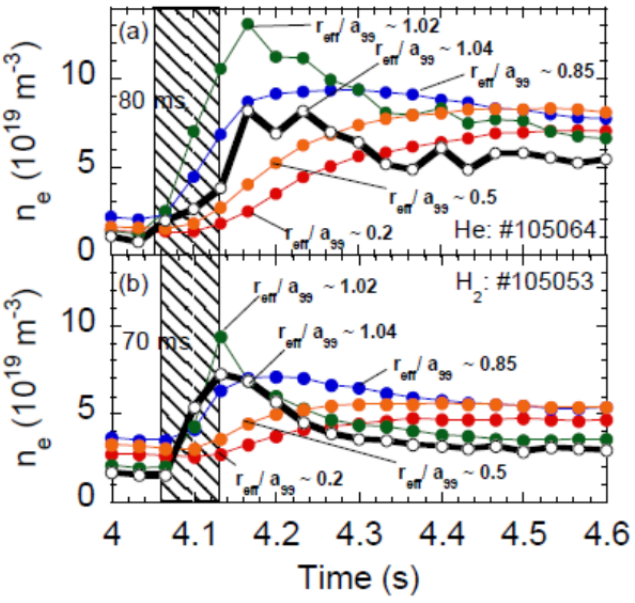

Fig. 3.10 Temporal evolutions of the electron density at different r_{eff}/a_{99} in the cases of (a) He and (b) H_2 SSGP. The pulse lengths of He and H_2 SSGP is 80 ms and 70 ms, respectively.

Bibliography of Chapter 3

[1] A. Murakami et al., Plasma Fusion Res. **5**, S1032 (2010).

[2] A. Murakami et al., J. Plasma Fusion Res. SERIES **9**, 979 (2010).

[3] J. Miyazawa et al., Fusion Sci. Tech **58**, 200 (2010).

[4] B. J. D. Tubbingb et al., Nucl. Fusion **32**, 967 (1992).

[5] J. Miyazawa et al., Nucl. Fusion **44**, 154 (2004).

[6] J. Miyazawa et al., Fusion Eng. Des. **83**, 265 (2008).

[7] K. Narihara et al., Rev. Sci. Instrum, **72**, 1122 (2001).

[8] I. Yamada et al., Fusion Sci. Tech **58**, 345 (2010).

[9] B. Pegourie et al., J. Nucl. Mater. **313**, 539 (2003).

[10] C. Y. Chen et al., J. Plasma Fusion Res. SERIES **9**, 37 (2010).

[11] S. Sudo et al., Nucl. Fusion **30**, 11 (1990).

[12] J. Miyazawa et al., Nucl. Fusion **48**, 015003 (2008).

[13] S. Morita et al., Proc. 14th Int. Conf. Plasma Physics and Controlled Nuclear Fusion Research, Germany, 2, p515, (1992).

[14] M. Isobe et al., Fusion Sci. Technol. **50**, 229 (2006).

Chapter 4

Plasma physics experiments using SSGP

4.1 Introduction

SSGP can be also used for plasma physics experiments. Various phenomena are induced by SSGP, such as the reheat of the plasma stored energy, the strong edge cooling and the nonlocal transport. The electron temperature fluctuations related to the MHD instability are induced after the nonlocal phenomenon. SSGP is also capable of inducing the fast density modulation externally by using fast pulse train. The fast density modulation of 50 ~ 200 Hz was excited by SSGP. SSGP has an additional effect of edge cooling that will be beneficial for divertor heat load reduction. SSGP is also available as the fueling method which triggers a variety of plasma responses by supplying a large numbers of particles in a short time. These results will be beneficial for future fusion reactors.

In this chapter, these plasma physics experiments using SSGP are discussed. the reheat of the plasma stored energy is reported in Section 4.2. The effect of the strong edge cooling is discussed in Sections 4.3. The nonlocal transport and the electron temperature fluctuations triggered by SSGP are revealed in section 4.4. The results of the fast density modulation experiments are reported in section 4.5. Fueling to the long pulse plasma discharge using ICRF heating is reported in section 4.6. Finally, these are summarized in Section 4.7.

4.2 Reheat discharge using SSGP

Improvement of plasma performance after turning off the conventional gas puffing ("reheat mode") had been observed in not only small-scale helical devices such as CHS but also in LHD [1-3]. "Reheat" of the plasma stored energy after a short pulse SSGP using the ϕ0.6L Laval nozzle was also observed. Figures 4.1(a) and 4.1(b) show the time evolutions of the line-averaged density and the plasma stored energy in a "reheat" discharge. In this discharge, R, a, B_t, and P_{NB} were 3.6 m, 0.6 m, 1.0 T, and 14 MW, respectively. SSGP was injected through the ϕ0.6L Laval nozzle at t = 4.0 s with a short pulse length of 25 ms and a high backing pressure of ~6 MPa. With this pulse length, the amount of supplied particle is ~ 13.6 Pa·m^3. The plasma shrunk and the density increased largely after the short pulse SSGP. The plasma stored energy was once decreased after SSGP and recovered at t ~ 4.4 s. This phenomenon is what we call "reheat". Figure 4.1(c) shows time evolution of the flux into divertor measured by Langmuir probe arrays embedded on divertor plates. The flux was also decreased after SSGP and increased at t ~ 4.4 s accompanying of the behavior of the plasma stored energy.

Figure 4.2 shows the radial profiles of (a) electron density and (b) electron temperature at t = 4.1 s and t = 4.5 s. As seen in the figure 4.2(a), while the density at t = 4.1s is formed hollow profiles and the density in the region of r_{eff} > 0.3 m is higher than the Sudo limit, the density at t = 4.5 s after reheat of plasma stored energy is formed parabola profile. Figure 4.2(b) shows the core electron temperature was recovered by two times higher than the temperature just after SSGP.

In Figs 4.1(a) and 4.2(b), the blue line denotes the discharge of not "reheat" with ordinary ϕ0.6 Laval nozzle, where the pulse length of 25 ms and the backing pressure of 6 MPa is the same value of reheat discharge with ϕ0.6L Laval nozzle. In the case of ordinary ϕ0.6 Laval nozzle, plasma did not shrink even though the same amount of

particles were supplied. It presumably indicates that the converged gas flow ejected through the ϕ 0.6L Laval nozzle is effective to make the plasma shrink.

Figure 4.3 shows the bata value of plasma core region as a function of core electron density in cases of the pellet injection, this reheat discharge of SSGP and the conventional gas puffing. As seen figure 4.3, the property of the reheat discharge with SSGP indicates intermediate between the pellet injection and the conventional gas puffing.

4.3 Edge cooling effect

SSGP has an additional effect of plasma edge cooling. Figure 4.4 shows radial profiles of electron temperature and density in two discharges fuelled by GP or SSGP. In these discharges, R, a, B_t, and P_{NB} were fixed to 1.0 T, 3.6 m, 0.6 m, and 14 MW, respectively. SSGP was injected at t = 4.0 s with the pulse length of 60 ms. In the figure, the profiles before SSGP (denoted by "SSGP t = 4.000 s"), during SSGP ("SSGP t = 4.033 s"), just after SSGP ("SSGP t = 4.066 s"), and 40 ms after SSGP ("SSGP t = 4.100 s"), are compared with those in a reference discharge fuelled by normal gas puffing ("GP"). As seen in the figure, the edge temperatures at $r_{eff} \sim 0.65$ m (see shaded regions) during SSGP (SSGP t = 4.033 s) and just after SSGP (t = 4.066 s) were more than 50 % lower than that in the case of GP, in spite of the similar edge density. This observation clarifies that SSGP is able to cool the edge plasma within a short time of less than 0.1 s. A similar edge cooling effect of SPGI was also reported in Tore supra [4]. This strong edge cooling effect was, however, transient. The temperature 40 ms after SSGP (t = 4.100 s) was rapidly recovered to the same values as those before SSGP (t = 4.000 s).

The reason why the edge temperature becomes low just after SSGP is not understood yet. The difference in the flow rate and/or the convergence of gas flow

between SSGP and GP might be the key to consider the physics of this strong edge cooling effect. Nevertheless, this strong edge cooling effect will be beneficial for divertor heat load reduction, which is inevitable in future fusion reactors, since the low edge temperature enhances the radiation loss in the ergodic layer and reduces the conduction loss to the divertor plates.

4.4 Non-local transport phenomena triggered by SSGP

4.4.1 Non-local transport phenomenon

Non-diffusive heat transport, which cannot be explained by ordinary local diffusion, has been observed in magnetically confined toroidal plasmas. Many kinds of peculiar non-local transport phenomena have been reported by both tokamak and helical experiments [5-10]. For example, an edge cooling perturbation can cause the core electron temperature to start increasing under certain conditions. In the Large Helical Device (LHD), non-local transport is triggered by a small hydrogen ice pellet injection, a small impurity pellet (tracer-encapsulated solid pellet, TESPEL) injection, or Ar gas puffing [8, 9].

SSGP is able to generate convergent gas flow, and short-pulse SSGP causes a rapid density increase, like that observed in pellet injection experiments. In SSGP, the number of fueled atoms, the timing, and the number of injections are continuously variable. This flexibility makes SSGP a valuable tool for studying non-local transport. In this section, experimental results on non-local transport triggered by SSGP are reported.

4.4.2 Non-local transport phenomenon triggered by SSGP

Figures 4.5 (a) and 4.5(b) show the time evolution of the electron temperature T_e, measured by an electron cyclotron emission (ECE) radiometer, for various values of the

normalized minor radius ρ, where a TESPEL was injected at t = 2.59 s and SSGP was injected at t = 2.80 s with a pulse length of 200 μs. The pulse length was shorter than that of SMBI, which had a pulse length of 3 ms and a backing pressure of 0.5 MPa and triggered non-local transport phenomena in the HL-2A tokamak [10]. In case of SSGP for this experiment, the working gas was hydrogen and the backing pressure was 1.2 MPa. SSGP is expected to generate more convergent and shorter-pulse gas flow compared with SMBI. The supplied particle number was estimated to be 2.2×10^{19} particles for the TESPEL injection and 2.4×10^{20} particles for SSGP. The target plasma was produced by electron cyclotron heating (ECH) of ~0.8 MW and neutral beam injection (NBI) of ~1.4 MW in the counter direction. The radial absorbed position of ECH power is estimated to be $\rho \sim 0.2$ from calculations of the the vacuum magnetic surface. The magnetic field strength on the magnetic axis, B_t, was 2.85 T. The major and minor radii of the plasma were 3.6 m and 0.6 m, respectively.

Figures 4.5(c) and 4.5(d) show temporal evolutions of the line-averaged electron density $\overline{n_e}$. Figures 4.5(e) and 4.5(f) show the NBI deposition power P_{dep}, which is estimated by subtracting the shine-through power from the port-through power. Figures 4.5(g) and 4.5(h) show the plasma current. Figure 4.5(a) shows non-local transport triggered by the TESPEL injection at t = 2.59 s. The line-averaged electron density increased by 0.1×10^{19} m^{-3} after SSGP. Then, the electron temperature increased in the core region while it decreased in the edge region, thus exhibiting non-local transport. Temporal evolutions of the line-averaged electron density and the plasma current were similar for both the TESPEL injection and SSGP. The profiles of ι are presumed to be unchanged at the time of the TESPEL injection and SSGP. The plasma current was ~−50 kA in both cases.

Figure 4.6 shows radial profiles of the electron density measured by a YAG Thomson scattering system before (t = 2.566 s) and after (t = 2.600 s) the TESPEL injection (Fig. 4.6(a)), and before (t = 2.800 s) and after (t = 2.833 s) SSGP (Fig. 4.6(b)). Solid lines in Figs. 4.6(a) and 4.6(b) denote the density difference between before and

after injection. Radial positions of notable increase in the electron density profile are ρ ~ 0.8 and ρ ~ 0.6 for the TESPEL injection and SSGP, respectively. In both cases, peaks in the radial profile after injection at $\rho > 0.8$ were observed. The peak of the density increase indicates that the supplied particles were mainly ionized at $\rho \sim 0.8$. According to the time evolutions of the electron density profiles, the peak for the TESPEL injection decreased in ~ 40 ms, but the peak for SSGP was maintained for ~ 80 ms. In addition, there is another peak in the electron density profile after SSGP at $\rho \sim 0.6$. This peak was maintained during this phenomenon. The radial position of the particle deposition estimated from the decrease in the electron temperature at various normalized minor radii measured by ECE is $\rho = 0.6 – 0.9$ for the TESPLE injection and $\rho = 0.8 – 0.9$ for SSGP (Figs. 4.5(a) and 4.5(b), respectively). Indeed, the penetration depth evaluated from ablation signals from the TESPEL injection is $\rho \sim 0.8$. The core density was not affected by the TESPEL injection. This is a typical characteristic of non-local transport phenomena. In contrast, the core density was increased by SSGP. This different effect on the core density is caused by the difference in supplied particle number between the TESPEL injection and SSGP.

In the LHD, non-local transport phenomena triggered by Ar gas puffing were also observed [9]. For Ar gas puffing, the delay time, which corresponds to the time from injection to core electron temperature increase, is longer than that for the TESPEL injection. The delay time for Ar gas puffing was estimated to be 50 ms. In this experiment, the delay time for SSGP was ~10 ms, which is longer than that for the TESPEL injection. With regard to the plasma delay time, SSGP has intermediate properties between Ar gas puffing and TESPEL injection.

Figure 4.7(a) shows the temporal evolutions of the electron temperature at ρ = 0.23 for both the TESPEL injection and SSGP. At $t - t_1 = 0 – 0.01$ s, where t_1 denotes the time when the electron temperature started to increase, the increase rates of the electron temperature are similar in both cases. However, SSGP created a longer temperature increase than the TESPEL injection. The reason for this is not understood

yet. However, the increment of the electron temperature depends on the ECH power and the electron density, as reported by a previous study [8].

Figure 4.7(b) shows the radial profiles of the electron temperature before (t = 2.800 s) and after (t = 2.866 s) SSGP. The central electron temperature increased from ~2.3 to ~3 keV after SSGP, while the edge electron temperature remained unchanged.

4.4.3 Observation of temperature fluctuation

Fluctuations were observed in the electron temperature around $\rho \sim 0.5$ at t = 2.86 – 2.93 s in this discharge (See Fig. 4.5). The frequency of the fluctuations increased from ~400 Hz to ~1 kHz, while the amplitude decreased. Figure 4.8(a) shows enlarged waveforms of the electron temperature fluctuations, and Fig. 4.8(b) shows the radial profile of the rate of change in the electron temperature. As can be seen in this figure, the temperature fluctuations inside and outside of $\rho \sim 0.5$ had opposite phases. In other words, the radial gradient of the electron temperature at $\rho \sim 0.5$ repeatedly became steep and mild.

Noted that no significant confinement degradation due to this electron temperature fluctuation was recognized. Indeed, as shown in Fig. 4.7(b), the electron temperature profile at t = 2.866 s, where the electron temperature fluctuation was observed, was similar to that at t = 2.933 s, where the temperature fluctuation was negligibly small.

4.4.4 Rotating magnetic structure and the temperature fluctuation

Magnetic fluctuations of poloidal mode number m = 2 were also observed with the electron temperature fluctuations. The poloidal rotation of these magnetic fluctuations, measured by saddle loops set at different poloidal angles, is shown in Fig. 4.9. The mode structure propagated in the ion-diamagnetic direction. The rotation frequency and amplitude of the magnetic fluctuations showed similar characteristics to those of the electron temperature fluctuations: the frequency increased from ~400 Hz to ~1 kHz and the amplitude decreased correspondingly. This correlation suggests that the

electron temperature fluctuations were caused by the rotating magnetic mode structure. In the magnetic configuration used in this study, a rational surface of $m/n = 2/1$, where n is the toroidal mode number, is located at $\rho \sim 0.5$, assuming a vacuum magnetic surface. As was discussed in the previous section, the radial gradient of the electron temperature at $\rho \sim 0.5$ repeatedly became steep and mild (Fig. 4.8). In the LHD, it has been frequently observed that $m/n = 2/1$ magnetic fluctuations can cause local flattening in the electron temperature profile at its resonant position [11]. It is also possible to generate this flattening artificially using resonant magnetic perturbation coils placed in the LHD [12]. If the $m/n = 2/1$ magnetic island rotates, the temperature gradient at $\rho \sim 0.5$ may become steep (or mild) as the X-point (or O-point) of the island passes by the line of sight of the measurement. The magnetic intensities of these fluctuations were one order lower than that of typical $m/n = 2/1$ magnetic islands observed in the LHD. The width of the assumed magnetic islands is estimated to be less than 1 cm from the magnetic intensities. Therefore, local flattening is not obvious at $\rho \sim 0.5$ in the temperature profile shown in Fig. 4.8(b). When these magnetic fluctuations disappeared, the amplitude and width of the magnetic islands decreased. According to these observations, a rotating $m/n = 2/1$ magnetic island is the possible cause of the electron temperature fluctuations observed in the non-local transport phenomenon triggered by SSGP.

4.4.5 Summary of non-local transport and fluctuations

Non-local transport phenomenon triggered by short-pulse SSGP in the LHD was reported. SSGP triggered a longer temperature increase than that triggered by the TESPEL injection. Electron temperature fluctuations were observed around $\rho \sim 0.5$ after the core temperature increased. The frequency of the fluctuations increased and their amplitude decreased within 0.1 s. A rotating magnetic structure with $m = 2$ suggests that a rotating $m/n = 2/1$ magnetic island is the cause of these electron temperature fluctuations.

A similar correlation between electron temperature fluctuations and a rotating m/n = 2/1 magnetic island was reported in JT-60U [13], where neoclassical tearing modes (NTMs) cause magnetic island formation. Characteristics of NTMs in helical plasmas and their role in non-local transport phenomena are, however, not yet understood and remain for future studies.

4.5 Fast density modulation

4.5.1 Density modulation

Density and/or temperature fluctuations related to the MHD instabilities and micro instabilities are always observed in plasma experiments. Especially, anomalous transport driven by micro instabilities is thought to be playing an important role in determining the confinement property of the plasma. It is therefore desired to find a method to control the instabilities of the order of kHz to MHz to mitigate the anomalous transport and improve the confinement property.

On the other hand, density modulation of the order of 1 Hz using normal gas puffing has been carried out to estimate the particle transport coefficient [14]. Repetitive injection of small hydrogen ice pellet of the order of 10 Hz has been shown to be effective for controlling ELMs in tokamaks [15]. It has been, however, difficult to drive the density fluctuation of the order of kHz.

In this section, basic characteristics of the SSGP device (Section 4.5.2) and results of the fast density modulation experiment carried out in LHD (Section 4.5.3) are discussed. The results of ELM mitigation experiments using the fast density modulation by SSGP is described in Section 4.5.4.

4.5.2 Test results

Preliminary experiments using the solenoid valves and Laval nozzles were carried

out in a test stand [16,17]. To visualize the gas flow, the working gas was cooled by using the refrigerator and cluster beams were formed. Continuous visible laser light intersecting the gas flow at a few cm from the exit of the Laval nozzle was applied and the laser light scattered by the cluster beam was detected by a fast camera. Figure 4.10 shows typical time evolution of the scattering signal from the supersonic hydrogen cluster beam. In this case, the valve was operated at 500 Hz with the pulse length of 50 μs. Then, the scattered light fluctuating at 500 Hz was observed as shown in Fig. 4.10. Figure 4.10 also shows that the scattering signals from clusters were not uniform. It indicates that the averaged cluster size and number density of the clusters varied when the valve was operated with high frequency.

4.5.3 Fast density modulation experiments

Figure 4.11(a) shows the typical waveform of the line density at the plasma edge region measured by a far infrared laser interferometer (FIR) [18]. In this experiment, the working gas was hydrogen and the backing pressure was ~1 MPa. The magnetic field strength on the magnetic axis was 1.5 T. The major radius and the minor radius of the plasma torus were 3.75 m and 0.6 m, respectively. The line-of-sight of FIR No.1 channel passes through the plasma edge region including the so-called ergodic layer in LHD. The pulse length and the injection cycle of SSGP were set to 1 ms and 50 Hz, respectively. SSGP was injected during 3.5 - 4.3 s. As seen in the figure, the fast density modulation was excited by SSGP. The increasing rate of the density signal was changed at ~3.7 s. This might be reflecting the density dependence of the fueling efficiency of SSGP. Further investigation on this is, however, remained for future studies.

Figure 4.11(b) shows the Fourier spectrum of the line density signal shown in Fig. 4.11(a). A large peak is recognized at 50 Hz, which corresponds to the injection cycle of SSGP. Higher harmonics that might be related to the peak of 50 Hz are also observed at 100 and 200 Hz (and presumably at 150 Hz, although it is unclear).

To excite the fast density modulation, the Laval nozzle and the backing pressure,

i.e., the flow rate of SSGP, should be chosen carefully. Even at a high backing pressure of 2.5 MPa, the 0.1 mm Laval nozzle was not effective for fast density modulation excitation since the density perturbation by each pulse was so small that cannot be detected by FIR. High frequency injection from 0.3 mm Laval nozzle was effective as shown in Fig. 4.11. In the case of 0.6 mm Laval nozzle, on the other hand, the density perturbation was too large and the density of the target plasma increased as a result. The optimum flow rate for fast density modulation experiments in LHD was 40 – 200 $Pa \cdot m^3/s$, which was realized by the 0.3 mm Laval nozzle with the backing pressure of 1 – 5 MPa.

4.5.4 ELM mitigation using SSGP

The fast frequency SSGP was injected to edge localized mode (ELM) plasma. Figure 4.12 shows time evolutions of the divertor line density, the line densities of FIR ch.3 and ch.4, and the ratio of the line densities of FIR ch.3 and ch.4 in this discharge. A fluctuation of ELM starts at $t \sim 5.2$ s. SSGP was injected during 5.3 – 5.6 s. The pulse length and the injection cycle of SSGP were set to 0.15 ms and 100 Hz, respectively. The backing pressure is 0.8 MPa. The frequency of ELM was increased at $t = 5.4$ s and decreased after SSGP. It presumably indicates that the fast density modulation of SSGP is effective to control of the frequency of ELM and mitigate the intensity of ELM. The possibility for pacing of type-1 ELMs in H-mode plasmas by 2 Hz SPGI was investigated in ASDEX-U [19]. Since SSGP is available for fast density modulation of 50 ~ 200 Hz, it is expected to be strong tool to mitigate ELM. Detailed experiments of ELM mitigation using SSGP is a future task.

4.6 Fueling to the long pulse plasma discharge using ICRF heating

SSGP was used as the fueling method of long pulse plasma discharge using ICRF heating. Figure 4.12 shows the time evolutions of line averaged density, electron temperature and ion temperature at core region, the ratio of hydrogen in plasma, and the powers of ICH and ECH. Previous study was revealed that the SPGI reduced wall inventory compared to a similar conventional gas puffing in one long pulse discharge in Tore supra [20]. In long pulse discharge using ICH in LHD, the ratio of hydrogen and helium is significant factor to heat plasma effectively. Since SSGP is more available for adjusting the supplied particles compared with pellet injection, it was selected as the fueling methods in long pulse discharge in LHD.

4.7 Summary

SSGP can be also used for plasma physics experiments. Flux into divertor decreased after SSGP in reheat discharge. SSGP has the additional effect of edge cooling that will be beneficial for divertor heat load reduction. The edge temperatures at during and just after SSGP are more than 50 % lower than that in the case of conventional gas puffing, compared at the similar edge density. This strong edge cooling effect will be beneficial for divertor heat load reduction, which is inevitable in future fusion reactors, since the low edge temperature enhances the radiation loss in the ergodic layer and reduces the conduction loss to the divertor plates.

The nonlocal transport phenomenon and electron temperature fluctuations were triggered by SSGP. After a short-pulse SSGP, the core electron temperature increased while the edge electron temperature decreased. SSGP triggered a longer core temperature increase than that triggered by a small impurity pellet injection. The temperature profile, which was relatively flat inside the half minor radius before SSGP, becomes parabolic after non-local transport was triggered. Fluctuations were excited in the electron temperature signals around the half minor radius. The frequency of these fluctuations increased from ~400 Hz to ~1 kHz within ~0.1 s and the amplitude

decreased correspondingly. The temperature fluctuations inside and outside of the half minor radius had opposite phases. Magnetic fluctuations resonating near the half minor radius were observed simultaneously with the electron temperature fluctuations. Fast density modulation experiments using SSGP has been also carried out in the LHD. The fast density modulation of 50 ~ 200 Hz was excited by SSGP. High-frequency injection (500 Hz) was confirmed in preliminary experiments on the test stand. The achieved frequency of 200 Hz is still smaller than that demonstrated in the test stand of 500 Hz. The optimum flow rate for fast density modulation in LHD was 40 – 200 $Pa \cdot m^3/s$. In the case of 50 Hz injection, higher harmonics of up to 200 Hz was also observed simultaneously. The fast frequency SSGP was injected to ELM plasma. It presumably indicates that the fast density modulation of SSGP is effective to control of the frequency of ELM and mitigate the intensity of ELM.

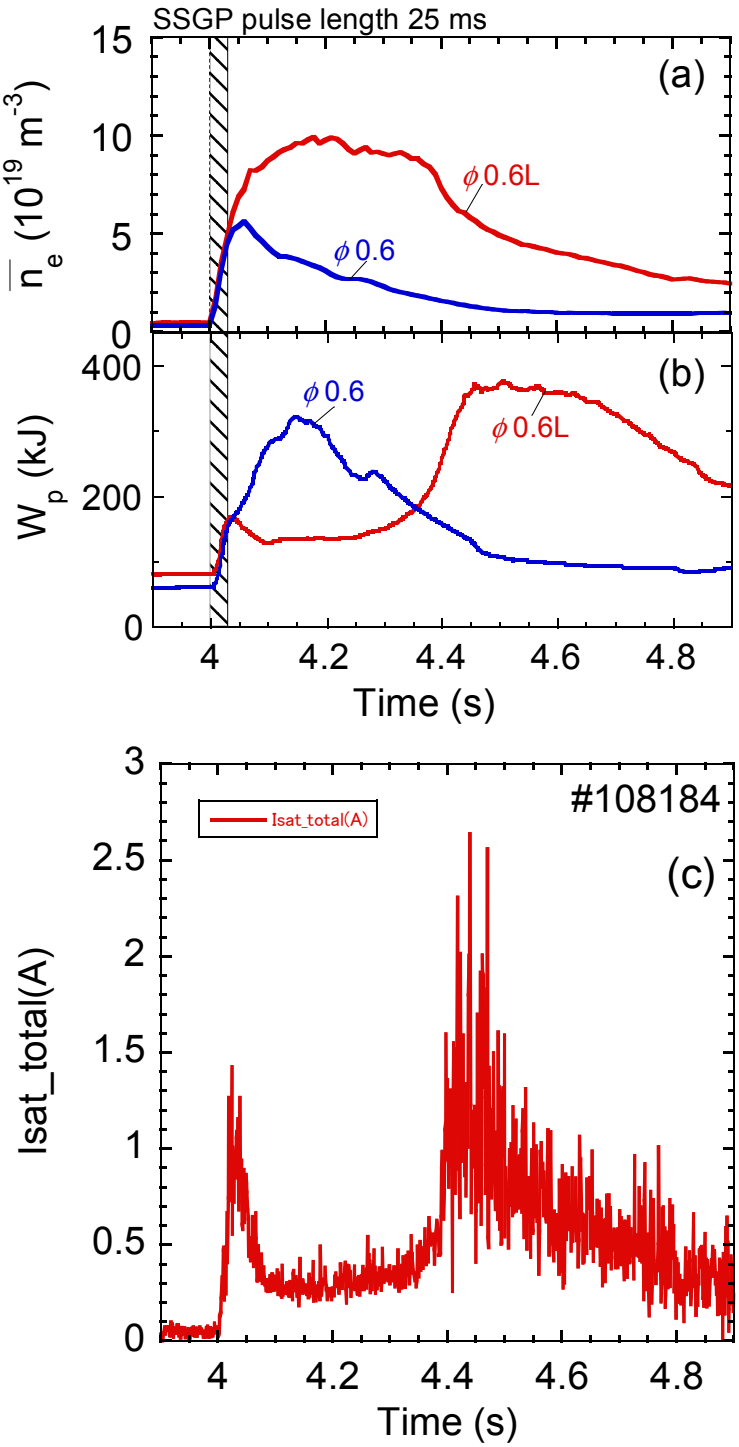

Fig. 4.1 Temporal evolutions of (a) line-averaged density, (b) plasma stored energy and (c) flux into divertor.

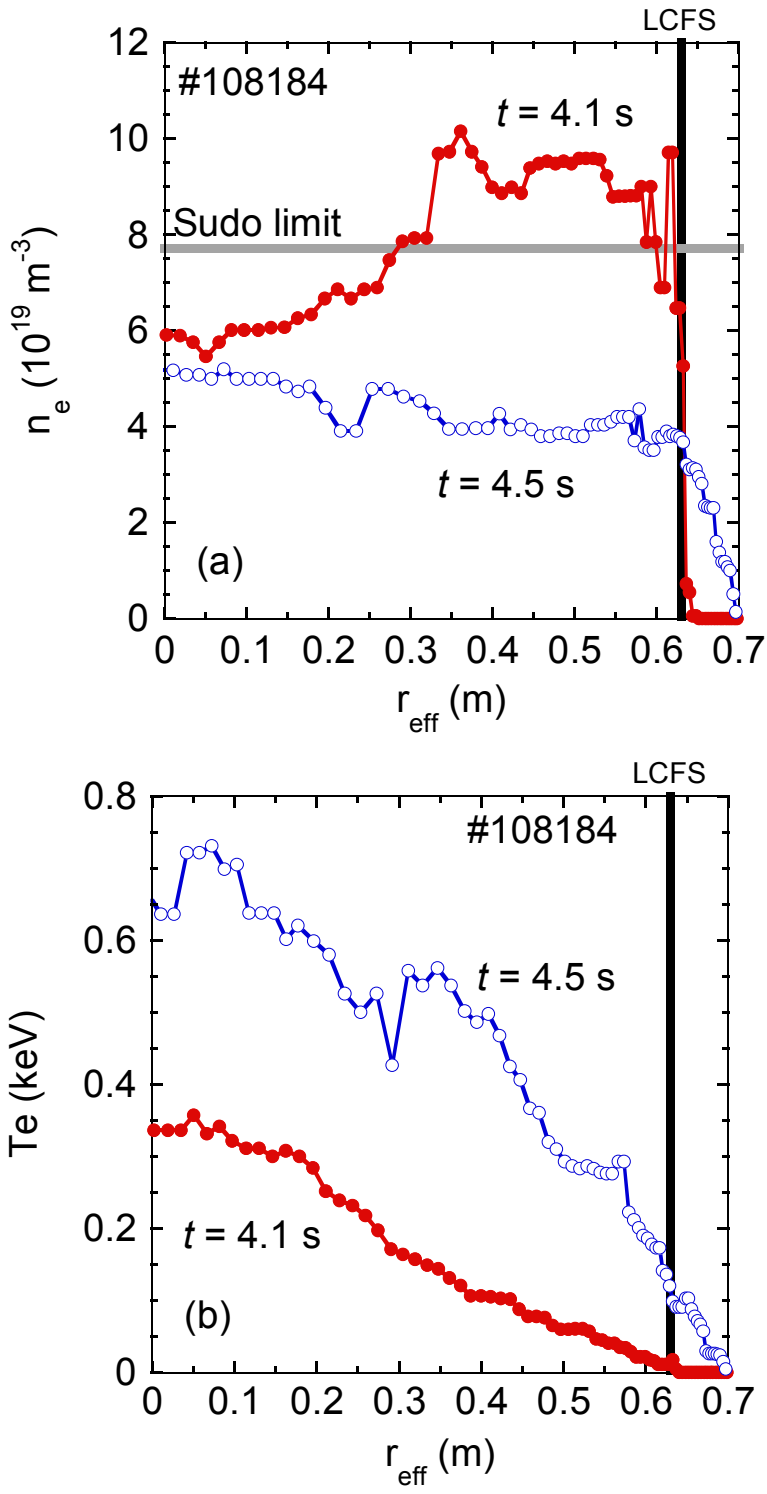

Fig. 4.2 Radial profiles of (a) electron density and (b) electron temperature at t = 4.1s and t = 4.5s in reheat discharge.

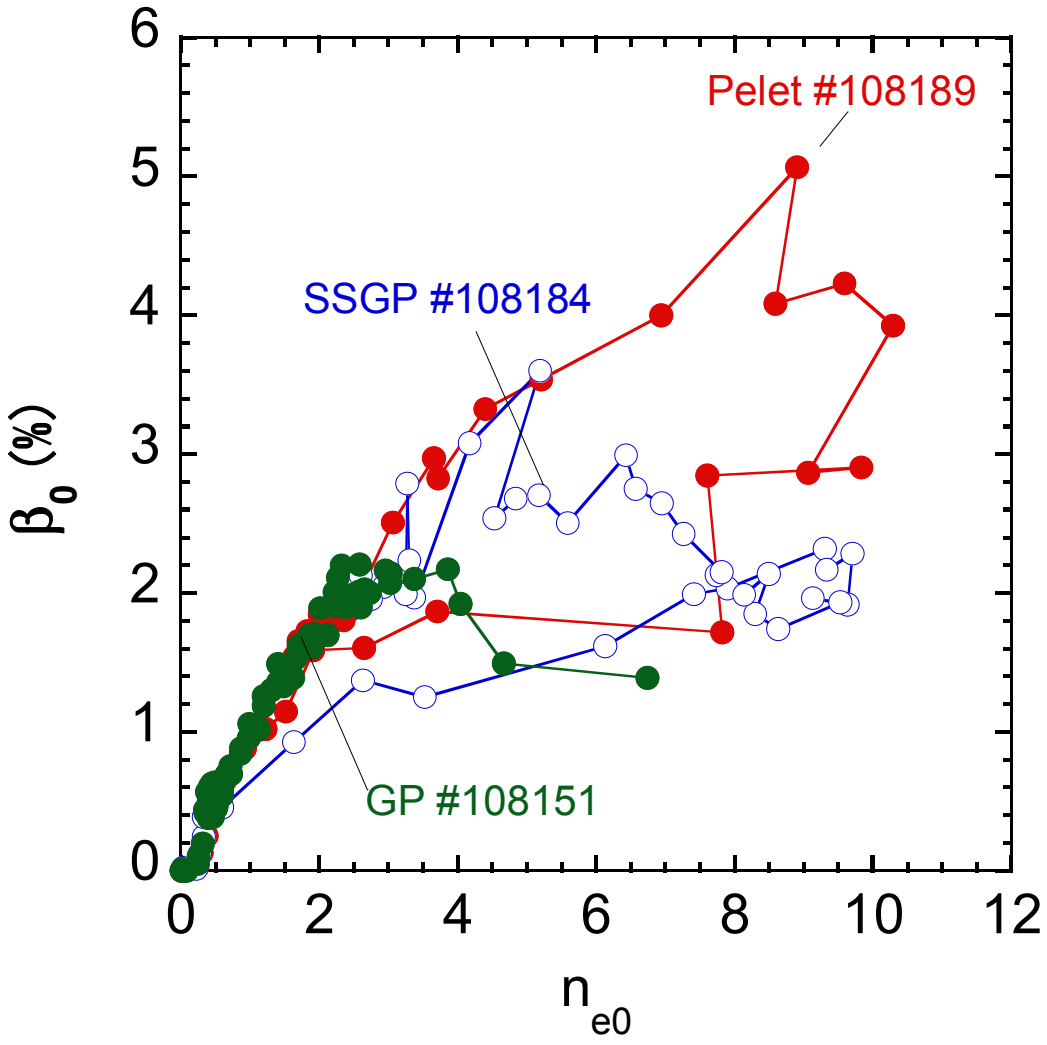

Fig. 4.3 The beta value of core region as a function of electron density of core region in reheat discharge.

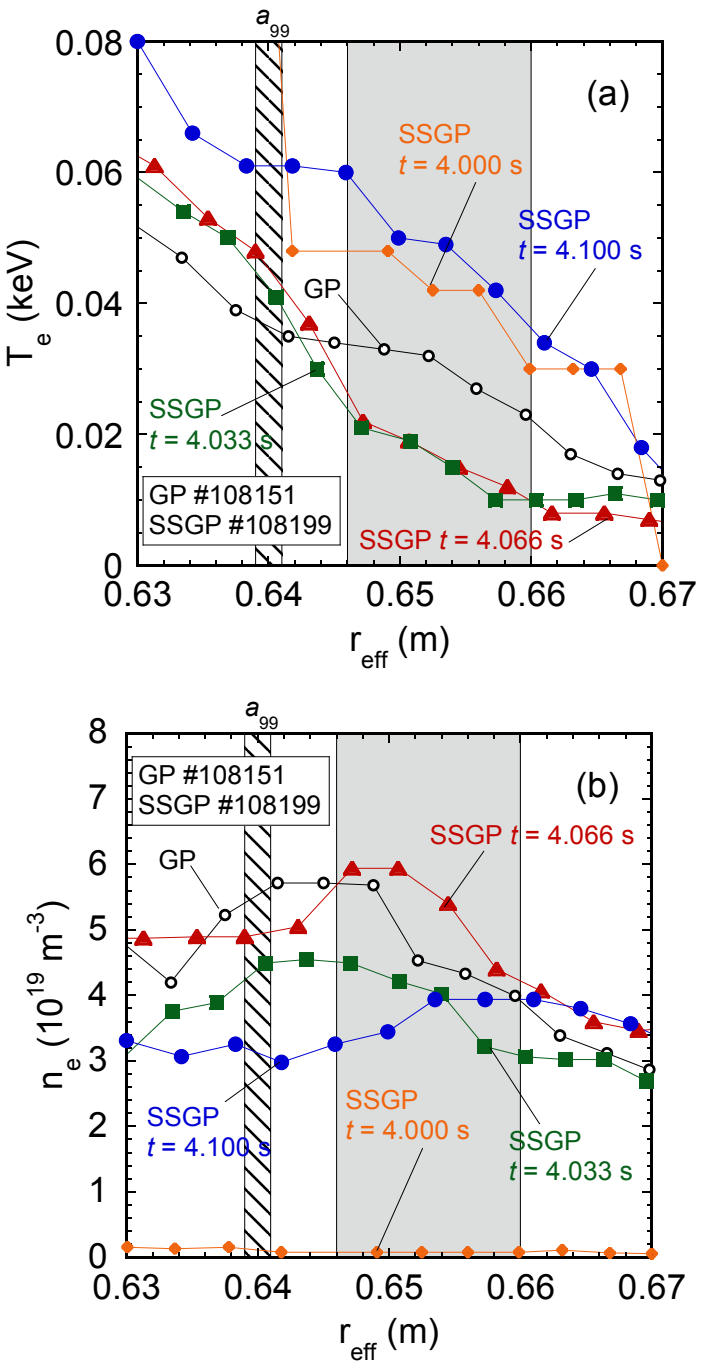

Fig. 4.4 Radial profiles of (a) the electron temperature and (b) the electron density, in two different discharges fuelled by GP (open symbols) or SSGP (closed symbols).

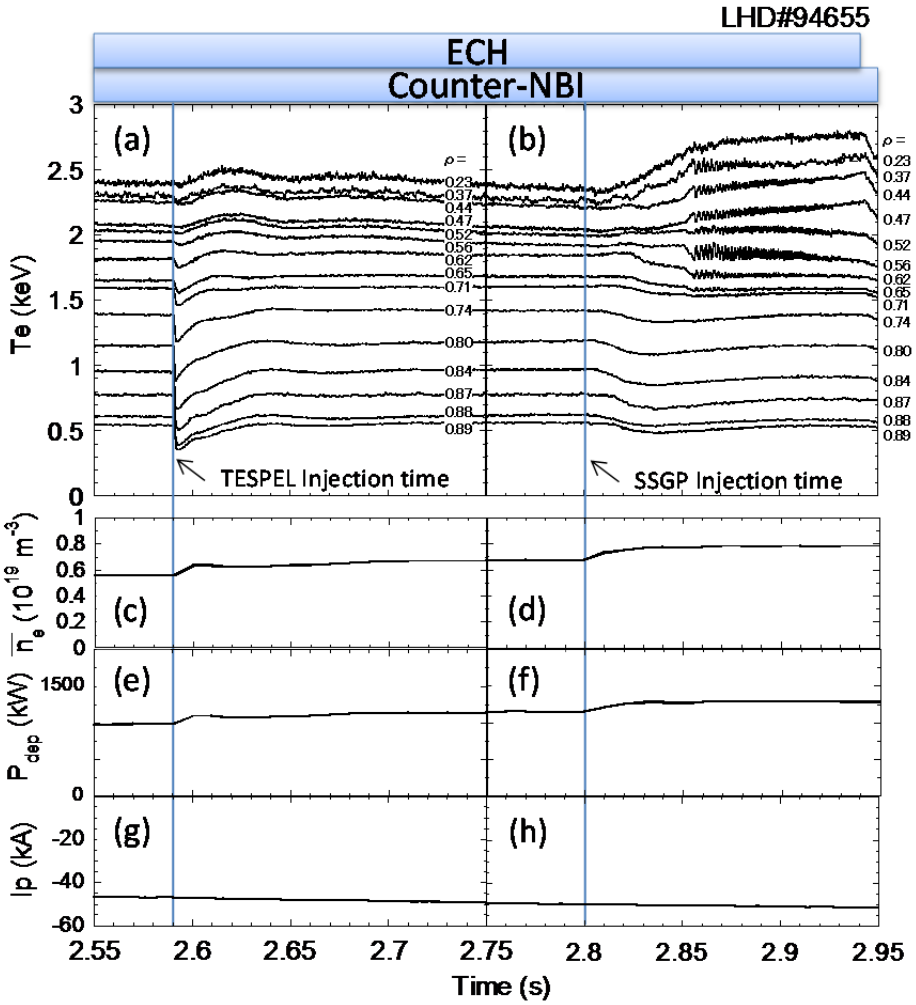

Fig. 4.5 Temporal evolutions of (a) and (b) the electron temperature at different normalized minor radii, (c) and (d) the line-averaged density, (e) and (f) the NBI deposition power P_{dep}, and (g) and (h) the plasma current. Non-local transport phenomena are triggered after the TESPEL injection at t = 2.59 s and SSGP at t = 2.80 s.

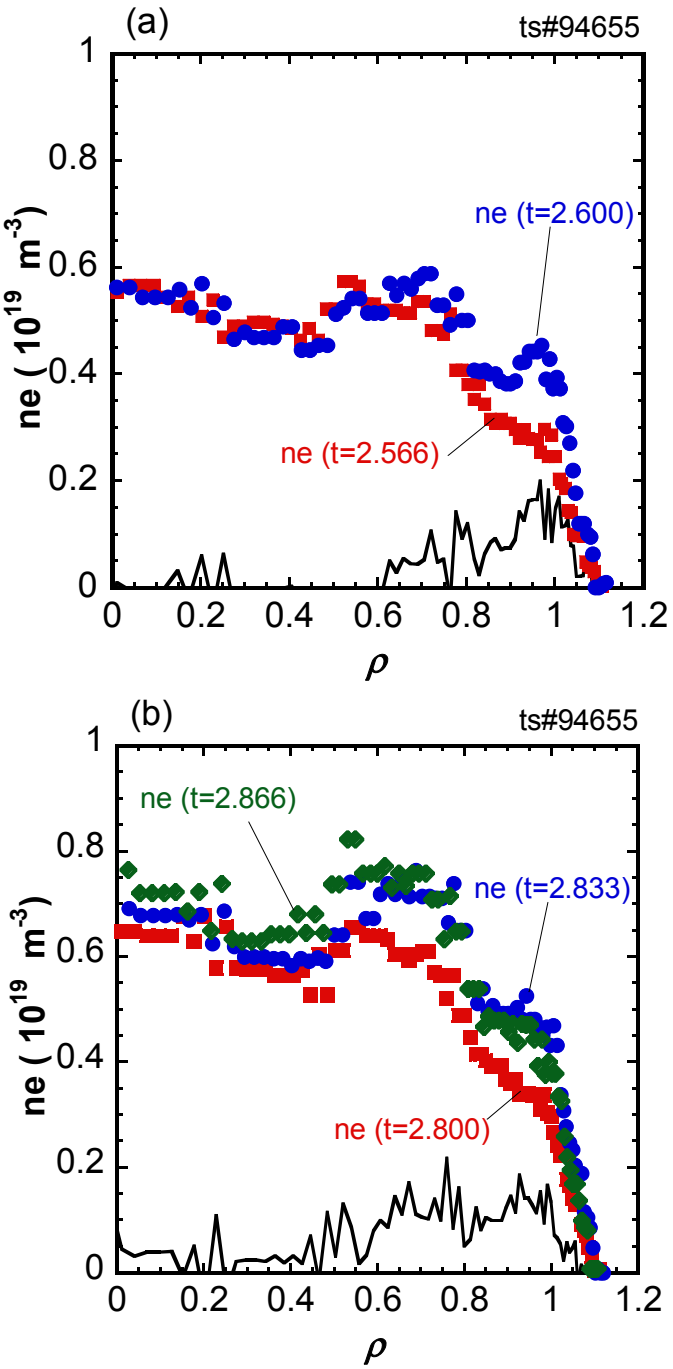

Fig. 4.6 Radial profiles of the electron density (a) before (t = 2.566 s) and after (t = 2.600 s) the TESPEL injection, and (b) before (t = 2.800 s) and after (t = 2.833 s) SSGP. The profile of t = 2.866 s is that with the temperature fluctuation. Solid lines in Figures (a) and (b) denote the difference between before and after injection.

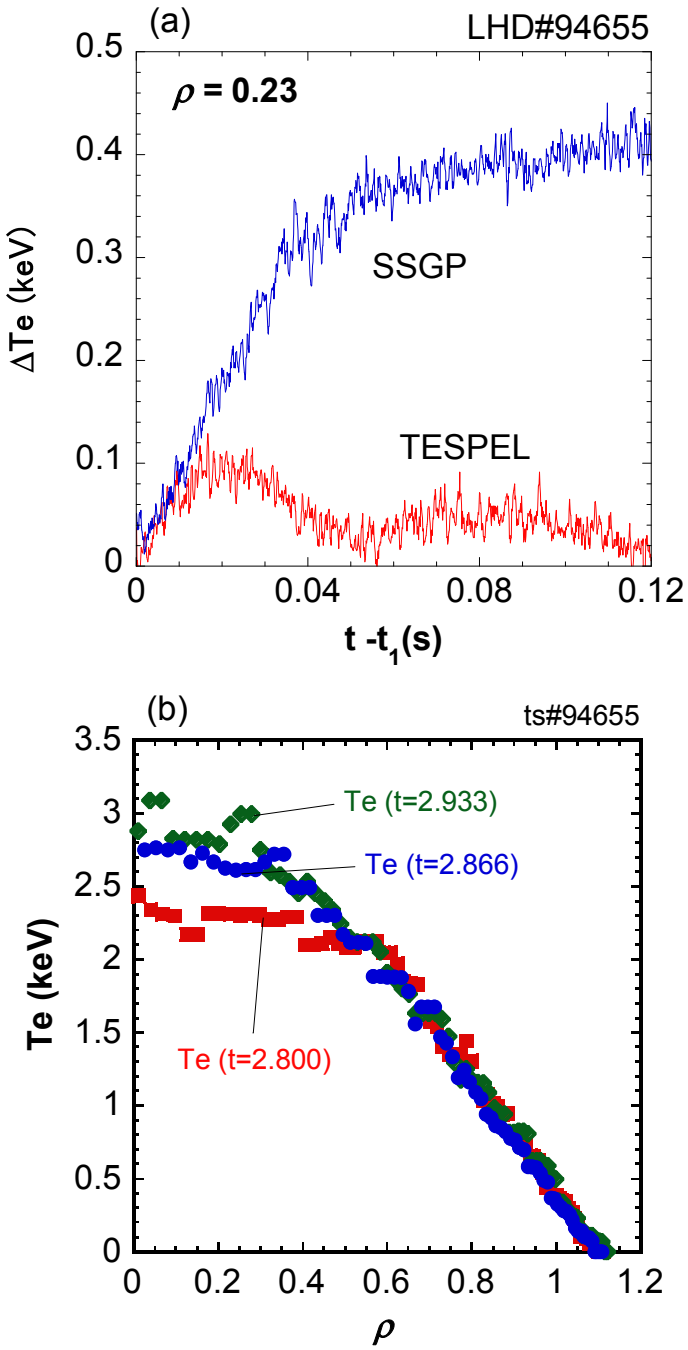

Fig. 4.7 (a) Temporal evolution of the electron temperature at $\rho = 0.23$ (t_1 in the figure is the time when the electron temperature started to increase). (b) Radial profiles of the electron temperature before (t = 2.800 s) and after (t = 2.866 s) SSGP. The profile of t = 2.933 s is that with the electron temperature fluctuation.

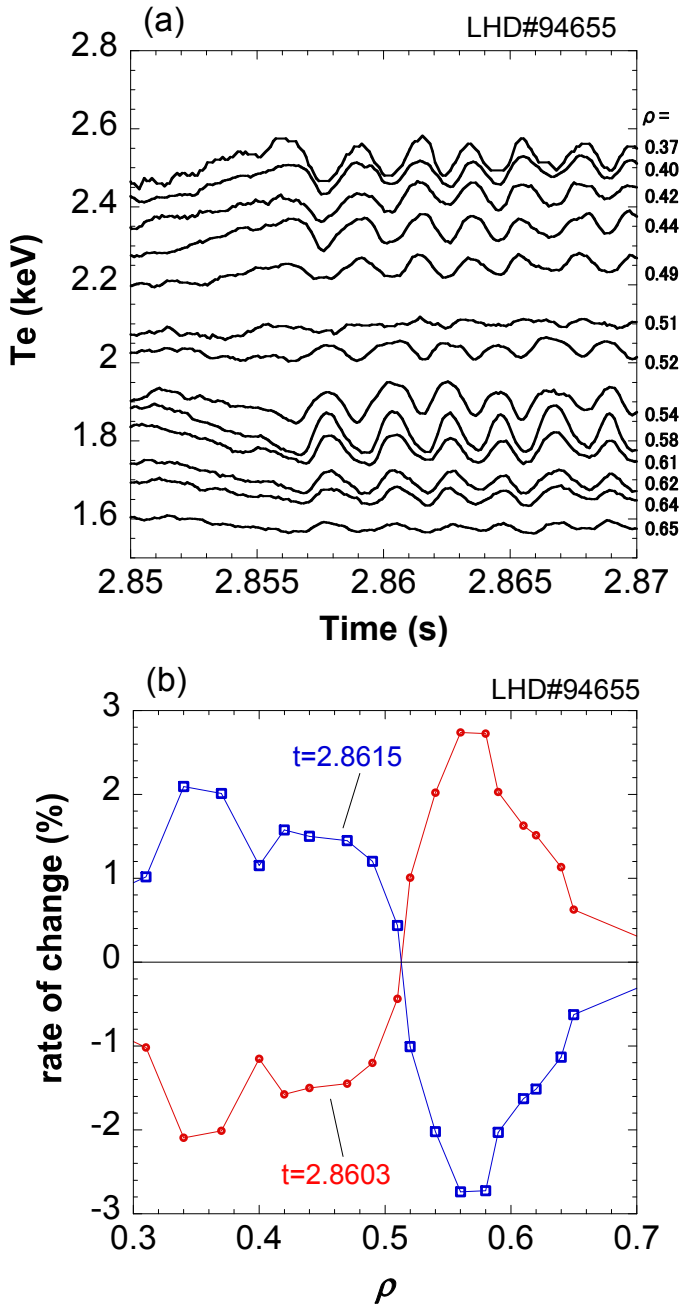

Fig. 4.8 (a) Enlarged waveforms of the electron temperature at $\rho = 0.37 - 0.65$. (b) Radial profile of the rate of change of the electron temperature. The phase of the electron temperature fluctuation inside $\rho \sim 0.5$ is opposite to that outside $\rho \sim 0.5$.

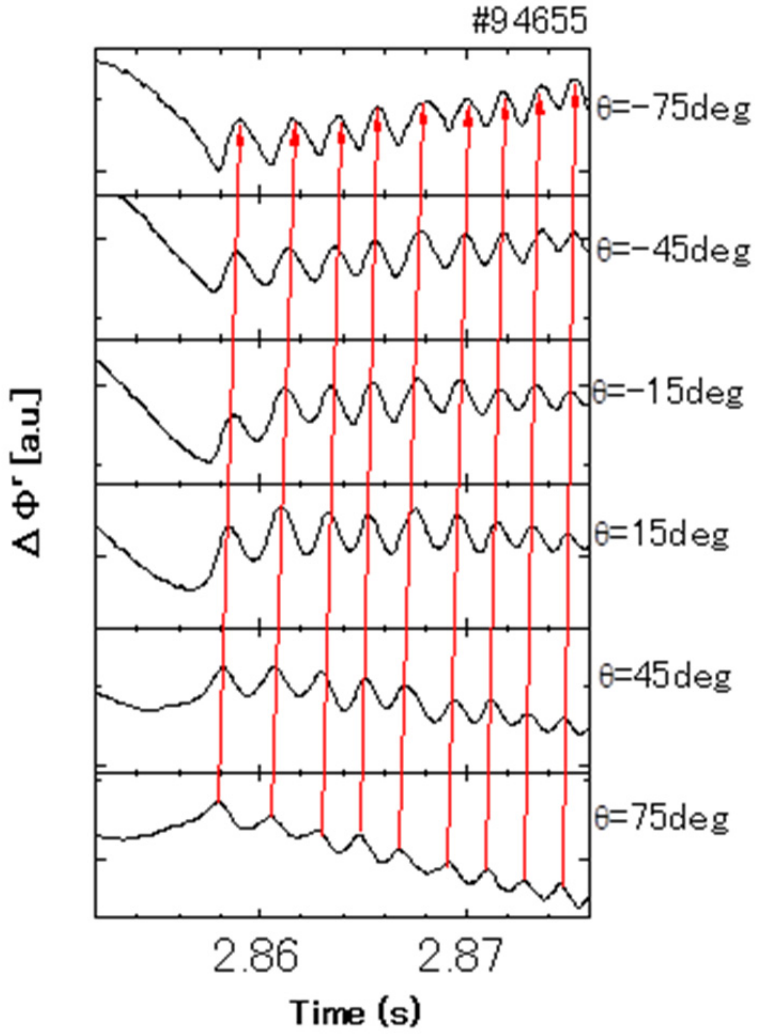

Fig. 4.9 Poloidal propagation of the radial component of the magnetic field measured by saddle loops set at various poloidal angles in the same discharge shown in Fig. 4.5. A coherent structure of poloidal mode number m = 2 is propagating in the ion-diamagnetic direction.

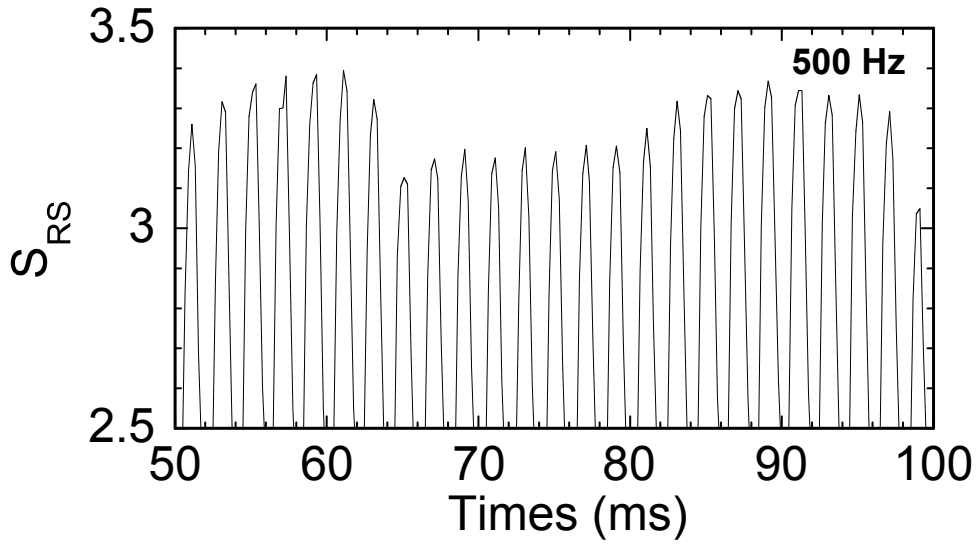

Fig. 4.10 Temporal evolution of the scattered signal from the hydrogen cluster beam ejected through the fast solenoid valve.

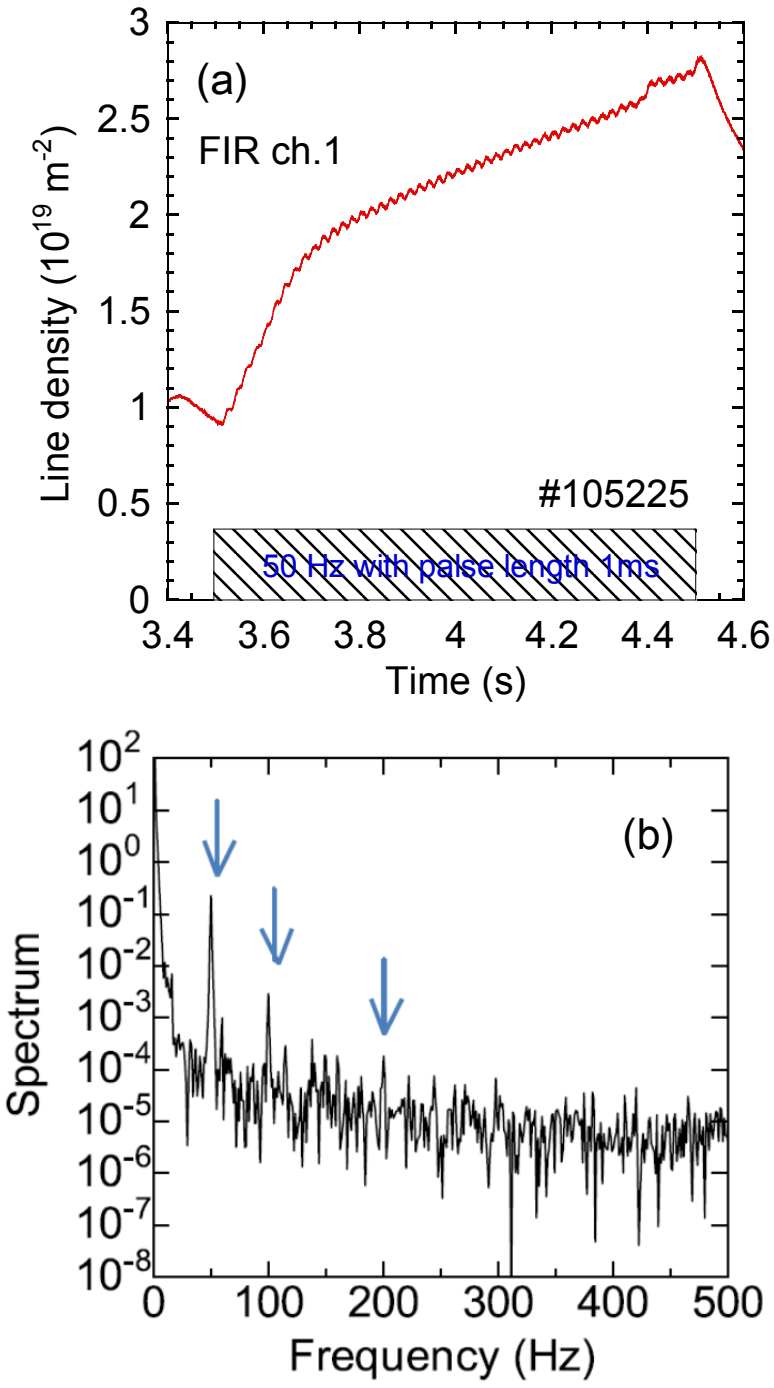

Fig. 4.11 (a) Typical temporal evolution of the line density of FIR ch.1, and (b) the Fourier spectrum of the density fluctuation. SSGP was injected from t = 3.5 s to 4.5 s.

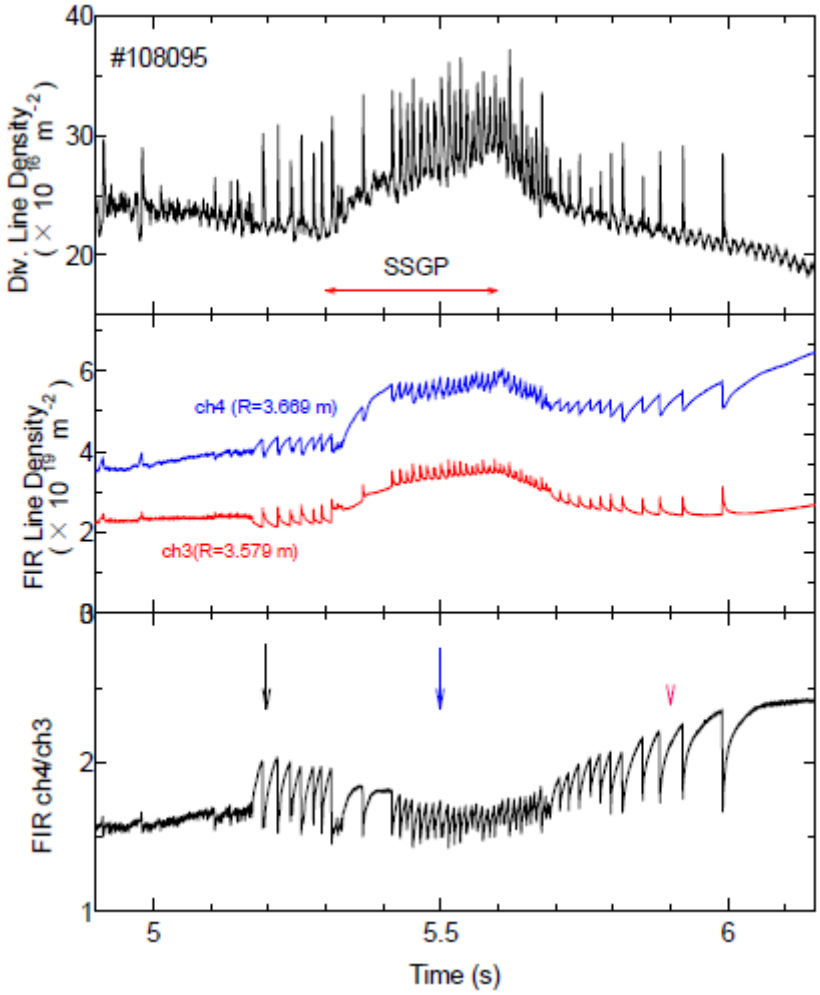

Fig. 4.12 Temporal evolutions of divertor line density, FIR line density, and the ratio of the line density of FIR ch.3 and ch.4 [21].

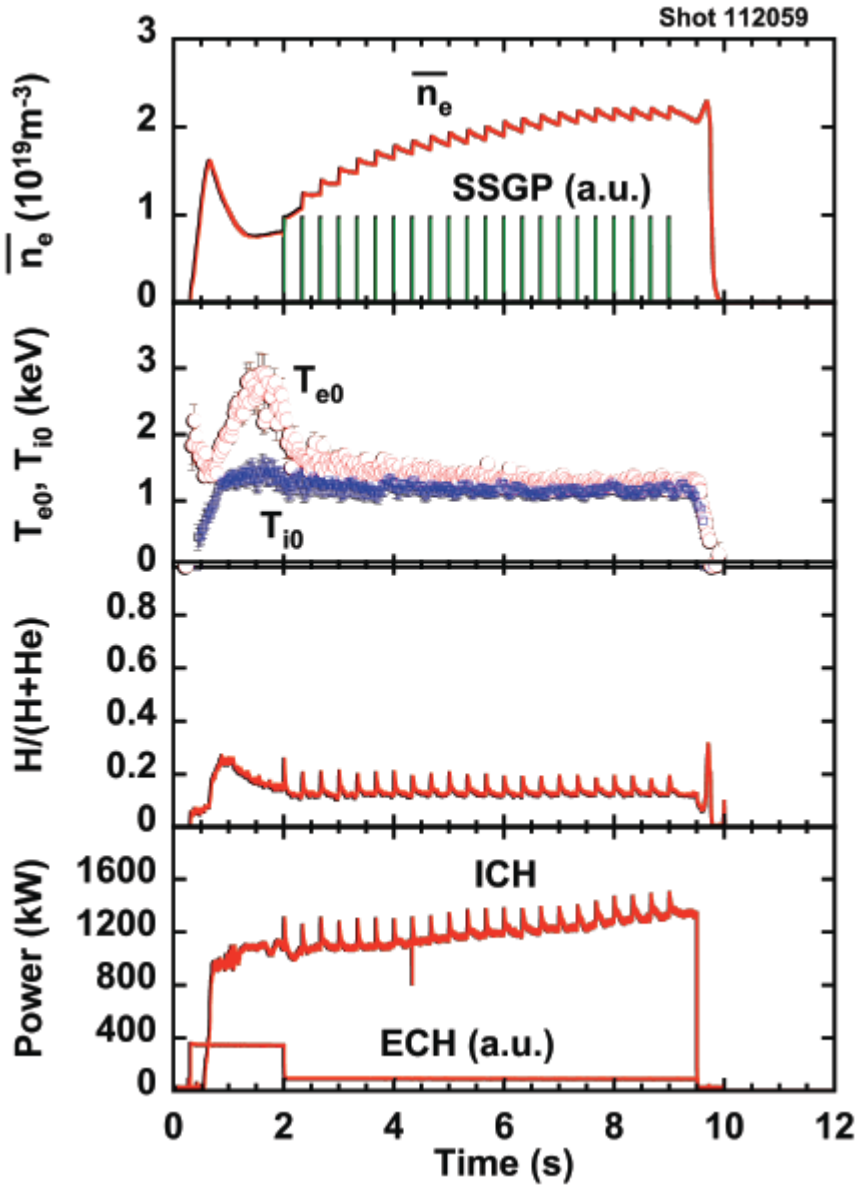

Fig. 4.12 Temporal evolutions of line averaged density, electron temperature and ion temperature at core region, the ratio of hydrogen in plasma, and the powers of ICH and ECH [22].

Bibliography of chapter 4

[1] S. Morita et al., Proc. 14th Int. Conf. Plasma Phys. and Control. Nucl. Fusion Res., Germany, 2, p515 (1992).

[2] M. Isobe et al., Fusion Sci. Technol. 50, 229 (2006).

[3] S. Morita et al., Proc. 28th European Conf. on Control. Fusion and Plasma Phys., Madeira, p73 (2001).

[4] B. Pegourie et al., J. Nucl. Materials **313-316**, 539 (2003).

[5] K. W. Gentle *et al*., Phys. Plasma **2,** 2292 (1995).

[6] F. Ryter *et al*., Nucl. Fusion **40**, 1917 (2000).

[7] M. W. Kissick *et al*., Nucl. Fusion **36**, 1691 (1996).

[8] N. Tamura *et al*., Nucl. Fusion **47**, 449 (2007).

[9] N. Tamura *et al*., Journal of Physics Conference Series **123**, 012023 (2008).

[10] H. J. Sun *et al*., Plasma Phys. Control. Fusion **52**, 045003 (2010).

[11] S. Sakakibara *et al*., PFR **1,** 003 (2006).

[12] Y. Narushima et al., Fusion Sci. Tech. **58,** 194 (2010).

[13] A. Isayama et al., Nucl. Fusion **47**, 773 (2007).

[14] K. Tanaka et al., Fusion Sci. Tech. **58,** 70 (2010).

[15] P. T. Lang et al., Nucl. Fusion **44**, 665 (2004).

[16] A. Murakami et al., Plasma Fusion Res. **5**, S1032 (2010).

[17] A. Murakami et al., J. Plasma Fusion Res. SERIES **9**, 79 (2010).

[18] T. Akiyama et al., Fusion Sci. Tech. **58**, 352 (2010).

[19] P. T. Lang et al., Plasma Phys. Control. Fusion **47**, 1495 (2005).

[20] J. Bucalossi et al., 19th IAEA conf. Lyon, WX/P4-04, (2002).

[21] LHD Experimental diary at September 3, 2011.

[22] LHD Experimental diary at October 24, 2011.

Chapter 5

Summary and conclusion

Establishment of fueling methods in future thermonuclear fusion reactors is one of the critical issues. In a fusion reactor, the role of fueling device is to supply fuel particles and, consequently, to control the plasma density profiles.

SSGP has been developed as a new fueling method that can combine both advantages of the pellet injection and the conventional gas puffing, i.e., simpleness of the device, high fueling efficiency, and rapid response. In SSGP, high-pressure gas is ejected through a fast solenoid valve equipped with the Laval nozzle. SSGP supplies pulsed convergent gas flow to the plasma.

Before applying SSGP to LHD, the effectiveness of the Laval nozzle has been tested by visualizing the gas flow. Three methods have been applied for visualization, i.e., the shadow graph imaging, the emission imaging using electron beam, and the laser scattering after forming the cluster beam. The cluster beam is formed by selecting the gas species, or by cooling the gas using a refrigerator.

As the first step, the cluster beam ejected through the fast solenoid valve without using the Laval nozzle has been investigated by selecting the gas species capable of forming the cluster at a room temperature in a test chamber. Time-resolved 2-D images of Rayleigh scattering from clusters have been measured by a fast charge coupled

device camera. The expansion half angle of the gas flow without the Laval nozzle was 22.5º. The scattering signal was proportional to the averaged cluster size and the number density of clusters. The scattering signals from argon and nitrogen clusters showed approximately cubic dependence on the backing pressure as expected from a model. Meanwhile, stronger pressure dependence than this was found in the case of methane, where the scattering signal increased with the fifth power of the backing pressure at 3.2 MPa – 7 MPa, and it was further enhanced at > 7 MPa. This suggests that a new structure model would be necessary to determine the cluster size of methane, which shows stronger backing pressure dependence than argon and nitrogen.

Next, formation of the hydrogen cluster beam using the Laval nozzle has been investigated at a low-temperature regime ranging from 120 K to 300 K. The Rayleigh scattering signal from hydrogen clusters was detected when the temperature was lower than 178 K, as expected from a calculation result of the cluster formation condition. The scattering signal intensity was inversely proportional to the fifth power of the gas temperature and the cube of the backing pressure as expected from an available cluster model. The divergence of cluster beam has been decreased from 22.5 º to ~5 º after installation of the Laval nozzle.

Based on the test results of the Laval nozzle, fueling characteristics have been investigated in LHD. The fueling efficiency of SSGP depends on the target plasma density and decreases as the density increases. This is due to the fueling mechanism of SSGP, where the fuel particles are supplied to the plasma edge region and then transported to the core region by diffusion. SSGP locally supplies a large number of particles to the edge region within a short time on the order of ms. The fueling efficiency of ~20 % can be achieved by SSGP, which is more than twice higher than that of ordinary gas puffing.

Two kinds of improvement in the fueling efficiency of SSGP have been observed. The fueling efficiency improved suddenly when the target plasma was close to the density limit. In the case of hydrogen SSGP, abrupt increase in the density increase rate

was observed with the plasma shrinkage. As a result of this, the fueling efficiency was improved for two times even though the difference in the number of supplied particles was less than 20 %. The fueling efficiency also improved when the edge-density was kept high and a strongly hollow density profile was maintained. The fueling efficiency of helium SSGP is indeed higher than that of hydrogen SSGP because of the high recycling property.

SSGP can be also used for physics experiments. the nonlocal transport phenomenon and electron temperature fluctuations were triggered by SSGP. After a short-pulse SSGP, the core electron temperature increased while the edge electron temperature decreased. SSGP triggered a longer core temperature increase than that triggered by a small impurity pellet injection. The temperature profile, which was relatively flat inside the half minor radius before SSGP, becomes parabolic after non-local transport was triggered. Fluctuations were excited in the electron temperature signals around the half minor radius. The frequency of these fluctuations increased from ~400 Hz to ~1 kHz within ~0.1 s and the amplitude decreased correspondingly. The temperature fluctuations inside and outside of the half minor radius had opposite phases. Magnetic fluctuations resonating near the half minor radius were observed simultaneously with the electron temperature fluctuations.

Fast density modulation experiments using SSGP has been also carried out in the LHD. The fast density modulation of 50 ~ 200 Hz was excited by SSGP. High-frequency injection (500 Hz) was confirmed in preliminary experiments on the test stand. The achieved frequency of 200 Hz is still smaller than that demonstrated in the test stand of 500 Hz. The optimum flow rate for fast density modulation in LHD was 40 – 200 $Pa \cdot m^3/s$. In the case of 50 Hz injection, higher harmonics of up to 200 Hz was also observed simultaneously.

SSGP has the additional effect of edge cooling that will be beneficial for divertor heat load reduction. The edge temperatures at during and just after SSGP are more than 50 % lower than that in the case of conventional gas puffing, compared at the similar

edge density. This strong edge cooling effect will be beneficial for divertor heat load reduction, which is inevitable in future fusion reactors, since the low edge temperature enhances the radiation loss in the ergodic layer and reduces the conduction loss to the divertor plates.

In conclusion, the fueling efficiency of SSGP is more than twice higher than that of conventional gas puffing. The fueling efficiency improves when the target plasma is close to the density limit during SSGP and the edge-density is kept high and a strongly hollow density profile is maintained. In plasma physics experiments, SSGP caused various interesting phenomena by supplying the short convergent gas flow. SSGP is also available as the fueling method which triggers a variety of plasma responses by supplying a large numbers of particles in a short time. The scientific knowledge obtained in this study will be beneficial for future fusion reactors.

Appendix

Magnetic shield

It is necessary that the solenoid valve for SSGP in LHD is shielded magnetically in order to prevent a mechanical error. A magnetic shield can be designed as follows.

The magnetic field at the position of the solenoid valve in the case of SSGP device in LHD is ~0.1 T (Figs. A1, A2). The shape of the magnetic shield is assumed to be cylindrical.

Calculation of magnetic field in a hollow cylindrical form

Figure A3 shows the model of a hollow cylindrical shield, where the magnetic permeability, inner and outer diameters are μ_2, a and b, respectively. It is assumed that the hollow cylindrical shield is long enough so that the edge effect is ignored. The magnetic potentials in the outer region, inside the cylindrical shield, and the inner region of ϕ_{m1}, ϕ_{m2} and ϕ_{m3}, respectively, are given as follows, from Figure A3,

$$\phi_{m1} = \frac{M_1}{r}\cos\theta - H_0 r\cos\theta, \tag{A.1}$$

$$\phi_{m2} = \frac{M_2}{r}\cos\theta - H_1 r\cos\theta, \text{ and} \tag{A.2}$$

$$\phi_{m3} = -H_2 r\cos\theta, \tag{A.3}$$

The boundary conditions are,

$\phi_{m3} = \phi_{m2,}$ and

$$\mu_1 \frac{\partial \phi_{m3}}{\partial r} = \mu_2 \frac{\partial \phi_{m2}}{\partial r}, \text{ at } r = a. \tag{A.4}$$

$\phi_{m2} = \phi_{m1,}$ and

$$\mu_2 \frac{\partial \phi_{m2}}{\partial r} = \mu_1 \frac{\partial \phi_{m1}}{\partial r}, \text{ at } r = b. \tag{A.5}$$

Then,

$$-H_2 a = \frac{M_2}{a} - H_1 a \tag{A.6}$$

$$-\mu_1 H_2 = \mu_2 \left(-\frac{M_2}{a^2} - H_1 \right) \tag{A.7}$$

$$\frac{M_2}{b} - H_1 b = \frac{M_1}{b} - H_0 b \tag{A.8}$$

$$\mu_2 \left(-\frac{M_2}{b^2} - H_1 \right) = \mu_1 \left(-\frac{M1}{b^2} - H_0 \right) \tag{A.9}$$

M_1, M_2, H_1, and H_2 are calculated by Eqs. (A.6) - (A.9).

$$H_1 = \frac{2\mu_1(\mu_1 + \mu_2)b^2}{-(\mu_2 - \mu_1)^2 a^2 + (\mu_2 + \mu_1)^2 b^2} H_0 \tag{A.10}$$

$$H_2 = \frac{4\mu_1 \mu_2 b^2}{-(\mu_2 - \mu_1)^2 a^2 + (\mu_2 + \mu_1)^2 b^2} H_0 \tag{A.11}$$

$$M_1 = \frac{\left(\mu_2{}^2 - \mu_1{}^2\right)(b^2 + a^2)b^2}{-(\mu_2 - \mu_1)^2 a^2 + (\mu_2 + \mu_1)^2 b^2} H_0 \tag{A.12}$$

$$M_2 = \frac{2\mu_1(\mu_1 - \mu_2)a^2 b^2}{-(\mu_2 - \mu_1)^2 a^2 + (\mu_2 + \mu_1)^2 b^2} H_0 \tag{A.13}$$

H_2 is the magnetic field strength inside the magnetic shield. In the SSGP system, a magnetic shield of triplex structure is used. The outer structure consists of 20 layers of 0.05 mm PB Permalloy. The mid structure consists of 10 layers of PB Permalloy. The inner structure consists of 4 layers PC Permalloy. The magnetic field strength inside this magnetic shield is estimated to be reduced by 1/10000.

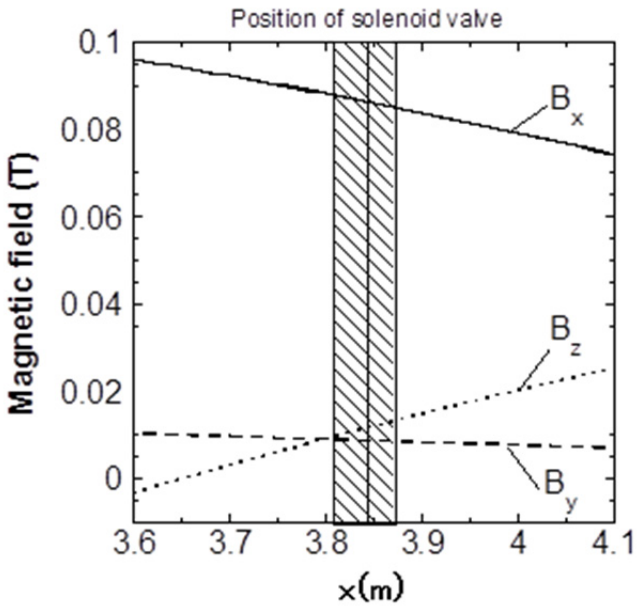

Figure A1 The magnetic field at the position of the solenoid valve in the case of SSGP device in LHD.

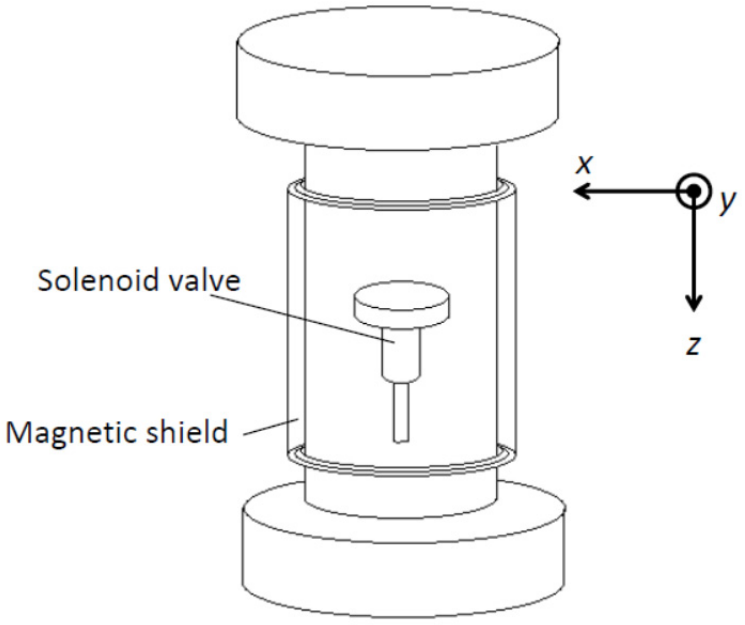

Figure A2 Schematic view of the magnetic shield of the solenoid valve.

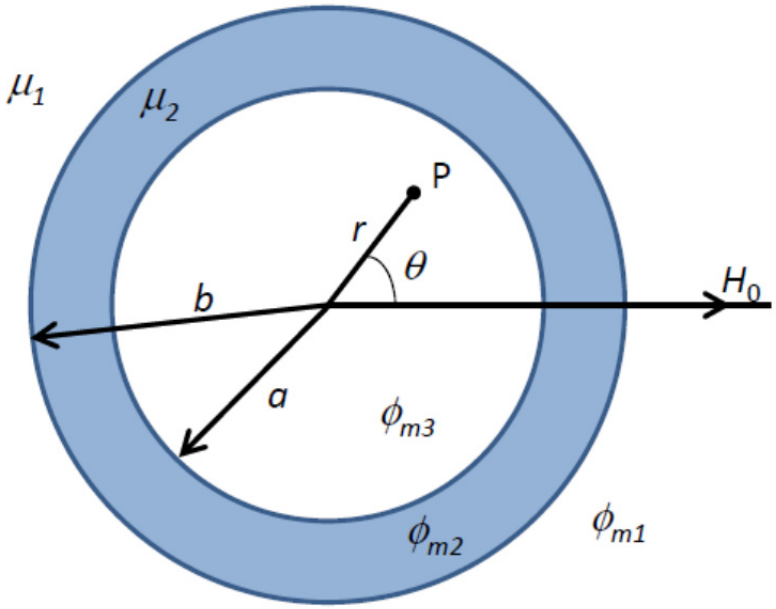

Figure A3 Schematic view of the magnetic field in a hollow cylindrical form.

List of Symbols

Chapter 1

Symbol	Definition
a	minor radius
R	major radius
V_p	plasma volume
B_t	magnetic field strength on the plasma axis

Chapter 2

Symbol	Definition
A	cross section area
A^*	cross section area at the throat
A_1	cross section area of the radial surface at the inflection point
d	throat diameter
l	length between P and Q points
M	Mach number, v/v_s
M^*	Mach number at the throat, $M^* = v^*/v_s^* = 1$
M_1	Mach number at the inflection point
M_t	Mach number of the design value
n_f	density of the flow
n_{f0}	stagnation density of the flow, $n_{f0} = p_s/R_G T_s$
n_c	number density of clusters
n_0	monomer density before becoming cluster
N_c	averaged cluster size
p	pressure of the flow
p_s	stagnation pressure of the flow
P_0	backing plenum pressure in 10^{-4} MPa
$\boldsymbol{r}^*$	vector at the throat

$\boldsymbol{r}_1$	vector at the inflection point
R_G	specific gas constant [J/(kg/K)]
S	control surface
T_0	pre-expansion temperature in Kelvin
T_s	stagnation temperature of the flow
v	velocity of the flow
v_s	speed of sound
v^*	velocity of the flow at the throat
v_1	velocity of the flow at the inflection point
v_t	Prandtl-Meyer function
V	control volume
x	distance of the stream-tube
x^*	x-coordinate at the throat
x_1	x-coordinate at the inflection point
y^*	y-coordinate at the throat, radius of the throat
y_1	y-coordinate at the inflection point
α	expansion half angle of gas flow or cluster beam
α_0	Mach angle
γ	$\gamma = c_p/c_v$, For air at standard condition, $\gamma = 1.4$
Γ^*	empirical scaling parameter
θ_1	angle at the inflection point
σ	scattering cross section

Chapter 3

Symbol	**Definition**
a_{99}	effective minor radius in which 99% of the plasma kinetic energy is confined
$\overline{n_e}$	line-averaged electron density
n_{e_edge}	edge density at reff ~ 0.64 m
N_e	total electron inventory
P_{NB}	heating power of NB injection
r_{eff}	averaged minor radius
Γ_{SSGP}	particle flux of SSGP
η_{diff}	differential fueling efficiency
η_{tot}	total fueling efficiency

ΔN_e	increase in the total electron number due to SSGP
Δt	pulse length of SSGP

Chapter 4

Symbol	**Definition**
m	poloidal mode number
n	toroidal mode number
T_e	electron temperature
P_{dep}	NBI deposition power
ρ	normalized minor radius
ι	rotational transform

List of Publications

[1] Akiyoshi MURAKAMI[1], Junichi MIYAZAWA[2], Hayato TSUCHIYA[2], Tomohiro MORISAKI[2], Nari TSUTAGAWA[3], Yoshiro NARUSHIMA[2], Ryuichi SAKAMOTO[2] and Hiroshi YAMADA[2]
[1)]SOKENDAI, [2)]NIFS, [3)]Nagoya Univ.
『*Investigation of the Clustering Condition for Various Gasses Ejected from a Fast Solenoid Valve for Supersonic Cluster Beam Injection*』
Plasma and Fusion Research, Volume 5, pp S1032-1–5, (2010)

[2] Akiyoshi MURAKAMI[1], Junichi MIYAZAWA[2], Hayato TSUCHIYA[2], Takanori MURASE[2], Naoko ASHIKAWA[2], Tomohiro MORISAKI[2], Ryuichi SAKAMOTO[2] and Hiroshi YAMADA[2]
[1)]SOKENDAI, [2)]NIFS
『*Characteristics of hydrogen supersonic cluster beam generated by a Laval nozzle*』
Journal of Plasma and Fusion Research SERIES, Volume 9, pp 79–83, (2010)

[3] Akiyoshi MURAKAMI[1], Junichi MIYAZAWA[2], Koji YASUI[2], Takanori MURASE[2], Naoki TAMURA[2], Hayato TSUCHIYA[2], Yoshiro NARUSHIMA[2], Tomohiro MORISAKI[2], Ryuichi SAKAMOTO[2], Hiroshi YAMADA[2] and LHD Experiment Group
[1)]SOKENDAI, [2)]NIFS,
『*Observation of Electron-Temperature Fluctuations Triggered by Supersonic Gas Puffing in the LHD*』
Plasma and Fusion Research, Volume 6, pp 1402135-1–5, (2011)

[4] Akiyoshi MURAKAMI[1], Junichi MIYAZAWA[2], Chihiro SUZUKI[2], Ichihiro YAMADA[2], Tomohiro MORISAKI[2], Ryuichi SAKAMOTO[2], Hiroshi YAMADA[2] and LHD Experiment Group
[1)]SOKENDAI, [2)]NIFS,
『*Fueling characteristics of supersonic gas puffing applied to large high-temperature plasmas in the Large Helical Device*』
Plasma Physics and Controlled Fusion, Volume 54, pp 055006-1–6, (2012)